



**Politecnico
di Torino**

Politecnico di Torino

Master's Degree in Civil Engineering
Academic Year. 2024/2025
Graduation Session March 2025

Seismic improvement of existing structures using bistable metamaterials

Supervisor:

Prof. Rosario Ceravolo

Candidate:

Borgianni Riccardo s305396

Co-Supervisors:

Ing. Linda Scussolini

Ing. Valeria Cavanni

For those who supported me.

Abstract

With the advancement of technology and construction techniques, newly built structures fully comply with regulatory requirements, including seismic safety standards. However, many existing buildings were designed without seismic criteria, making them particularly vulnerable to earthquake effects.

In response to the need to safeguard and protect existing structures, many technologies are being developed. However, these strategies are often invasive, not maintaining the original configuration of the structure. In this context, the need for more sophisticated technologies such as the ones involving the use of mechanical metamaterials (i.e., engineered materials with mechanical properties not existing in nature), arises.

This thesis investigates a seismic improvement solution, whose dissipative capabilities are primarily based on the properties of metamaterials, which allow for optimizing the response of structures subjected to seismic excitations. Specifically, a bistable mechanical metamaterial has been analyzed. The concept of bistability is related to the potential ability of a dynamic system to oscillate between two equilibrium states. The transition between these two states enables greater dissipation of seismic energy.

The proposed seismic improvement solution is evaluated by applying it to benchmark cases, assessing its effectiveness.

Contents

List of Figures.....	VI
List of Tables	VIII
Introduction.....	1
1 Seismic retrofitting and control strategies	3
1.1 Seismic retrofitting	4
1.1.1 Seismic retrofitting approaches and their effectiveness.....	4
1.1.2 External Sub-structure Retrofitting technology.....	5
1.1.3 The Role of External Sub-Structures in Seismic and Energy Efficiency Retrofitting.....	6
1.2 Control strategies	7
1.2.1 Tuned Mass Dumper.....	13
1.2.2 Targeted energy transfer and nonlinear energy sinks	16
2 Metamaterials and bistability	19
2.1 Metamaterials.....	19
2.1.1 Stiffness-Related Properties of Metamaterials	20
2.1.2 Negative Poisson's Ratio Metamaterials.....	26
2.2 The Idea of Bistability	27
2.2.1 Mathematical Modeling and Analysis of Bistable Structural Dynamics	31
3.0 Technology of the metapanel unit cell.....	38
3.1 Snap-through and bistability of the sinusoidal beam.....	38
3.2 Metapanel modeling	49
3.2.1 Introduction to modeling	49
3.2.2 Geometry and Materials of the Panel	49
3.2.3 Modelling with Cad	51
3.2.4 Modelling with Ansys.....	52
3.2.5 Modelling with Matlab	53
3.2.6 Results.....	54
4.0 Benchmark cases.....	56
4.1.1 Reinforced concrete structure	57
4.1.2 Masonry structure	62
4.2 Finite Element Modelling	67

4.2.1 Reinforced concrete structure	72
4.2.2 Masonry structure	73
4.2.3 Result of Reinforced concrete structures	74
4.2.4 Result of Masonry structures	76
5.0 Application of coupled system	78
5.1 Reinforced concrete structures.....	79
5.1.1 First proposed solution.....	79
5.1.2 Second proposed solution	89
5.2 Masonry structures.....	96
5.2.1 First proposed solution.....	96
5.2.2 Second proposed solution	104
6.0 Conclusion	114
References.....	117

List of Figures

Figure 1: The typical cases of the external sub-structure retrofitting method [1].	5
Figure 2: Block Diagram of active control system [3]	10
Figure 3: Block Diagram of passive control system [3]	11
Figure 4: Block Diagram of semi-active control system [3]	11
Figure 5: Schematic illustration of traditional TMD [3]	13
Figure 6: Schematic illustration of Pendulum,	14
Figure 7: Schematic illustration of NES [3]	18
Figure 8: Metamaterial Classification Based on Elastic Constants [7]	20
Figure 9: Lattice structures a) Octet-truss b) Tetrakaidecahedron [7]	22
Figure 10: Chiral and anti-chiral systems [7]	23
Figure 11: Origami geometry [7]	24
Figure 12: Cellular metamaterials [7]	24
Figure 13: Cellular metamaterials [7]	25
Figure 14: Example of deformed conditions for unit cells a) $\nu=0.8$ e b) $\nu=-0.8$ [7]	27
Figure 15: Schematic of bistable system [8]	27
Figure 16: Dependence of (a) spring force and (b) stored potential energy on the displacement position of the inertial mass [8]	28
Figure 17: An oscillator with arbitrary spring restoring force $F(x - z)$ [8]	31
Figure 18: (a) Spring restoring force profiles for linear, monostable hardening Duffing, and bistable oscillators, and (b) corresponding potential energy [8]	32
Figure 19: Example of free response displacement time series of bistable system. (b) basin of attraction map with single example case of phase portrait free response overlaid as light dashed curve, $\beta=1$, $\gamma=0.1$ [8]	36
Figure 20: Energy trapping mechanism[6]	38
Figure 21: Inclined, curved, and arched beams [6]	39
Figure 22: Force-Displacement curves for beams a) inclined, b) curved e c) arched [6]	40
Figure 23: Force-Displacement diagrams for beams: a) Inclined, b) Curved, c) Arched, varying with geometric parameters [6]	41
Figure 24: Deformation process [6]	42
Figure 25: Comparison of bistability [6]	42
Figure 26: Geometry of GNS and NNS Configurations[10]	43
Figure 27: Force-Displacement Response of a) GNS and b) NNS [10]	45
Figure 28: Force-Displacement Curve of the Cyclic Test in GNS [10]	46
Figure 29: Force-Displacement Curve of the Cyclic Test in NNS [10]	47
Figure 30: MCF and SEA for GNS and NNS [10]	48
Figure 31: Generic representation of metapanel	49
Figure 32: 2D representation of the metapanel	50
Figure 33: 3D representation of the metapanel	51
Figure 34: Aquila earthquake	52
Figure 35: Modal frequencies of the metapanel	54
Figure 36: Results of Metapanel as SDOF	54

Figure 37: First equilibrium condition.....	55
Figure 38: Second equilibrium condition	55
Figure 39: First typology of reinforced concrete building.....	58
Figure 40: Second typology of reinforced concrete building	59
Figure 41: Third typology of reinforced concrete building	60
Figure 42: Fourth typology of reinforced concrete building	61
Figure 43: First typology of masonry building.....	63
Figure 44: Second typology of masonry building	64
Figure 45: Third typology of masonry building	65
Figure 46: Fourth typology of masonry building.....	66
Figure 47: Seismogram of the Aquila earthquake	70
Figure 48: Simulated wind signal	70
Figure 49: Applied pressure due to wind.....	71
Figure 50: Earthquake displacement with one layer of metapanel (1RC).....	82
Figure 51: Earthquake displacement with one layer of metapanel (2RC).....	83
Figure 52: Earthquake displacement with one layer of metapanel (3RC).....	84
Figure 53: Earthquake displacement with one layer of metapanel (4RC).....	84
Figure 54: Wind displacement with one layer of metapanel (1RC).....	86
Figure 55: Wind displacement with one layer of metapanel (3RC).....	87
Figure 56: Earthquake displacement with two layers of metapanel (1RC).....	91
Figure 57: Earthquake displacement with two layers of metapanel (2RC).....	92
Figure 58: Earthquake displacement with two layers of metapanel (3RC).....	93
Figure 59: Earthquake displacement with two layers of metapanel (4RC).....	94
Figure 60: Earthquake displacement with one layer of metapanel (1M).....	98
Figure 61: Earthquake displacement with one layer of metapanel (2M).....	99
Figure 62: Earthquake displacement with one layer of metapanel (3M).....	99
Figure 63: Earthquake displacement with one layer of metapanel (4M).....	100
Figure 64: Wind displacement with one layer of metapanel (1M)	102
Figure 65: Wind displacement with one layer of metapanel (3M)	103
Figure 66: Earthquake displacement with two layers of metapanel (1M).....	106
Figure 67: Earthquake displacement with two layers of metapanel (2M).....	107
Figure 68: Earthquake displacement with two layers of metapanel (3M).....	108
Figure 69: Earthquake displacement with two layers of metapanel (4M).....	108

List of Tables

Table 1: Geometric dimensions of the metapanel	50
Table 2: Material parameters of infill wall	72
Table 3: Material parameters of reinforced concrete	72
Table 4: Material parameters of load bearing walls	73
Table 5: Material parameters of reinforced concrete	73
Table 6: Collection of seismic improvement for an earthquake with a single layer of metapanel for reinforced concrete structure.	85
Table 7: Collection of wind-induced dissipative capacity for a single layer of metapanel for reinforced concrete structure.	87
Table 8 Collection of seismic improvement for an earthquake with a double layer of metapanel for reinforced concrete structure	95
Table 9: Collection of seismic improvement for an earthquake with a single layer of metapanel for masonry structure.....	101
Table 10: Collection of wind-induced dissipative capacity for a single layer of metapanel for masonry structure	103
Table 11: Collection of seismic improvement for an earthquake with a double layer of metapanel for masonry structure.....	109
Table 12: Summary table for reinforced concrete structures subjected to earthquake.....	110
Table 13: Summary table for masonry structures subjected to earthquakes.....	111
Table 14: Summary table for masonry and reinforced structures subjected to wind	112

Introduction

Many buildings were originally designed, according to outdated design codes. As a result, a significant number of existing structures fail to meet current seismic upgrading standards. Therefore, it is crucial to adopt targeted preventive measures, which are preferable to securing buildings that have already been damaged by extreme events, such as earthquakes. In this context, it is vital to identify the structural issues of existing buildings and protect them. However, seismic improvement interventions on existing buildings are not always particularly efficient and often consist of invasive interventions, highlighting the need for research into more advanced technologies.

This thesis investigates a seismic improvement solution, here called metapanel, whose dissipative capabilities are primarily based on the properties of metamaterials, which allow for optimizing the response of structures subjected to seismic forces. In particular, a bistable metamaterial has been analysed. The concept of bistability is related to the potential ability of a dynamic system to oscillate between two equilibrium states. The transition between these two equilibrium states allows for greater dissipation of seismic energy.

The research is built upon a comprehensive bibliographic review, which, particularly in recent years, has thoroughly developed the topic of metamaterials and their potential applications in the design of seismic and energy improvement interventions.

The thesis is structured into five chapters:

- The first chapter will cover and introduce the concepts of seismic retrofitting and the possible types of strategic control, with particular attention to the TMD (Tuned Mass Damper) and the NES (Nonlinear Energy Sink).
- The second chapter will introduce definitions of bistable materials and nonlinear dynamic analytical developments of the basic models considered.
- In the third chapter, the metapanel, its modeling, and the energy dissipation mechanism will be introduced.

- In the fourth chapter, the buildings subjected to analysis, both masonry and reinforced concrete, will be introduced. Additionally, the type of modelling applied and the types of materials used for them will be described.
- The fifth chapter will describe the behaviour of the combined system of the metapanel and buildings. Additionally, the type of modeling and the applied loads will be discussed.
- The sixth chapter will present the results regarding displacement reduction, comparing buildings with and without panels.

1 Seismic retrofitting and control strategies

Earthquakes are one of the most destructive natural disasters, causing significant social impacts and extensive property damage. The immediate effects of an earthquake include building collapses, bridge failures, ground cracks, landslides, and more. Secondary consequences, such as fires, the spread of diseases, and social unrest, exacerbate the human toll and the overall severity of the disaster.

According to the available data, earthquakes are responsible for 54% of the total death toll from natural disasters in the 20th century. For instance, the M8.2 Kanto Earthquake in Japan in 1923 resulted in 142,000 fatalities and caused property damage exceeding 6.5 billion U.S. dollars. In 1994, the 30-second main shock of the M6.6 Northridge Earthquake led to the collapse of over 11,000 homes and caused a financial loss of more than 30 billion U.S. dollars in the United States, along with the destruction of highways and high-rise buildings within a 30-kilometer radius of the epicenter. In 2010, the M7.0 earthquake in Haiti resulted in over 270,000 deaths and affected 3.7 million people. The catastrophic effects of earthquakes have drawn global attention, making earthquake disaster prevention a significant issue in seismic research. According to the disaster statistics of over 130 rare earthquakes, more than 95% of casualties and losses were due to the destruction or collapse of buildings [1]

Typically, these structures are at a much higher risk of earthquake damage compared to new buildings. Furthermore, as seismic theory advances and related technologies improve, the recognition of earthquake risks increases, leading to more stringent regional seismic fortification requirements. This makes older buildings even more vulnerable to seismic impacts.

Given the historical and economic factors, many of these buildings cannot be demolished or reconstructed. As such, it is necessary to upgrade them to ensure they remain safe and functional in the face of seismic risks. Therefore, to solve this issue many strategies emerged, such as the seismic retrofitting technologies and control strategies.

1.1 Seismic retrofitting

1.1.1 Seismic retrofitting approaches and their effectiveness

The application of seismic retrofitting technology dates back to the 1970s, when Robinson first introduced the concept of seismic retrofitting for highway bridges following the 1971 San Fernando earthquake. Since then, seismic retrofitting technology has garnered significant attention and exploration from researchers worldwide. Various retrofitting methods with multiple objectives and diverse outcomes have been proposed and implemented in practical engineering.

Currently, seismic retrofitting technology is still developing rapidly, with numerous advancements covering aspects such as construction details, experimental techniques, numerical strategies, theoretical models and case studies.[1]

Seismic retrofitting technologies can be generally divided into three types: (i) strength-improving type; (ii) ductility-improving type; (iii) seismic dissipation/isolation type.

The first category encompasses the most traditional retrofitting techniques, including material replacement, cross-section enlargement, reinforcement addition, and bolt anchoring, among others.

The second category is further divided into two subtypes: component surface strengthening and component interior strengthening. This includes methods like increasing stirrups, wrapping with fiber-reinforced polymers (FRP), surface prestressing, and steel encasement.

The third category involves the use of additional devices, such as friction dampers, viscous dampers, and isolating bearings.

The first and second categories typically focus on the main load-bearing elements of structures, converting them into energy-dissipating components. However, these elements are more likely to suffer damage during an earthquake, potentially leading to the demolition or loss of functionality of the structure. In contrast, the third category utilizes non-load-bearing or additional components (like dampers) for

energy dissipation or isolation, thus protecting the main structure by allowing these supplementary components to absorb the damage.

1.1.2 External Sub-structure Retrofitting technology

The external sub-structure retrofitting method[1] has become widely adopted in seismic-prone regions over the past few decades. This method integrates an external sub-structure with the existing building, enabling them to function as a cohesive unit during an earthquake. By using an external sub-structure, the transfer of forces, lateral displacement, and accumulated seismic damage in the original structure can be significantly reduced, resulting in a substantial improvement in the overall mechanical performance of the building. The introduction of the external sub-structure can alter the structural configuration of the system, enhancing the integrity of the existing structure. At the same time, it allows for the strengthening of weak layers in the existing structure, making the structural capacity and stiffness more uniform. Furthermore, because the retrofitting process occurs externally, it does not disrupt the normal operation of the building's inner structure, which is particularly valuable for lifeline infrastructures such as schools, hospitals, and nuclear power plants, where service interruptions must be avoided. Additionally, the external retrofitting sub-structures typically do not bear vertical loads (i.e., gravity) but are designed to resist only horizontal seismic forces.



Figure 1: The typical cases of the external sub-structure retrofitting method [1].

1.1.3 The Role of External Sub-Structures in Seismic and Energy Efficiency Retrofitting

The external construction of the externally attached sub-structure allows for changes to the overall structural system through its design, enabling the incorporation of technical methods such as energy dissipation and the use of new materials during the retrofitting process.[1] For instance, energy-dissipating dampers can be integrated into the external sub-structure to absorb the damage to the original structure, while the sub-structure itself provides space to house these dampers, circumventing the issue of limited space in the facades or infills of existing buildings.

Moreover, new materials that were not considered when the original structure was built can be introduced into the external sub-structure, enhancing the seismic performance of the building to meet various demands (e.g., ultra-high performance concrete, self-compacting concrete, high-strength steel, and memory alloys).

The external sub-structure can boost the overall structural capacity and improve performance by modifying its own structural forms and construction details.

Energy-efficient retrofitting has become an essential concern, and the external sub-structure retrofitting method offers an ideal solution for the comprehensive retrofitting (including form, energy, and functionality) of the entire building, significantly improving energy efficiency and reducing long-term maintenance costs of existing structures.

1.2 Control strategies

Seismic safety is undoubtedly a global priority, which is why one of the primary concerns for researchers in this field is to develop innovative concepts for the anti-seismic design of structures.

The traditional approach to reduce vibrations caused by earthquake and wind loads involves designing building structures with sufficient resistance and the ability to deform in a ductile manner. This strategy, which focuses on ensuring the combination of resistance and ductility in structural key elements, treats strong seismic forces as a load that the structure must endure and remain intact, while accepting some level of both structural and non-structural degradation. In this approach, the structure deforms well beyond its elastic limit, with inelastic deformations taking the form of localized plastic hinges, leading to energy dissipation and increased flexibility.

On the other hand, newer structural control strategies, including passive, active, and semi-active systems, aim to avoid the inelastic deformations of the structure altogether.

Design concepts based on energy criteria have become increasingly relevant in the development of new energy dissipation technologies. This approach focuses more on the structure's ability to dissipate energy than on its resistance to lateral forces. The energy concept in design is not a recent development; in fact, as early as 1956, Housner proposed a design method based on energy concepts for traditional structures[2]

Generally, the work done by external forces acting on a system is equal to the sum of the mechanical energy temporarily stored in the structure (kinetic and recoverable strain energies) and the energy transformed into other forms, either as viscous damping energy or irrecoverable hysteretic energy. The energy balance equation, accounting for these forms, takes the following time-dependent conservation of energy form:

$$E_i = E_k + E_s + E_d + E_h + E_m \quad (1)$$

where, at time t ,

E_i - input energy in structure by the ground motion;

E_k - kinetic energy stored in the mass;

E_s - recoverable strain energy stored by the structure;

E_d - viscous damping energy dissipated by the principal elements of the structure;

E_h - hysteretic energy dissipated by the principal elements of the structure;

E_m - viscous or hysteretic energy dissipated by the supplemental passive, semi-active or active system.

The input energy can be written as

$$E_i = \int_0^t -m\ddot{x}_g(t)dx(t) = \int_0^t -m\ddot{x}_g(t) \frac{dx(t)}{dt} dt = -m \int_0^t \ddot{x}_g(t)\dot{x}(t)dt = \quad (2)$$

The kinetic energy and the recoverable strain energy are given by

$$E_k = \int_0^t m\dot{x}(t)\dot{x}(t)dt = \frac{m}{2} \dot{x}(t)^2 \quad (3)$$

$$E_s = \int_0^t kx(t)\dot{x}(t)dt = \frac{k}{2} x(t)^2 \quad (4)$$

The energy dissipated through viscous damping of the structure has the following form:

$$E_d = \int_0^t c\dot{x}(t)\dot{x}(t)dt = c \int_0^t \dot{x}(t)^2 dt = \quad (5)$$

In case of inelastic deformation, the absorbed energy becomes

$$E_p = E_p + E_h = \int_0^t f_h(t)dx(t) = \int_0^t f_h(t)\dot{x}(t)dt = \quad (6)$$

Where f_h represents the restoring force, which depends on the deformation history, specifically whether the deformation is increasing (positive velocity) or decreasing (negative velocity).

The control and safety of buildings, for a given input and energy, can be achieved through various control strategies[3]. These strategies, which we will describe in more detail, help manage the structural response and enhance the building's resilience to dynamic forces.

1. The **active control system** utilizes measured excitation and structural response to generate a calculated control signal, which is then transmitted to electrohydraulic or electromechanical actuators. These actuators apply the necessary control forces to the structure

A common example of such systems is the active mass damper *Fig. 2*, which consists of a small auxiliary mass connected to the upper floors of the main structure through an actuator. The controller continuously monitors accelerometer and displacement data from the input excitation and key points within the primary structure. It processes these measurements using a predefined control algorithm and sends the necessary control signal to the actuator. The electrohydraulic or electromechanical actuator applies inertial forces to both the auxiliary mass and the main structure to reduce the structural response. Clearly, producing the control forces requires substantial and continuous power sources, typically in the range of kilowatts for small structures and megawatts for larger ones.

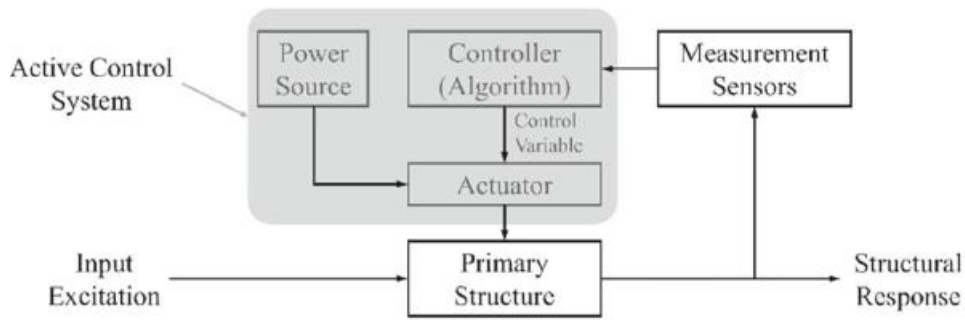


Figure 2: Block Diagram of active control system [3]

2. The **passive control systems** are made up of localized components that engage with the structural vibrations to absorb and dissipate a large portion of the input energy, effectively reducing the vibration levels within the structure.

As illustrated in *Fig. 3*, the control forces are generated through the coupling mechanism between the main structure and the passive control device, meaning that no external power source is required for their operation. Input excitations can also assist in activating the passive control devices, depending on the type of loading and the structure of the control system. Furthermore, passive control systems do not rely on feedback, eliminating the need for sensors, actuators, and control computers.

However, while they enhance the energy dissipation capabilities of the main structure in specific scenarios, their performance is greatly influenced by changes in the structure's properties, usage patterns, and the unpredictable nature of loading conditions.

There are various types of passive control systems, including tuned mass dampers, liquid and viscous fluid dampers, viscoelastic dampers, friction dampers, metallic yield dampers, and base isolation systems.

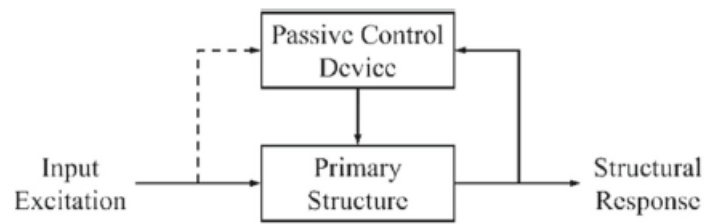


Figure 3: Block Diagram of passive control system [3]

3. A **semi-active control** device can be described as a modified version of a passive control system that doesn't introduce energy into the primary structure or the control device. Instead, it adjusts the properties of the device to optimally reduce the system's response *Fig. 4*.

Similar to a passive control system, the control forces are generated by the motion of the primary structure. However, the magnitude of these forces is regulated through feedback from sensors that measure the structure's response, much like in an active control system. As a result, semi-active control systems offer the adaptability of an active system without the need for large power sources, as only a small amount of external power is required.

Examples of semi-active control systems include controllable stiffness vibration absorbers, variable tuned liquid or fluid dampers, variable orifice dampers, and controllable impact dampers.

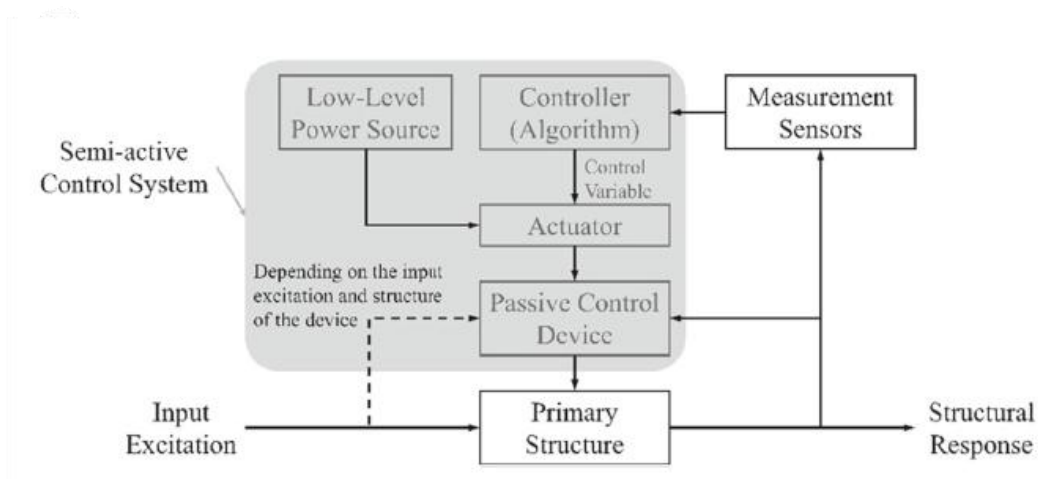


Figure 4: Block Diagram of semi-active control system [3]

4. **Hybrid control systems** combine passive, semi-active, and active control systems to integrate the advantages of each conventional system into a single solution. This integration allows for higher levels of reliability, efficiency, and adaptability. However, the trade-off is increased design complexity and cost. Additionally, the full-scale implementation of hybrid control systems may face challenges such as limited space and potential stability issues if the system is not properly designed.

1.2.1 Tuned Mass Dumper

Vibration reduction can be accomplished by using passive linear absorbers, such as Tuned Mass Dampers (TMD), which quickly dissipate a significant portion of the energy received from seismic or impulsive excitations affecting the structure.

Tuned Mass Damper (TMD), first introduced by Frahm, is the most popular passive linear vibration absorber utilized in structures, particularly in tall buildings and towers and sometimes in aerospace[3].

This device is called "tuned" because its natural frequency is adjusted to match a specific structural mode frequency, where the majority of the vibration energy is introduced into the structure. As a result, most of the vibration energy from that mode is quickly absorbed by the tuned linear absorber, where it is dissipated, thereby reducing the vibration of the entire structure. In its most basic and commonly used form, the traditional Tuned Mass Damper (TMD) consists of a supplemental mass that is linearly coupled to the structure through an elastic element and a linear viscous damping device.

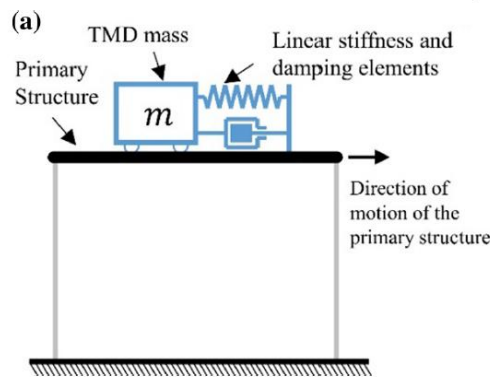


Figure 5: Schematic illustration of traditional TMD [3]

Linear vibration absorbers have also been utilized in many tall buildings for the protection against earthquakes, wind and blast excitations.

For example, Burj-Al Arab and Emirates Towers in Dubai buildings equipped with eleven 5000 kg and six 1200 kg TMDs respectively. The most famous passive control system is the pendulum TMD installed in Taipei 101 tower. Given the active geographical location, the 101-floor building in Taiwan is prone to strong winds, typhoons and earthquakes. Therefore, huge 728-ton pendulum TMD was suspended from the 92nd floor to the 87th floor [3].

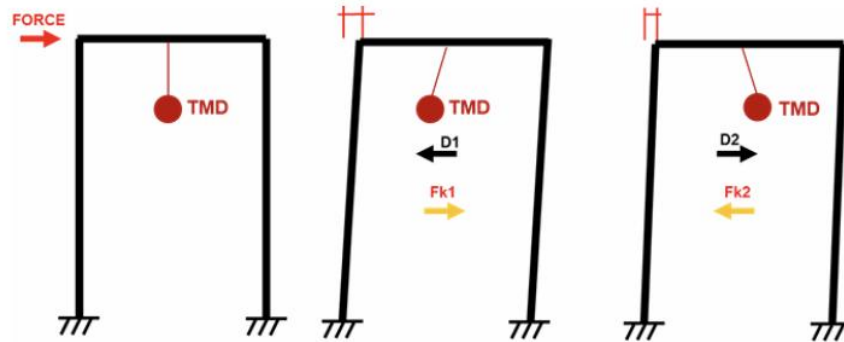


Figure 6: Schematic illustration of Pendulum,

Tuning the natural frequency of a Tuned Mass Damper (TMD) to a specific structural mode is critical for efficient vibration energy absorption and dissipation. When the structural mode is closely matched with the TMD's frequency, strong resonance occurs at a 1:1 ratio, ensuring effective energy capture and vibration suppression. However, this performance significantly deteriorates when frequency fluctuations occur between the TMD and the associated structure.

Several issues arise from this lack of robustness in TMDs[3]:

- **Frequency Variability:** The natural frequency of the primary structure may change due to various factors such as unexpected actions, aging, and extreme loading conditions. Aging and environmental factors (e.g., settlement, fatigue, humidity, and temperature) can affect the stiffness and mass of the structure, causing small variations in its natural frequency, which reduces the effectiveness of the TMD.

- **Extreme Loading Conditions:** These are particularly problematic for passive control systems like TMDs for two key reasons:
 - Multiple modes are often excited during extreme seismic or shock loading, but TMDs are designed to address only one specific mode. As a result, they cannot mitigate the response of other modes.
 - Large-scale systems have multiple natural frequencies, making the TMD less effective in such complex systems. While the largest amplitudes and most severe oscillations typically occur at the lowest natural frequencies, it becomes critically important to manage oscillations at higher frequencies, especially for large-scale structures.

Even though structures are designed to maintain their elastic properties under various loading conditions, in extreme events such as blasts or earthquakes, the structures may yield to dissipate more energy. However, this inelastic behavior alters the design frequencies and significantly reduces TMD efficiency. Additionally, estimating the actual natural frequency of real-world structures often involves idealizations, leading to uncertainties and possible detuning of the TMD, rendering it ineffective.

In conclusion, to protect primary structures from damage, it is necessary to absorb the induced vibrational energy through energy dissipators. However, because induced energy can vary in form, magnitude, and frequency, passive linear vibration absorbers that rely heavily on the system's natural frequency are not always the optimal solution. This limitation has led to growing interest in nonlinear passive dissipation systems, which offer rapid and efficient vibration suppression across a broad range of frequencies and energy levels. Consequently, the TET (Tuned Energy Transfer) mechanism in nonlinear vibration absorbers has been extensively developed and studied over the past two decades.

1.2.2 Targeted energy transfer and nonlinear energy sinks

The primary goal of vibration absorbers is to protect structural dynamic systems from damaging vibration amplitudes by passively transferring and dissipating unwanted energy induced into these systems. The process by which energy is transferred from a primary structure to an attached recipient system in an irreversible manner is called Targeted Energy Transfer (TET)[3]. This energy transfer occurs due to the nonlinear interaction between the nonlinear energy sink (NES) and the structure, which results in efficient passive energy transfer. Even for structural modes with broadband frequencies, nonlinear energy interactions can still take place in nonlinear systems due to single or multiple internal resonances. Unlike linear vibration absorbers, which function within a narrow frequency range, the global behavior of the linear system is significantly altered by the nonlinear attachment. This is because the nonlinear attachment has a frequency-energy dependence, allowing it to function in a broadband fashion and effectively transfer and dissipate energy through multiple resonance captures with the linear system. Such a nonlinear attachment is referred to as a Nonlinear Energy Sink (NES).

An effective TET process using NESs should have the following characteristics:

- The energy should be transferred to the NES in a nearly one-way, irreversible manner, meaning minimal energy should return to the primary structure.
- Large amounts of energy should be rapidly transferred and dissipated from the primary system.
- The TET should work efficiently across a wide range of excitation conditions, including impulsive or seismic loads.
- The added mass of the NES should be relatively lightweight compared to the primary structure's mass.
- The TET process should be robust, maintaining efficiency despite changes in the dynamic system parameters.

Over the past few decades, TET has gained significant interest, especially in shock mitigation and energy harvesting applications. The concept of using NESs for TET was first introduced by Vakakis and Gendelman in 2001[4], where they demonstrated analytically that NESs could perform one-way, irreversible passive TET across broadband frequency ranges. Since then, extensive research has been conducted to explore various NES designs for different engineering applications.

NESs are a relatively new class of passive structural control devices. They are lightweight, nonlinearly coupled attachments with mass much smaller than the associated structure. NESs are primarily used to mitigate vibrations induced by external shocks, impulsive forces, or seismic loading. Recent research has focused on developing various NESs with robust performance to achieve TET across broad frequency and energy ranges. Unlike linear vibration absorbers, such as TMDs, which are effective only for specific modes and frequencies, NESs can transfer energy over a broad frequency range.

One of the key findings of Vakakis and Gendelman [4] was that NESs are frequency-independent, meaning they can be excited at any frequency as long as the amplitude is sufficient. This property has driven much of the subsequent research and development in NES technology. NESs can be classified based on the type of nonlinear coupling mechanism they employ with the target linear structure.

NESs can be categorized based on the type of nonlinear coupling mechanism used with the targeted linear structure. One type of NES utilizes purely cubic stiffness in the coupling force between the NES and the linear structure. This cubic stiffness is a nonlinear characteristic that can be realized through geometric nonlinearity. The force generated by this cubic stiffness is achieved by coupling the NES to the structure using two opposite linear springs that deform in the transverse direction relative to the NES motion.

Some of these stiffness-based NESs operate with either single or multiple degrees of freedom. Various kinds of stiffness-based NESs include types such as Type I, Type II, and Type III. Type I NESs, for example, employ a nonlinear cubic restoring force along with a linear viscous damping element, as depicted in the schematic

illustrations *Fig. 7*. This configuration has been applied in models of shear buildings, aerospace structures, and spacecraft.

The absence of a linear stiffness component, combined with the purely nonlinear coupling element, enables the NES to engage in multiple resonance captures along harmonic and subharmonic resonance backbones in the frequency-energy plot of periodic oscillations.

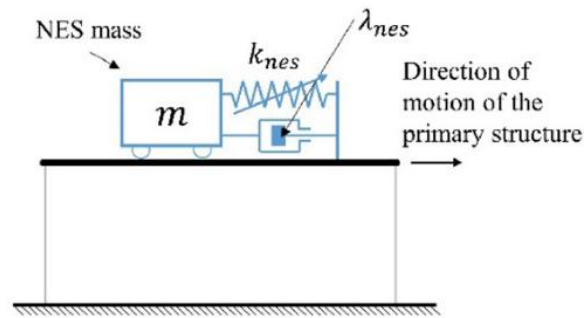


Figure 7: Schematic illustration of NES [3]

2 Metamaterials and bistability

The word „Meta“ is taken from Greek whose meaning is “beyond”. “Metamaterials” has the exotic properties beyond the natural occurring materials [5].

Metamaterials are artificial, and their properties are always determined by their own periodically arranged cell elements rather than the chemical make-up [6].

For this reason, the seismic improvement designed in the thesis in question represents an innovative solution, combining two advanced technologies: the Tuned Mass Damper (TMD) and metamaterials. This combination allows to obtain a seismic damping device that not only reduces vibrations through energy transfer, as occurs in traditional TMDs, but also exploits the properties of metamaterials to improve the effectiveness of the system.

2.1 Metamaterials

According to Xianglong Yu [7], mechanical metamaterials are artificial structures designed to exhibit counterintuitive mechanical properties, which depend on the geometry of the unit cell rather than the intrinsic characteristics of the individual components.

These metamaterials are commonly described by four fundamental constants: **Young's modulus (E)**, **shear modulus (G)**, **compressibility modulus (K)**, and **Poisson's ratio (ν)**. Unlike conventional materials, metamaterials do not occur naturally and are the result of human design and creativity. Their uniqueness lies in the ability to engineer units resembling atoms, thus creating materials with extraordinary properties. These distinctive characteristics are derived from the geometry of their microstructure rather than the composition of the materials themselves.

Metamaterials, therefore, exhibit a range of significantly enhanced mechanical

properties, such as null or negative Poisson's ratios, negative stiffness, or negative compressibility. *Fig. 8* provides a classification of metamaterials based on their elastic constants.

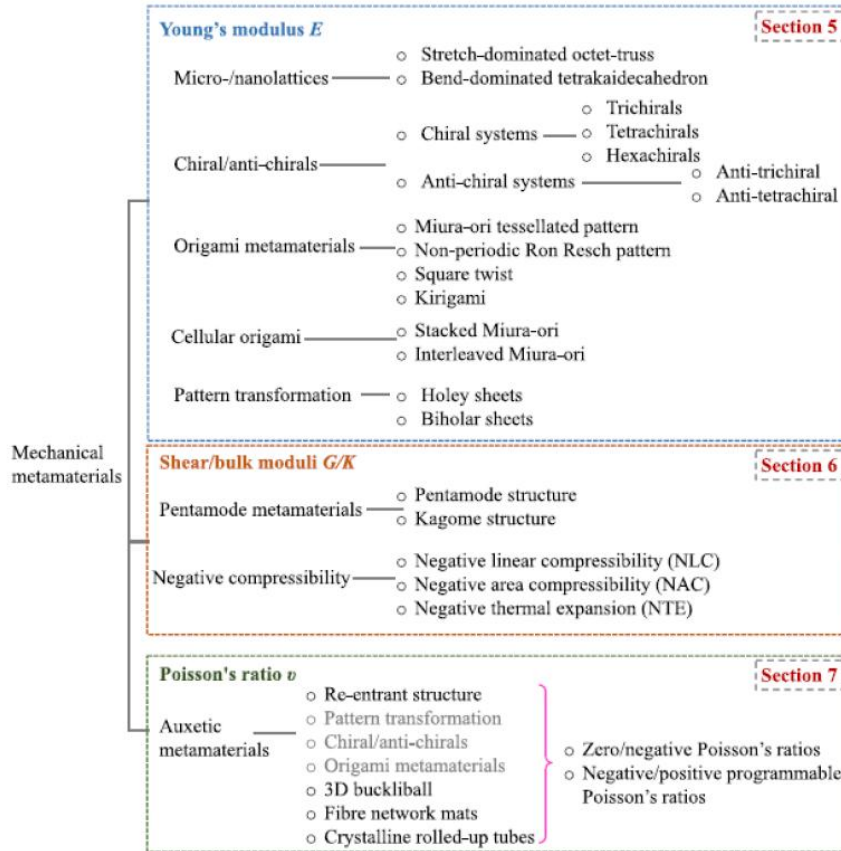


Figure 8: Metamaterial Classification Based on Elastic Constants [7]

2.1.1 Stiffness-Related Properties of Metamaterials

In almost all known elastic systems, stiffness describes the relationship between the applied force and the resulting displacement, similar to the spring constant of a spring. When an elastic object is compressed, it resists deformation by exerting a restoring force that attempts to return it to its initial position. Positive stiffness occurs when the deformation and applied force act in the same direction, creating a force that restores the object to its original configuration. However, in mechanical metamaterials, it is possible to achieve negative stiffness, which facilitates the applied deformation instead of opposing it.

The study by Xianglong Yu [7] highlights how different mechanical metamaterials can be divided into four main categories related to adjustable stiffness: **micro or nano lattices**, **chiral/anti-chiral metamaterials**, **origami-inspired metamaterials**, and **cellular metamaterials**.

A lattice material is made up of a cellular or truss structure, consisting of many uniform elements, such as thin beams or rods. These materials are created by tessellating a unit cell in space, which serves as the building block. The design of lattice materials requires attention to both the geometry of the unit cell and the arrangement of the entire lattice, as these factors significantly influence the material's final properties. In traditional applications, such as foams and aerogels, the lattice architecture is often determined using stochastic methods and typically features porosity greater than 50%. However, artificial micro and nano lattices, inspired by natural cellular solids like honeycomb structures, have more ordered architectures that enable precise control over the cellular structure. In the design of micro/nano lattice metamaterials, two key aspects need particular attention: the unit cell and its tessellation. Most of these ultra-light metamaterials, with densities lower than 10 mg/cm^3 , are made using a variety of solid materials and a hierarchical structure.

To characterize the mechanical properties of lightweight and strong metamaterials, it is essential to examine the relationship between strength and density in micro and nano lattices. Reducing material density often leads to a decline in mechanical properties, as structural elements tend to bend microscopically under macroscopic loads.

Two fundamental factors in designing micro and nano lattice metamaterials are the geometry of the unit cell and the arrangement of the lattice structure. The unit cell configuration influences both stiffness and yield strength, while the spatial arrangement determines the distribution of voids within the structure, which is crucial for maintaining lightness and strength. Additionally, in conventional cellular materials like foams and aerogels, the properties of the elastic modulus versus density are often independent of the dimensional scale or specific symmetry of the structure. However, recent studies have shown that, in structures with cubic

symmetry (simple cubic, body-centred cubic, and face-centred cubic), the elastic modulus dependent on density can exhibit structural anisotropy, affecting the material's response in different directions.

Mechanical metamaterials, whose stiffness depends more on their geometric configuration than on their chemical composition, allow for a linear scaling relationship between stiffness and density over a wide range of densities while using a variety of constituent materials. This approach, which reduces the degradation of the elastic modulus with decreasing relative density, has led to the development of ultra-light but strong metamaterials, ideal for advanced applications.

Two examples of such lattice structures *Fig. 9*, commonly described in technical literature, are the tension-dominated octet-truss and the bending-dominated tetrakaidecahedron.

Octet-trusses, made from metals or ceramics, have a triangulated geometry that allows the structure to deform predominantly through the axial elongation of the truss elements. This type of structure maintains a linear relationship between the elastic modulus and relative density, enabling the creation of ultra-light and rigid metamaterials. The unit cell of the octet-truss is based on a regular octahedron surrounded by eight tetrahedra, with a crystal structure similar to that of a face-centered cubic unit cell.

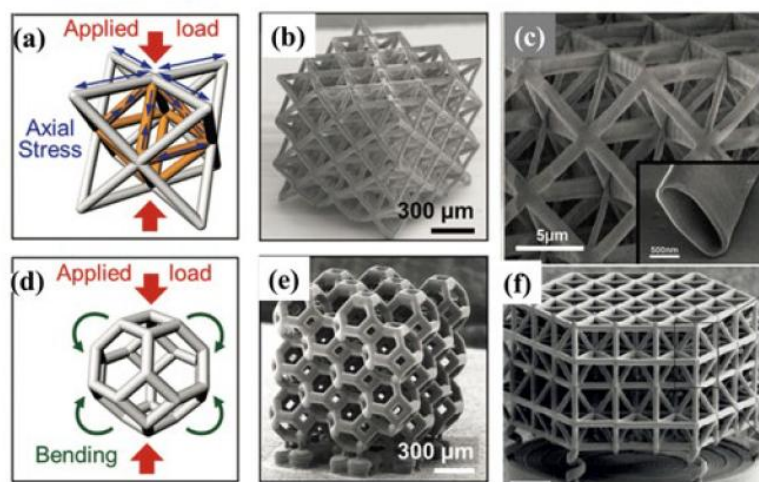


Figure 9: Lattice structures a) Octet-truss b) Tetrakaidecahedron [7]

Chiral structures are configurations that exist as mirror images that cannot be superimposed, and they can be designed in either right-handed or left-handed forms.

In this lattice, each unit cell contains a central cylinder, called a node, to which six units are tangentially connected, forming a sixfold rotational symmetry, known as hexachiral.

Chiral units can be further categorized into chiral and anti-chiral systems *Fig. 10*: in chiral systems, the nodes are positioned on opposite sides of the links, while in anti-chiral systems, the nodes are located on the same side, with equal proportions of right-handed and left-handed units.

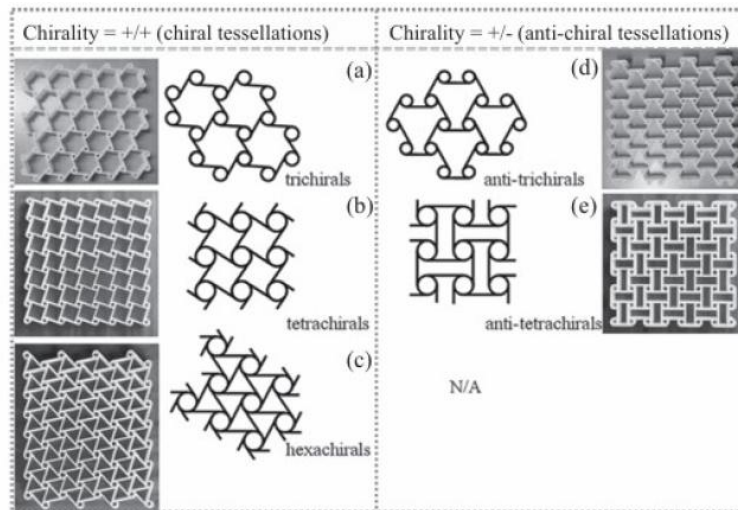


Figure 10: Chiral and anti-chiral systems [7]

The third type covered by Xianglong Yu [7] is origami, traditionally a Japanese art form involving the folding of paper to create decorative shapes without cutting. Today, it has become a technique used in engineering to design ultra-light, customizable mechanical metamaterials.

In computational origami geometry, key elements like folds and vertices are defined *Fig. 11*: folds are the lines along which the surface is bent, vertices are the points where folds meet, and the areas enclosed by folds are referred to as faces. Folds can be categorized into mountain folds and valley folds, based on the direction of the bend. In structural models, folds function as joints or hinges, allowing the structure to move and take on specific forms

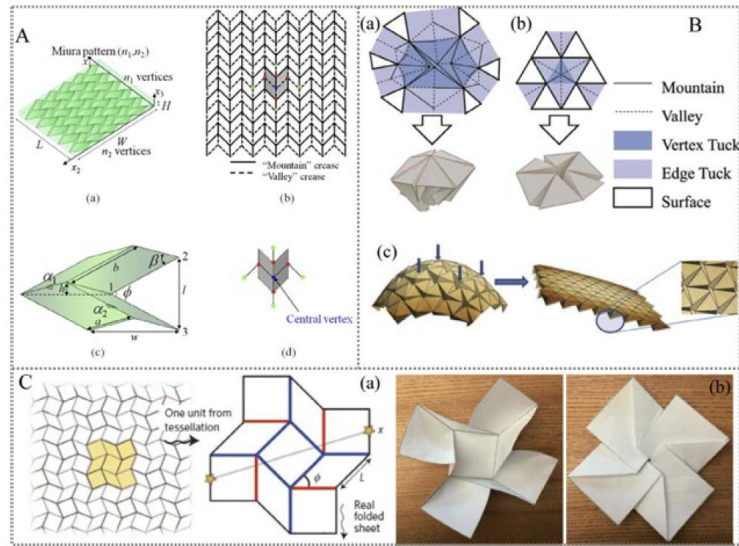


Figure 11: Origami geometry [7]

The final type explored is related to cellular systems. Today, the design concepts of origami are being used in the development of three-dimensional cellular materials, resulting in the creation of new foldable cellular metamaterials *Fig. 12*. These metamaterials combine the structural framework of micro and nano lattices with novel patterns derived from origami, maintaining the instability mechanisms and pattern transformations that are fundamental to traditional origami.

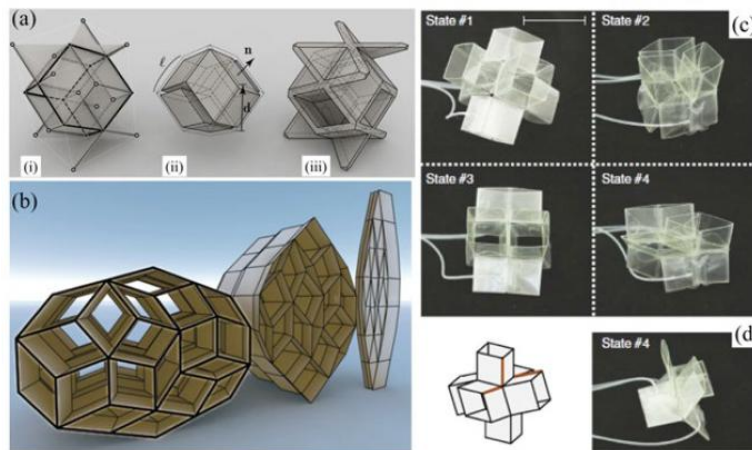


Figure 12: Cellular metamaterials [7]

The text also explores the transformation of patterns into specific configurations, particularly in structures with perforated patterns. This transformation is marked by a significant change in the material's stress and strain properties when compressed beyond a critical threshold. The process is driven by a cooperative bending mechanism, which leads to the development of meta-mechanical properties *Fig. 13*.

One key feature of pattern transformation is the ability to control stiffness in both axial and normal directions under compression.

The shape and arrangement of the pores play a vital role in influencing the transformation process. Whether the pores are circular, elliptical, or irregular, their form significantly impacts the onset of instability and post-buckling behaviour. By adjusting the pore shapes, it becomes possible to fine-tune the material's initial elastic response, instability, and post-buckling behaviour, thereby achieving specific mechanical properties, such as adjustable stiffness.

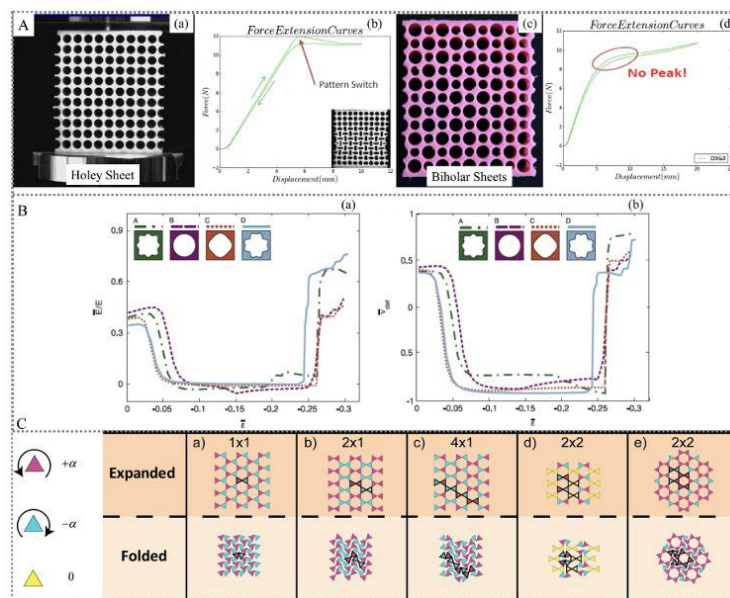


Figure 13: Cellular metamaterials [7]

Additionally, two specific pore arrangement patterns are discussed: **holey sheets** (plates with uniformly sized holes) and **biholar sheets** (plates with two hole sizes). Holey sheets act as rigid cellular structures connected by beams, allowing for high energy absorption when deformed beyond the linear elastic regime. In contrast, biholar sheets can exhibit programmable behaviour, such as hysteretic response,

resulting from the elastic instability that leads to yielding effects. In summary, elastic instabilities in periodic porous structures open up new possibilities for applications in metamaterials, as they allow for changes in structural properties in response to external stimuli.

2.1.2 Negative Poisson's Ratio Metamaterials

Considering an elementary parallelepiped subjected solely to the normal stress component σ_x , the deformations of the considered element are given by:

$$\varepsilon_x = \frac{\sigma_x}{E} \quad (7)$$

$$\varepsilon_y = -\frac{\nu}{E}\sigma_x = -\nu\varepsilon_x \quad (8)$$

$$\varepsilon_z = -\frac{\nu}{E}\sigma_x = -\nu\varepsilon_x \quad (9)$$

The coefficient ν indicates the ratio of the strain induced in the directions perpendicular to the applied stress to the strain in the direction of the applied stress:

$$\nu = \frac{\varepsilon_y}{\varepsilon_x} = \frac{\varepsilon_z}{\varepsilon_x} \quad (10)$$

The ratio ν is known as the normal elastic modulus or Poisson's ratio. Xianglong Yu [7] points out that, in most solids, when an object is stretched axially, it contracts in the lateral directions. However, some materials exhibit a negative Poisson's ratio, with values approaching -1, meaning they expand laterally when stretched and contract when compressed *Fig. 14*. These materials are referred to as auxetic metamaterials.

Additionally, auxetic metamaterials can be classified into two groups: complete auxetics and partial auxetics. In the former, the Poisson's ratio is always negative or zero, while in the latter, the ratio can be both positive and negative depending on the orientation of the meta-atoms undergoing deformation.

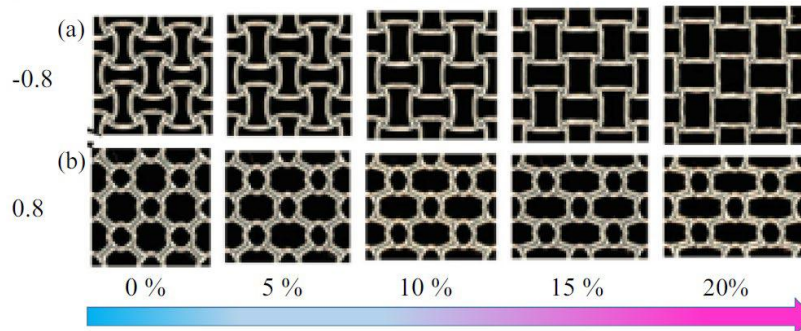


Figure 14: Example of deformed conditions for unit cells a) $v=0.8$ e b) $v=-0.8$ [7]

2.2 The Idea of Bistability

To present the key static features of a bistable structure, a diagram of a one-dimensional mechanical bistable system is illustrated in *Fig. 15* [8].

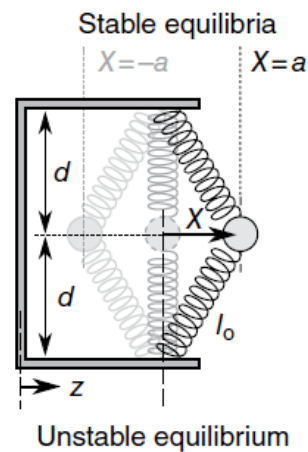


Figure 15: Schematic of bistable system [8]

In the bistable system depicted in *Fig. 15*, two identical springs with undeformed lengths l_0 connect a lumped mass to a surrounding frame with a span of $2d$. It is assumed that all displacements occur in a horizontal direction, so the frame motions z and mass displacements X move along the same axis.

When the undeformed spring length is less than or equal to half the span of the frame ($l_0 \leq d$), the system is monostable, and the mass will settle at the zero-displacement position ($X = 0$). However, when the undeformed spring length exceeds half the span of the frame ($l_0 \geq d$), the springs exert a force on the mass,

making it difficult to maintain the central position. In this case, the zero-displacement configuration becomes unstable, and two stable positions of the mass exist, which are symmetrically adjacent to the central unstable state. Due to the geometric condition $l_0 > d$, the mass-spring-frame system is classified as bistable, with the stable equilibrium positions being $X = \pm a$.

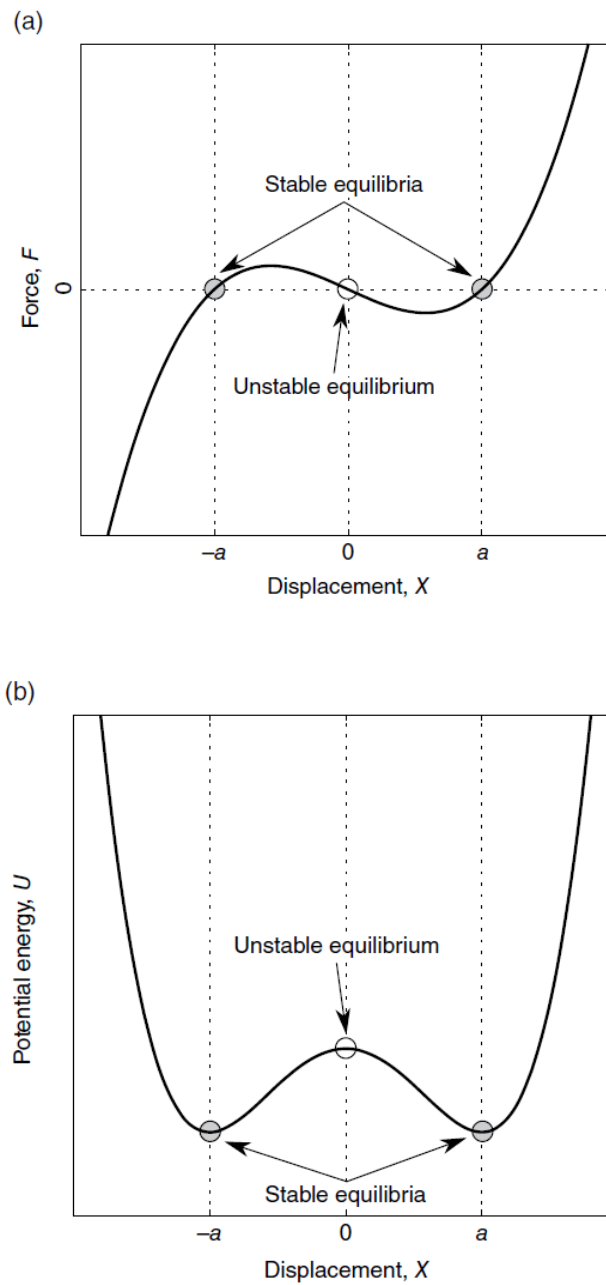


Figure 16: Dependence of (a) spring force and (b) stored potential energy on the displacement position of the inertial mass [8]

Fig. 16a and Fig. 16b show the force $F(X)$ and potential energy $U(X)$ of the bistable system, respectively, as functions of the mass displacement. The potential energy is determined by the integral $U = \int F dX$.

As shown in Fig. 16a, the total restoring force in the X-axis is zero when the inertial mass is positioned at any of the equilibrium points. In contrast, Fig. 16b demonstrates that the potential energy is maximized at the unstable central configuration of the inertial mass ($X = 0$), while the adjacent stable equilibria at $X = \pm a$ correspond to local minima in the potential energy of the system.

Principle of total potential energy

Deformation and stress analysis of structural systems can be accomplished using the principle of Minimum Potential Energy (MPE), which states that for conservative structural systems, of all the kinematically admissible deformations, those corresponding to the equilibrium state extremize (i.e., minimize or maximize) the total potential energy. If the extremum is a minimum, the equilibrium state is stable. By Hooke's law, the stiffness of a spring element is determined by the spatial derivative of the restoring force, dF/dX . Considering the total spring force profile at the unstable equilibrium in Fig. 16a, it is apparent that the bistable spring is characterized as having a negative stiffness for this mass position. In contrast to a spring which resists the motion of the mass in a given direction, a spring exhibiting negative stiffness over a range of displacements will assist the motion of the mass. As a result, the small perturbation to the inertial mass when precisely positioned at the unstable equilibrium will lead the bistable spring to propel the mass away from the central location to one of the stable system configurations. The bistable system considered for this thesis show this fundamental, static characteristic illustrated using the mechanical example in Fig. 15. In fact, the existence of two statically-stable equilibria configurations and one unstable configuration make it straightforward to identify bistable structures or systems.

However, the type of geometrical constraints exemplified in the mechanical device shown in Fig. 15 are just one possible approach to effect bistability.

For the technical areas of vibration control, energy harvesting, or sensing, numerous and diverse methods are employed to realize bistability [9].

2.2.1 Mathematical Modeling and Analysis of Bistable Structural Dynamics

The linear oscillator is one of the most fundamental vibratory systems, as shown in *Fig. 17*. However, if other polynomial terms are present, the system becomes inherently nonlinear. The general form of the restoring force in such an oscillatory system is represented by a smooth polynomial such as [8]:

$$F(y) = k_1y + k_2y^2 + k_3y^3 + \dots \quad (11)$$

The deformation of the spring is measured from its undeformed length, denoted as y . It is crucial to emphasize that the values of k_i can be positive, negative, or zero. These values are typically determined through experimentation or derived by using a series expansion of the exact force expression, which is written in terms of physically relevant system parameters, such as the beam's length, thickness, and other related characteristics.

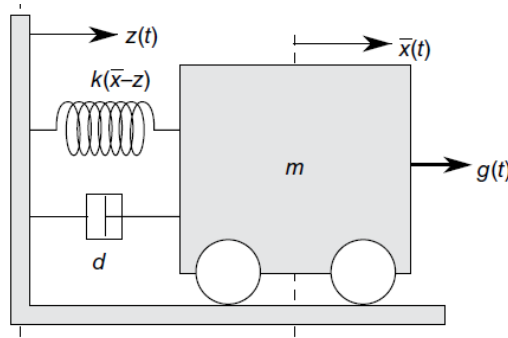


Figure 17: An oscillator with arbitrary spring restoring force $F(\bar{x} - z)$ [8]

For example, when the base excitation is $\mathbf{z} = \mathbf{0}$, the restoring force for the one-dimensional absolute motion \mathbf{X} of the mass-spring system shown in *Fig. 15* is given by:

$$F(X) = 2kX \left[1 - \frac{l_0}{\sqrt{X^2 + d^2}} \right] \quad (12)$$

where k is the spring stiffness constant.

If the base excitation is non-zero ($\mathbf{z} \neq \mathbf{0}$), the previously mentioned relation for the restoring force remains valid, with the substitution $\mathbf{x} \rightarrow \mathbf{y} - \mathbf{X} = \mathbf{z}$, where \mathbf{y} represents the relative motion of the mass with respect to the base motion, and it also indicates the degree to which the spring is relatively deformed. When considering $\mathbf{z} = \mathbf{0}$, the restoring force varies smoothly with changes in \mathbf{X} , but the force is not in a polynomial form. As a result, a Taylor series expansion is used to convert the force into a polynomial approximation.

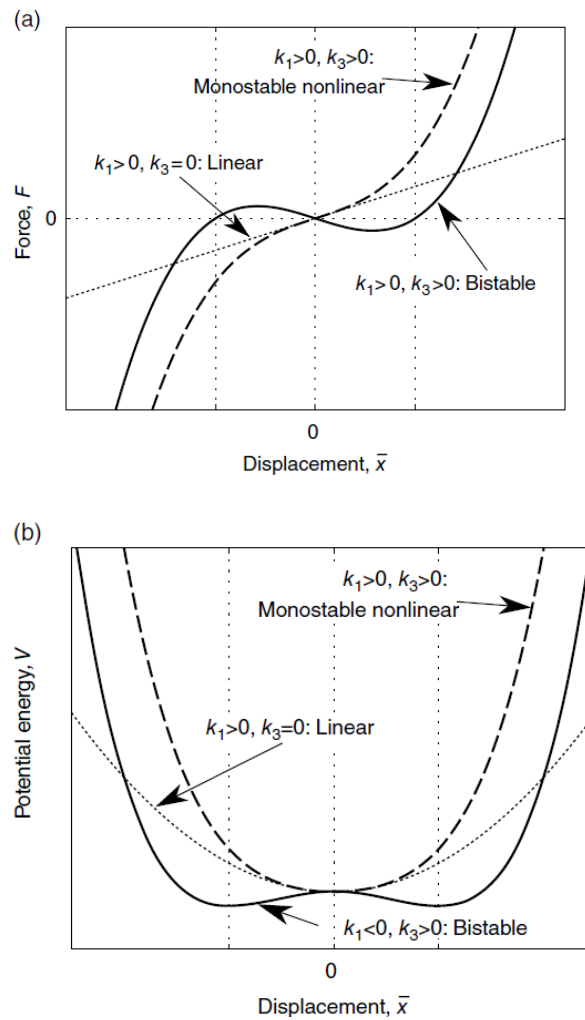


Figure 18: (a) Spring restoring force profiles for linear, monostable hardening Duffing, and bistable oscillators, and (b) corresponding potential energy [8]

In the case of an asymmetric cubic oscillator the restoring force becomes:

$$F(X) = k_1 X + k_3 X^3 \quad (13)$$

While higher-order terms in \mathbf{X} are removed from the expansion, it is assumed that the displacements from $\mathbf{x} = \mathbf{0}$ are finite but sufficiently small, such that the contributions from higher-order terms to the restoring force are negligible. By the expansion, the coefficients are found to be

$$k_1 = 2k \left(1 - \left(\frac{l_0}{d} \right) \right) \quad (14)$$

$$k_3 = k \frac{l_0}{d^3} \quad (15)$$

Finally, although it is not strictly necessary to apply the theoretical techniques detailed below, the restoring force polynomials will be odd, meaning that $\mathbf{F}(\mathbf{X}) = -\mathbf{F}(-\mathbf{X})$.

When the oscillator has a spring stiffness constant $\mathbf{k}_1 = \mathbf{k} > \mathbf{0}$ and $\mathbf{k}_2, \mathbf{k}_3 = \mathbf{0}$, the force-displacement profile is linear, as shown in *Fig. 18a*, with the corresponding parabolic potential energy function depicted in *Fig. 18b*.

The symmetric, bistable oscillator force–displacement profile is shown in *Figure Fig. 18a*, where negative linear ($\mathbf{k}_1 < \mathbf{0}$) and positive nonlinear ($\mathbf{k}_3 > \mathbf{0}$) terms contribute to the stiffness of the system. Often, the governing equation is expressed using positive stiffness coefficients such that

$$m\ddot{x} + d\dot{x} + k_1x + k_3x^3 = 0 \quad (16)$$

The fixed points $\mathbf{x}^* = [x_1^*, x_2^*]^T = [x^*, \dot{x}^*]^T$ of the bistable system are determined from

$$\begin{bmatrix} \frac{k_1}{m}x_1^* - \frac{k_3}{m}x_1^{3*} - \frac{d}{m}x_2^* \\ x_2^* \end{bmatrix} = \begin{bmatrix} 0 \\ 0 \end{bmatrix} \quad (17)$$

Computing Eq. (17) reveals three fixed points: $\mathbf{x}_1^* = [0,0]^T = \mathbf{x}_{2,3}^* = \left[\pm \sqrt{\frac{k_1}{k_3}}, 0 \right]^T$

The stability of the configurations must be evaluated following the linearization of the governing equation. The transformed variable, denoting small displacements around one of the equilibria, $\mathbf{y} = \mathbf{x} - \mathbf{x}^*$, is again employed. The Jacobian is then

$$\mathbf{D}_x \mathbf{f}(\mathbf{x}^*) = \begin{bmatrix} 0 & 1 \\ \frac{k_1}{m} - \frac{3k_3}{m} x_1^2 & -\frac{d}{m} \end{bmatrix}_{x=\mathbf{x}^*} \quad (18)$$

For clarity in the following developments, the following parameter values are used: $m = 1 \text{ kg}$, $k_1 = 1 \text{ N/m}$ and $d = \gamma \text{ Nsm}^{-1}$. Then, for $\mathbf{x}_1^* = [0,0]^T$, the linearized system is

$$\dot{\mathbf{y}} = \mathbf{D}_x \mathbf{f}(\mathbf{x}_1^*) \mathbf{y} = \begin{bmatrix} 0 & 1 \\ 1 & -\gamma \end{bmatrix} \mathbf{y} \quad (19)$$

while for $\mathbf{x}_{2,3}^* = \left[\pm \sqrt{\frac{k_1}{k_3}}, 0 \right]^T = \left[\pm \sqrt{\frac{1}{k_3}}, 0 \right]^T$, the linearized systems are both found to be

$$\dot{\mathbf{y}} = \mathbf{D}_x \mathbf{f}(\mathbf{x}_{2,3}^*) \mathbf{y} = \begin{bmatrix} 0 & 1 \\ \frac{k_1}{m} - \frac{3k_3}{m} k_1 & -\frac{d}{m} \end{bmatrix} \mathbf{y} = \begin{bmatrix} 0 & 1 \\ -2 & -\gamma \end{bmatrix} \mathbf{y} \quad (20)$$

Recall that the eigenvalues of the characteristic equation of the linearized governing equations (for the underdamped system, $0 < \gamma < 1$) are determined using:

$$\lambda_{1,2} = \frac{1}{2} [\text{tr}[A] \pm \sqrt{\Delta}] \quad (21)$$

Here $A = \mathbf{D}_x \mathbf{f}(\mathbf{x}_1^*)$ and $\Delta = \text{tr}[A]^2 - 4 \det[A]$. Then, considering Eq. (21), it is found that $\text{tr}[A_{x_1^*}] = -\gamma$, while $\det[A_{x_1^*}] = -1$.

Consequently, the eigenvalues are

$$\lambda_{1,2} = \frac{1}{2} \left[-\gamma \pm \sqrt{\gamma^2 + 4} \right]. \quad (22)$$

For such underdamped systems, the eigenvalues contain a positive real component, which indicates the local equilibrium $\mathbf{x}_1^* = [0,0]^T$ is unstable when subjected to small perturbation.

Repeating this procedure for the fixed points $\mathbf{x}_{2,3}^*$, the eigenvalues are:

$$\lambda_{1,2} = \frac{1}{2} \left[-\gamma \pm \sqrt{\gamma^2 + 8} \right]. \quad (23)$$

Therefore, the eigenvalues always contain negative real components, indicating stability of the two fixed points $\mathbf{x}_{2,3}^*$: hence, bistability.

In conclusion, the theoretical developments indicate that the bistable system has two stable configurations, with an unstable equilibrium between them. When the system is initially in the unstable position, small perturbations cause the mass to move toward one of the nearby stable configurations.

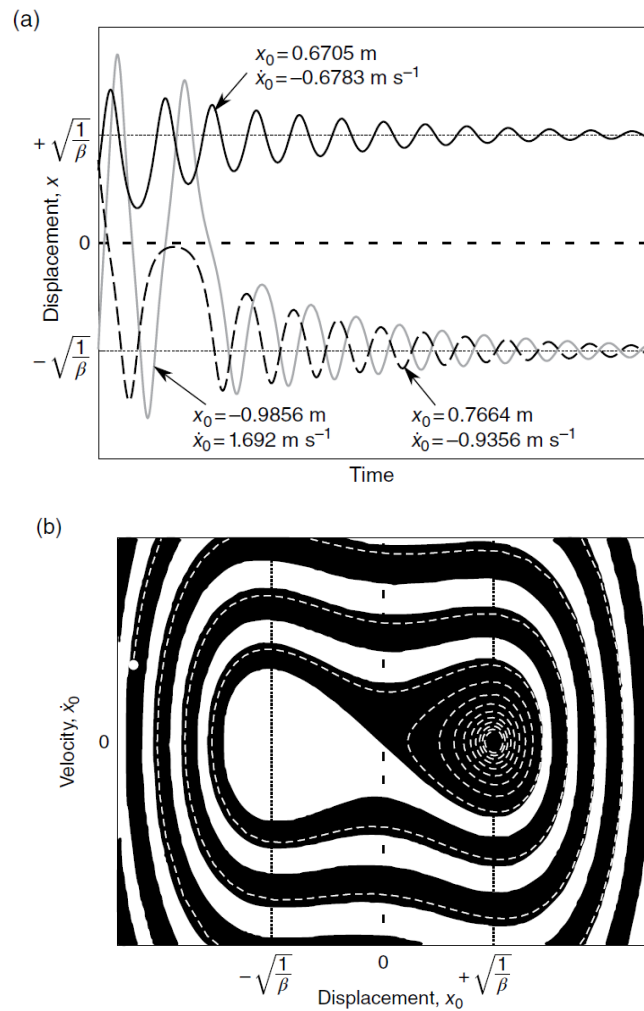


Figure 19: Example of free response displacement time series of bistable system. (b) basin of attraction map with single example case of phase portrait free response overlaid as light dashed curve, $\beta=1$, $\gamma=0.1$ [8]

In contrast to linear systems, many nonlinear systems, when driven by single-frequency excitations, can exhibit one or more forms of steady-state responses that coexist under the same excitation conditions. This coexistence of dynamic responses implies that, for a given set of design parameters, excitation level, and frequency, the nonlinear system may undergo different dynamics over time. Typically, these dynamics involve one of two distinct harmonic response amplitudes. The specific dynamic response that occurs depends on the system's initial conditions at the start of the single-frequency excitation.

In the case of bistable systems, several types of single-periodic steady-state dynamics may coexist. These can be classified into two main regimes: **intrawell oscillations** and **interwell oscillations**. Intrawell oscillations occur around one of

the two stable equilibrium positions, while interwell oscillations involve the system vibrating across the unstable equilibrium twice per excitation cycle. The potential energy profile of bistable systems, often referred to as the "double-well potential," visualizes these dynamics. The terms "intra-well" and "inter-well" describe whether the oscillations remain confined to one of the local wells of potential energy or cross back and forth between them, respectively.

These two dynamic regimes **intra-well** and **inter-well** can further be categorized into low and high amplitude versions, depending on the intensity of the input. It is important to highlight that the type of oscillation in a bistable system is strongly influenced by the intensity of the input excitation. When the energy is contained within the system, the system exhibits **non-linear behavior** due to the assumption of $k_1 < 0$, and the system will undergo oscillations around its equilibrium point (intra-well oscillations). However, when the input energy is sufficient to overcome the potential barrier between the stable equilibria, the system transitions between states and is described by **inter-well oscillations**, which are a result of the system crossing between equilibrium states.

3.0 Technology of the metapanel unit cell

3.1 Snap-through and bistability of the sinusoidal beam

Negative stiffness (NS) and multistable mechanical metamaterials have gathered significant attention over the past decade due to their promising applications in areas such as wave control, deployable structures, and energy absorption[6]. A deployable structure with multistable properties remains stable after undergoing deployment deformation. In the energy absorption domain, NS and multistable metamaterials can achieve high energy absorption efficiency. Moreover, NS structures enhance response rates through their snap-through behaviour.

It is important to note that multistable materials typically exhibit negative stiffness when subjected to loading. Negative stiffness describes a condition where a material or system displays an inverse relationship between force and displacement over a specific range of deformation. Simply put, in a negative stiffness element, the force applied decreases as the displacement increases, in contrast to the typical positive stiffness behaviour where force increases with displacement.

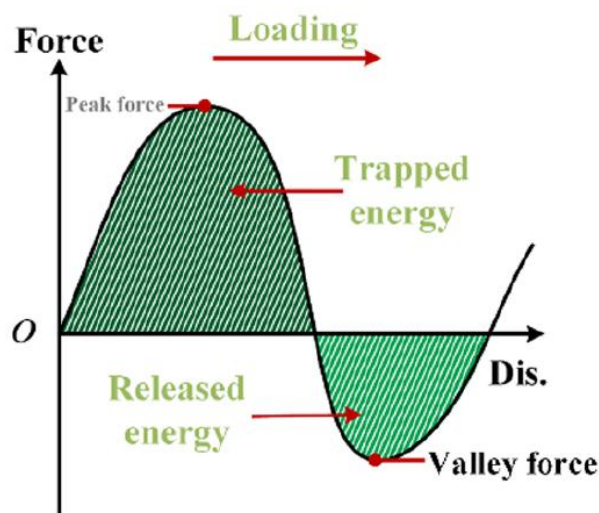


Figure 20: Energy trapping mechanism[6]

The following descriptions outline the behaviours of bistable materials with negative stiffness, which form the basis of the literature and this paper, particularly drawing from the studies of Tan [6], Chen [10]. These studies emphasize the positive aspects of the structures, with bistability (and snap-through) being among the most notable features.

The principal investigated objectives are several beam elements, tilted beam, curved beam, and arched beam, as depicted in Fig. 1. The shape of tilted beams can be determined by three geometric parameters, span, $2L$, thickness, t , and height, h . The beam element in Fig. 1 is all the uniform cross-section, these beam elements are all symmetrical structures.

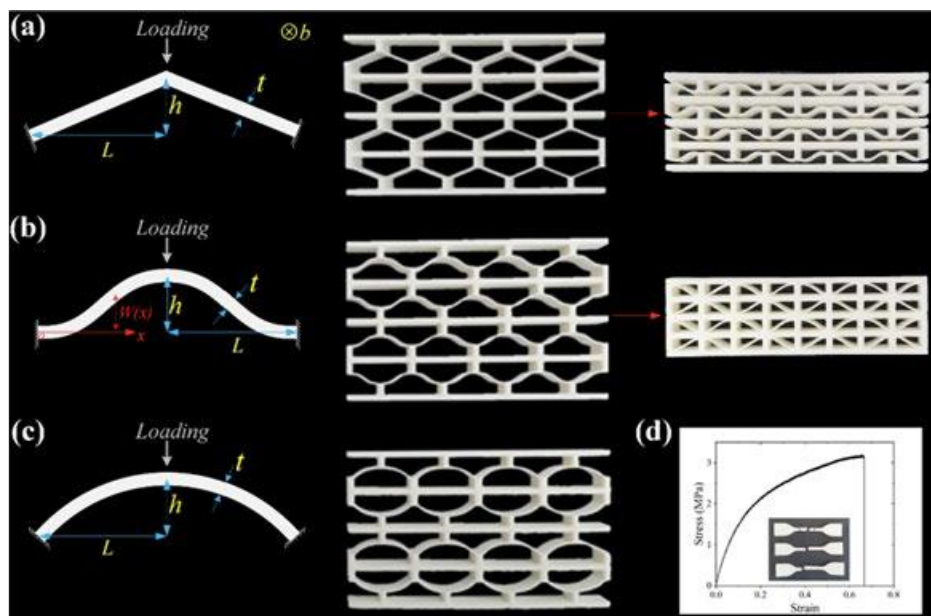


Figure 21: Inclined, curved, and arched beams [6]

The authors present a detailed experimental and numerical approach to evaluate the mechanical properties of beams with negative stiffness and bistable behaviour. The beam samples, designed in various configurations (inclined, curved, and arched), were fabricated using SLS (Selective Laser Sintering) technology with TPU (thermoplastic polyurethane). Mechanical tests were carried out to verify the stress-strain response curve of the material by varying geometric parameters such as beam thickness, height, and length.

The study compares the results obtained from mechanical tests with those from FEM analysis. The force-displacement response curves of the studied structures, consisting of inclined, curved, and arched beam elements, are shown separately in *Fig. 21*, and the corresponding deformation processes are illustrated in *Fig. 22*. These structures are all assembled with 4×4 beam elements. The peak force, or the instability force for the inclined and curved beam structures, is almost identical, but it is significantly higher than that of the arched beam structure for the specified geometric dimensions ($t = 0.6$ mm, $h = 4$ mm, $L = 20$ mm, and $b = 1.5$ mm). The global deformation processes for all shapes are similar, with no unique deformation modes emerging with the introduction of curvature. The structures collapse layer by layer and exhibit serrated and periodic mechanical response curves.

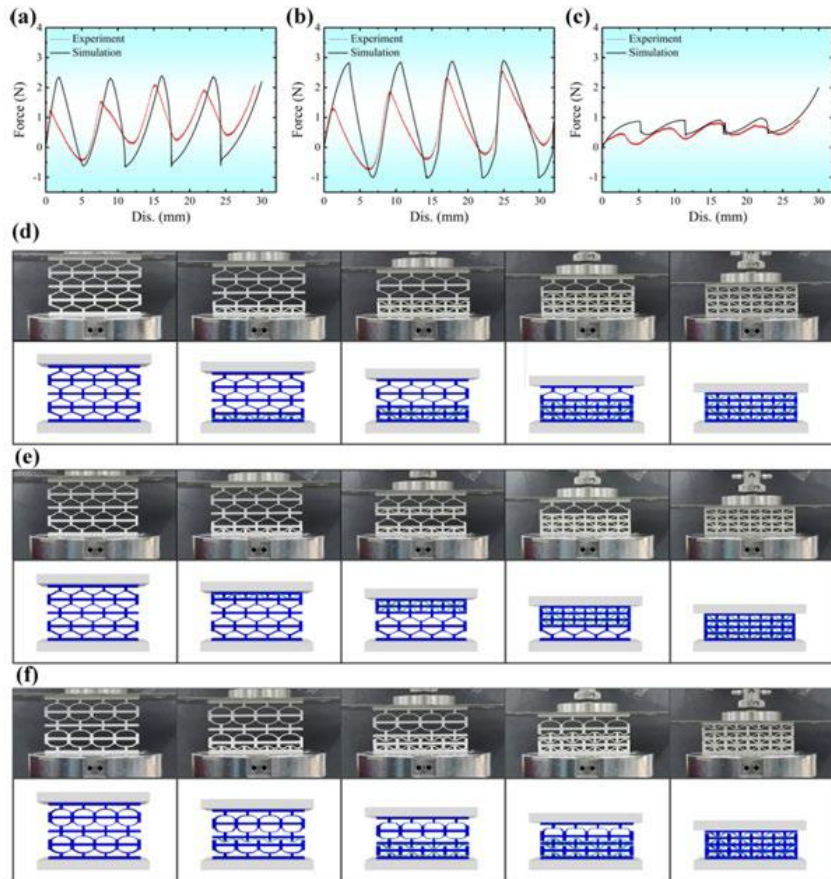


Figure 22: Force-Displacement curves for beams a) inclined, b) curved e c) arched [6]

In the same study previously cited, the different responses of bistable structures to variations in geometric parameters are highlighted. It is observed from the force-

displacement response curves that both the peak force and the initial stiffness increase as the ratios of h/L and t/L increase.

However, the relationship between the minimum force (valley force) and these parameter ratios is relatively complex. The valley force of the inclined beam increases as t/L increases and decreases as h/L increases, as shown in Fig. 45. The relationship between the valley force and the parameter ratios for the curved beam follows the same trend as that of the inclined beam. For the arched beam element, the relationship between the valley force and the parameter ratios is more apparent: the valley force increases with both h/L and t/L , as can be seen in Fig. 23.

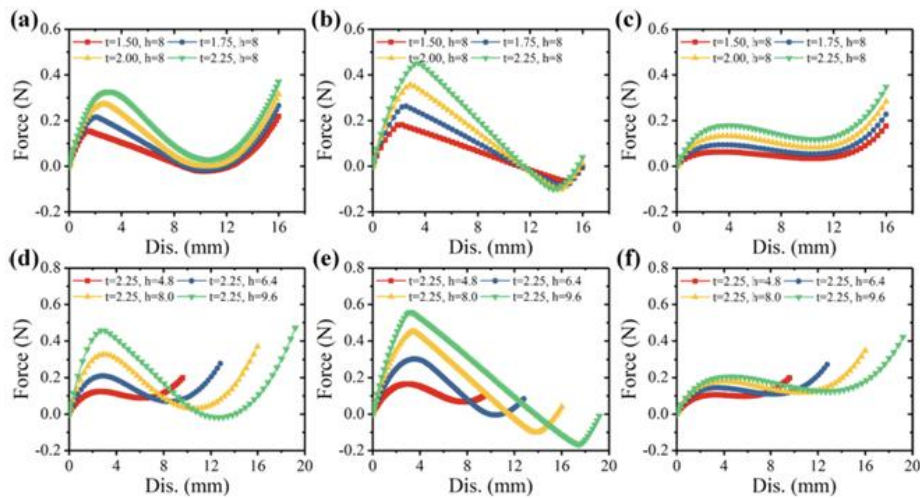


Figure 23: Force-Displacement diagrams for beams: a) Inclined, b) Curved, c) Arched, varying with geometric parameters [6]

The study also presents the deformation processes for these three beam elements, shown in Fig. 46. Their deformation modes are all identical. The stress is primarily concentrated at the ends of the beams, while there is little stress in the central part of the beams when they are fully compressed.

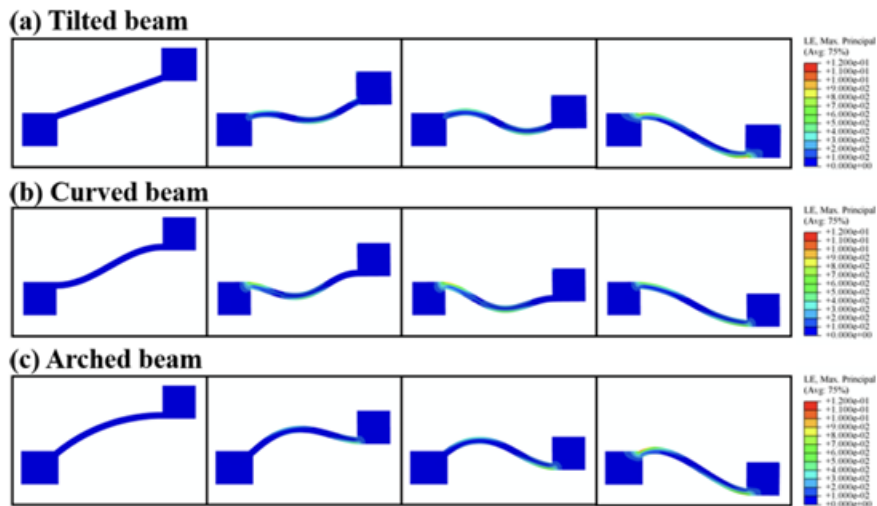


Figure 24: Deformation process [6]

As can be seen, the study highlights that, for the ratios $h/L = 0.64$ and $t/L = 0.08$, both the inclined and curved beam elements are bistable, while the arched beam element is monostable. In the case of the ratios $h/L = 0.64$ and $t/L = 0.125$, the inclined beam also exhibits a monostable behaviour.

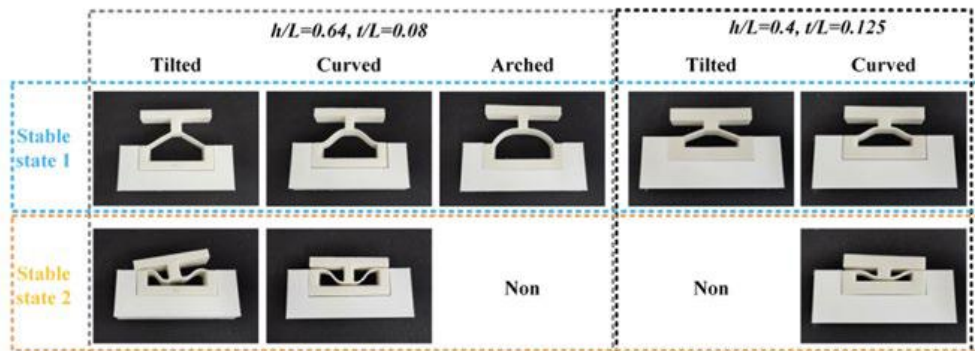


Figure 25: Comparison of bistability [6]

Another article addressing the topic of bistability in structures is Chen [10], which proposes a honeycomb structure for energy absorption. This study also focuses on designing an innovative configuration in which the cells of the structure exhibit regular variations in stiffness, in contrast to traditional structures with uniform negative stiffness. The aim is to improve energy absorption and vibration control

through an optimized distribution of deformation. Through a combination of numerical simulations and experimental tests, the paper demonstrates how the structure can offer superior performance compared to conventional configurations, both in terms of energy absorption capacity and vibration isolation, opening up new possibilities for engineering applications.

The innovative structure presented in the cited article is shown in *Fig. 26* as a three-dimensional model, where each unit cell consists of stiffening walls and a sinusoidal beam. When a vertical force is applied to the center of the sinusoidal beam, the beam undergoes a buckling instability (elastic instability).

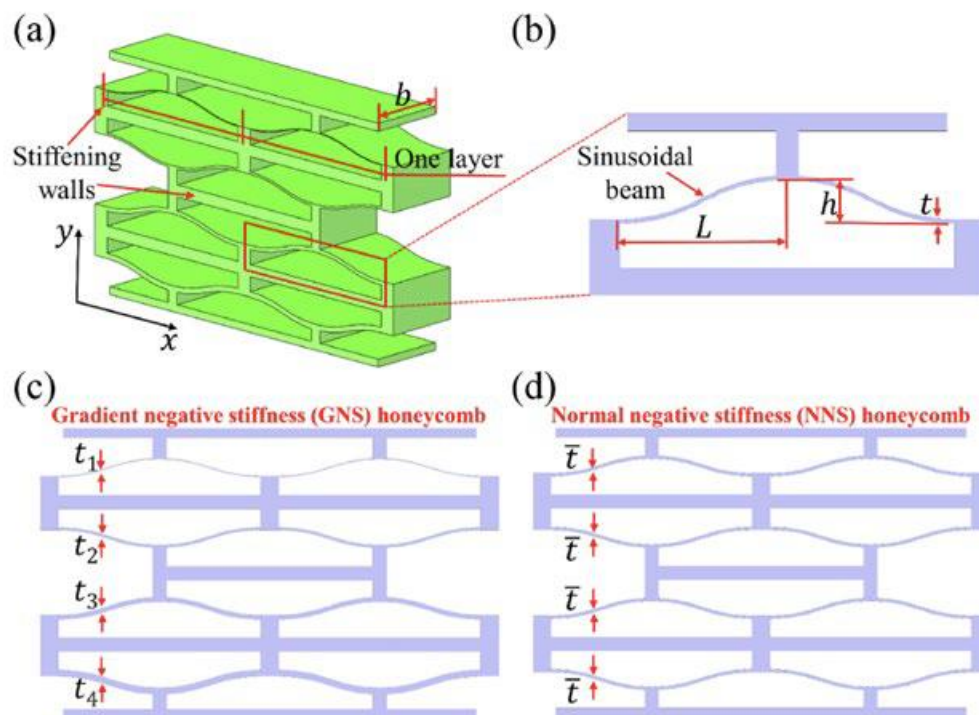


Figure 26: Geometry of GNS and NNS Configurations[10]

The geometry of the sinusoidal beam is expressed with a specific mathematical equation that represents the curve as a function of the beam's length and height. The geometric parameters of the curved beam include the in-plane thickness (t), length (L), height (h), depth (b), and the number of cells in a layer (n). All the sinusoidal beams are connected by stiffening walls. The presence of these walls is crucial to prevent horizontal expansion of the curved beams, which would otherwise hinder the snap-through behaviour and reduce the negative stiffness effect.

This design allows the entire honeycomb structure to be built using units with beams of varying thickness, thereby ensuring a gradual variation of mechanical properties throughout the structure.

The manufacturing process of the structure discussed in the study is not traditional due to the complex geometry. Additive Manufacturing (AM), particularly Selective Laser Sintering (SLS), has proven to be the most suitable technique. SLS technology offers many advantages, including the ability to create complex, hollow structures in various materials and sizes with high printing precision (up to 0.05 mm), reduced production costs, and high material utilization, as the structure does not require supports during the fabrication process.

For the fabrication process, polyamide (PA) was chosen as the material due to its advantages in terms of cost, strength, ability to withstand high temperatures, and good ductility.

In this proposed study, all the experimental tests were accompanied by FEM analyses in order to compare the results. The study results highlight a different behaviour between two types of structures: Gradient Negative Stiffness (GNS) and Normal Negative Stiffness (NNS). The first is a structure designed with a stiffness gradient, meaning there are progressive variations in thickness within the structure, which helps improve the distribution of deformation. The second has structural units with uniform thickness, and as a result, all the cells react similarly during compression, without a gradual variation in stiffness between the layers.

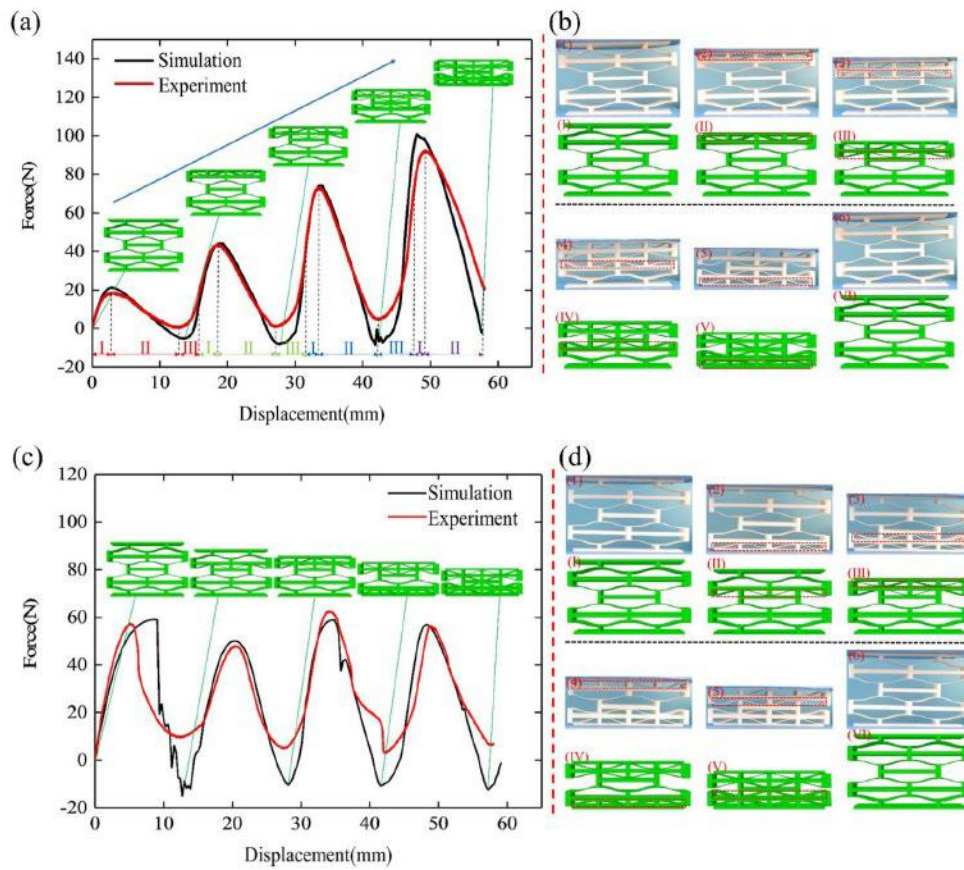


Figure 27: Force-Displacement Response of a) GNS and b) NNS [10]

The gradient configuration of GNS helps prevent local asymmetric instability. Deformation occurs in a more controlled and sequential manner, starting from the layers with smaller thickness and increasing with the rise in stiffness. On the other hand, NNS tends to develop local asymmetric instabilities even during compression. This instability can lead to sudden collapses in some layers, reducing the overall efficiency in energy absorption.

From the energy absorption performance perspective, GNS structures absorb more energy per unit mass compared to NNS, improving the specific energy absorption (SEA). The gradient design allows for maintaining a high level of absorption even after numerous compression cycles.

These results were confirmed by cyclic tests. Specifically, 30 cycles of compression and decompression were performed at a constant displacement rate of 5 mm/min

for both GNS and NNS configurations. In GNS, the mechanical properties change very little as the number of cycles increases. This indicates an elastic behaviour of the structure, which prevents the formation of unpredictable local plastic deformations.

These results confirm that the structure can withstand significant deformation without compromising its energy absorption capabilities.

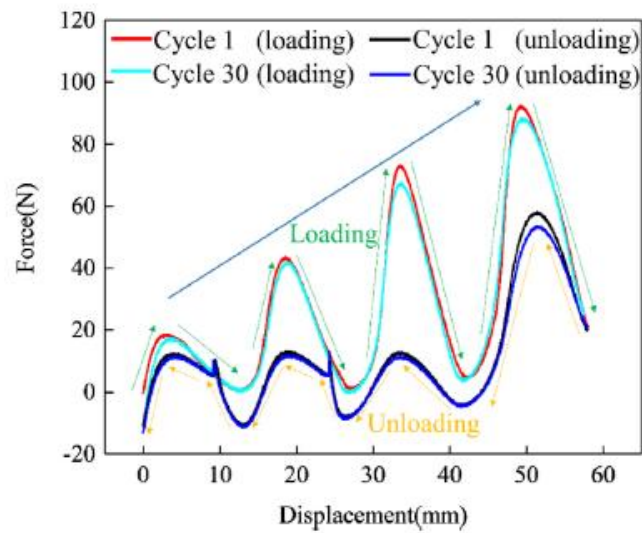


Figure 28: Force-Displacement Curve of the Cyclic Test in GNS [10]

NNS structures, while showing some resistance, are penalized by the absence of a stiffness gradient, which leads to local asymmetric instability and lower energy absorption performance.

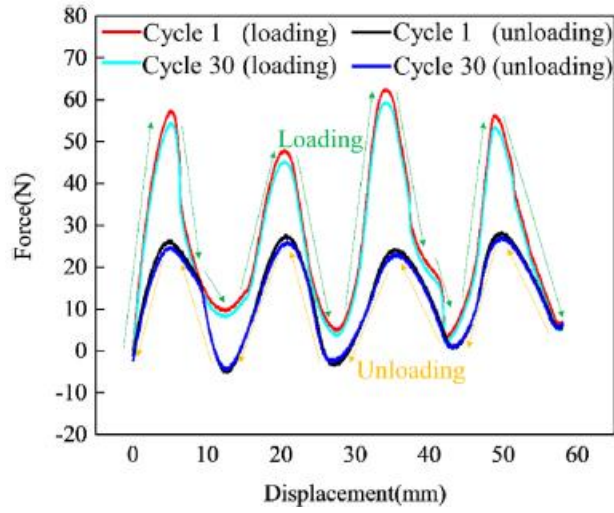


Figure 29: Force-Displacement Curve of the Cyclic Test in NNS [10]

A parameter that provides an indication of the absorbed energy is the MCF, or Mean Compression Force, which is the average force required to compress the honeycomb structure. This parameter is calculated as follows:

$$\text{MCF} = \frac{EA}{\delta} \quad (24)$$

Where:

- EA is the total energy absorbed during compression;
- δ is the total displacement during compression

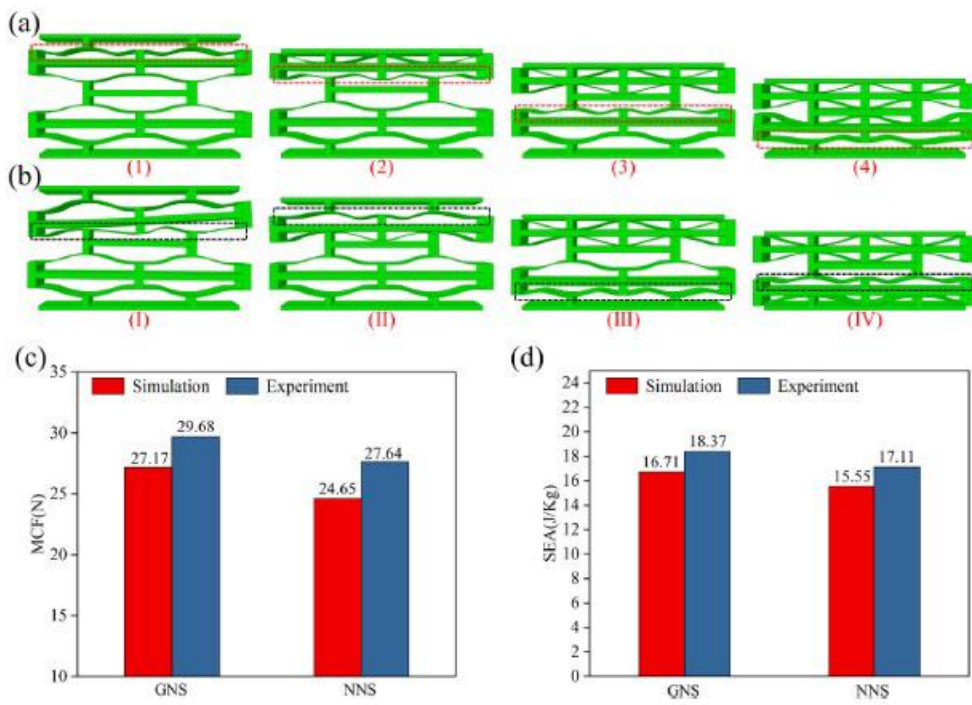


Figure 30: MCF and SEA for GNS and NNS [10]

This last set of data highlights once again how, in both considered parameters, GNS structures have a greater energy absorption capacity, both from an experimental and a simulation perspective

3.2 Metapanel modeling

3.2.1 Introduction to modeling

This chapter describes the modeling process of the device, designed to optimally respond to dynamic loads, such as those induced by seismic events.

The system described in *Fig.31* consists of vertical and horizontal rigid supports, on which we find the beam with a sinusoidal shape, connected at the top by a plate and a vibrating mass coupled to it. The system is entirely characterized by steel elements with variable thickness, which will be properly defined later.

The device exploits the properties of TMD through the vibrating steel mass and those of metamaterials through the sinusoidal panel.

This chapter details the principles of the analysis conducted, the assumptions made, the main geometric characteristic. Subsequently, the results of the time history analysis will be presented, confirming the achievement of the desired bistability and illustrating the behaviour of unit cell under seismic loads.

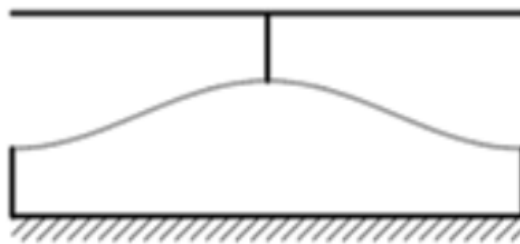


Figure 31: Generic representation of metapanel

3.2.2 Geometry and Materials of the Panel

The definition of the geometry is based on the sinusoidal Eq. (25), so the first step was the selection of the equation parameters.

$$y = \frac{h}{2} \left(1 + \cos \left(2 \pi \frac{x}{L_{tot}} \right) \right) \quad (25)$$

Where:

- $h/2$ is the amplitude of the sinusoid
- x it is the progressive distance
- L_{tot} is the total of the considered length

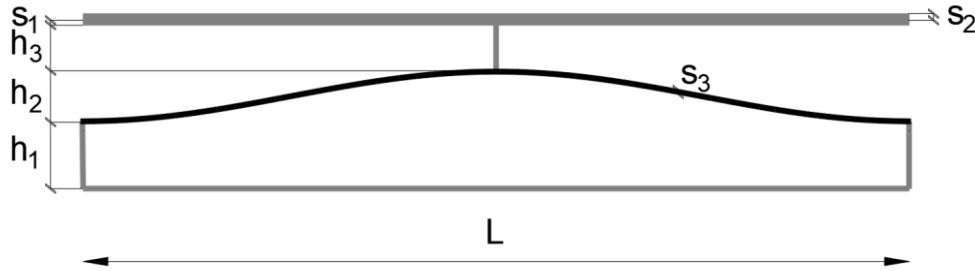


Figure 32: 2D representation of the metapanel

The metamaterial panel is divided into elements with different thicknesses. The vertical and horizontal supporting elements are described by a constant thickness of s_1 . The sinusoidal element, on the other hand, is described by a constant thickness of s_3 , while the vibrating mass located above the horizontal supporting element has a thickness of s_2 . The dimensions will be listed in the following table.

<i>Metapanel Dimensions</i>		
<i>Parameter</i>	<i>Value</i>	<i>Unit</i>
Length	0.50	m
Width	3.00	m
Thickness s_1	0.002	m
Thickness s_2	0.005	m
Thickness s_3	0.001	m

Table 1: Geometric dimensions of the metapanel

3.2.3 Modelling with Cad

Representative images of the panel, created with AutoCAD, will be shown.. For further information, please refer to 4.2.

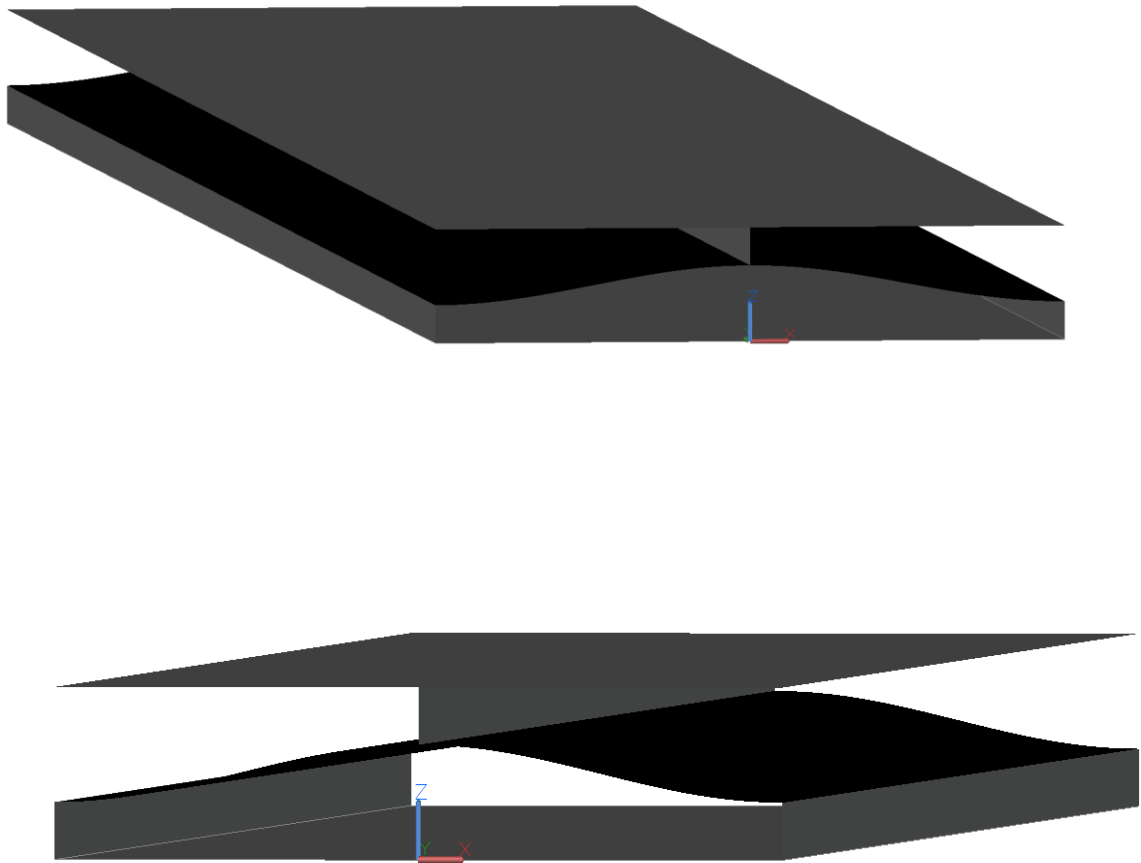


Figure 33: 3D representation of the metapanel

3.2.4 Modelling with Ansys

The modeling of this element and the vibrating mass were made possible by inputting the values of the material types used. The values applied will be provided below.

$$E = 210000 \frac{N}{mm^2}$$

$$\nu = 0.3$$

$$\gamma = 7850 \frac{kg}{m^3}$$

The software used for modeling is Ansys, two types of analyses were performed: the modal analysis and the transient analysis. For further information, please refer to chapter 4.2.

In this case, the transient analysis is a **nonlinear dynamic analysis** due to the large displacements experienced by the element (geometric nonlinearity). To determine the correct type of input for the bistability search, preliminary evaluative analyses were conducted. Indeed, the transient analysis required a high computational cost, both in terms of execution time and space required to store the data. To address this issue, the system depicted above was assumed to be a Single Degree of Freedom (SDOF) system, and its resolution was carried out using Matlab.

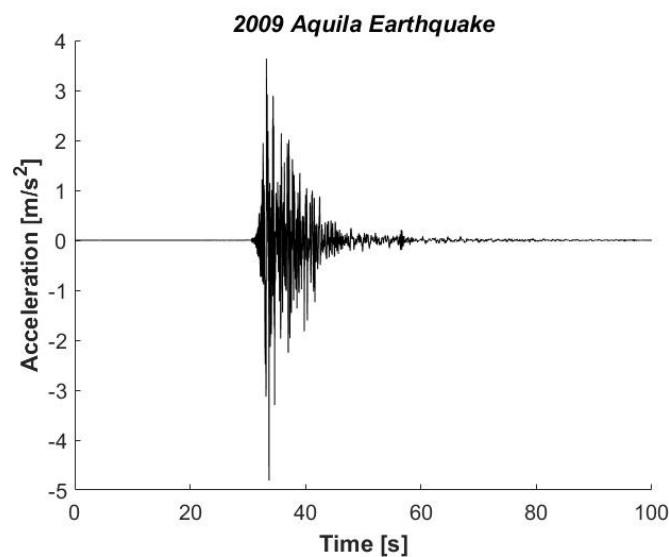


Figure 34: Aquila earthquake

3.2.5 Modelling with Matlab

To solve and describe SDOF that exhibit nonlinear stiffness i.e. an increase in deformation associated with a reduction in load, as in our case, the bistability was modelled using a modified Duffing equation. [8]

$$m\ddot{x} + d\dot{x} + k_1x + k_3x^3 = F(t) \quad (26)$$

The Duffing model, depending on the positive or negative values of the coefficients k , describes different conditions. In our case, to describe the bistability of an SDOF system, it was necessary to impose the values $k_1 < 0$ and $k_3 > 0$. The input data $F(t)$ is any function that depends on time, in our case it will be the earthquake.

This type of modeling and its simplification were made possible through the comparison of modal frequencies. The model initially analysed with Ansys, as an MDOF (Multiple Degrees of Freedom), provided the same modal frequency values as those obtained from an SDOF (Single Degree of Freedom) model analysed via Matlab.

This problem is solved by **ode45** which is a numerical tool used to solve first-order ordinary differential equations (ODEs). It applies a version of the 4th/5th-order Runge-Kutta method, which is an adaptive method capable of effectively and accurately solving both linear and nonlinear equations. Once the system is defined, the method numerically integrates the equations over the points in the specified time interval. The time step, which represents the difference between consecutive points where the solution is calculated, is automatically chosen by the method based on the need to maintain a specified level of accuracy. This adaptive approach allows **ode45** to solve the system with good precision while maintaining computational efficiency. The input value used is the L'Aquila earthquake shown in figure *Fig34*.

3.2.6 Results

Modal analysis

The following images show the deformations of the metapanel. It is important to note that the images are not to scale in order to provide a better view. The colours indicate the magnitude of the deformation, as described by the bar at the bottom of each image

<i>Modal frequencies</i>		
First mode	4.05	Hz
Second mode	15.53	Hz
Third mode	37.52	Hz

Figure 35: Modal frequencies of the metapanel

Matlab analysis

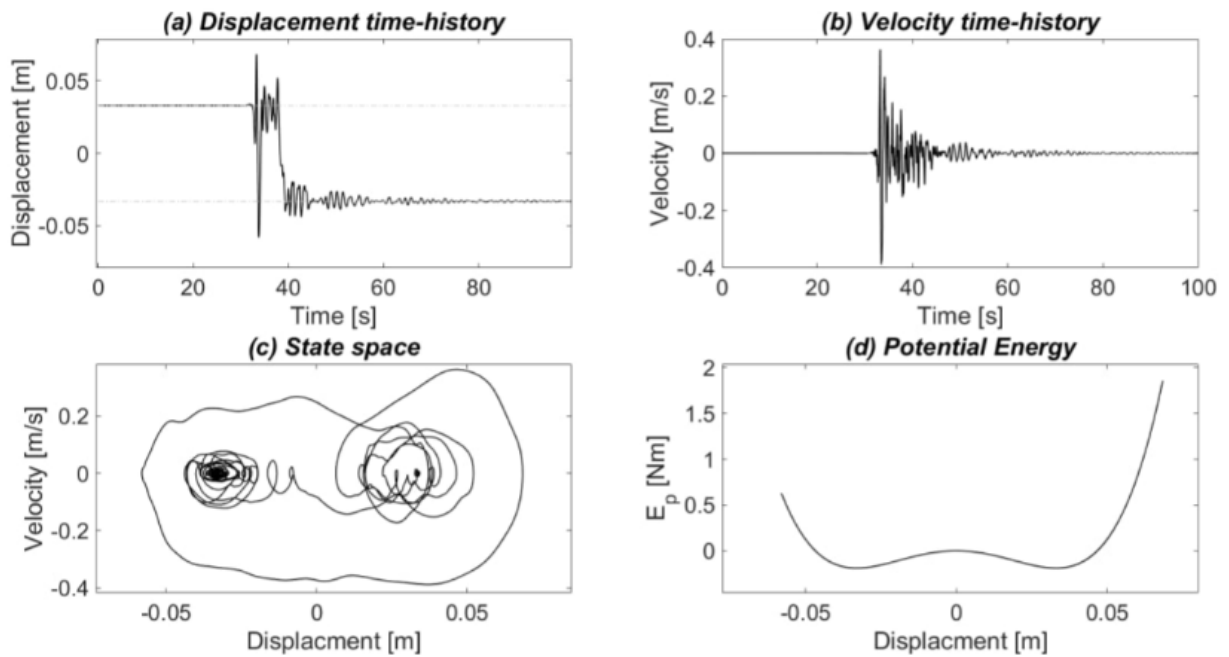


Figure 36: Results of Metapanel as SDOF

As shown in *Fig 36(a) (b)*, the metamaterial panel system is characterized by two types of oscillations: intrawell and interwell. Initially, around 20 seconds, the system experiences an input that is not contained, which leads to an initial intrawell oscillation. However, once the peak point is reached, the system transitions into an interwell oscillation, characterized by a significant deformation. After this phase, the system returns to its equilibrium state and begins oscillating around it. Then, around 40 seconds, the system "snaps" again, dissipating energy during the transition between the two equilibrium states. This is also illustrated by *Fig.36 (d)*, where the system, as a function of its deformation, assumes two distinct points of minimum potential energy. According to the principle of minimum potential energy, these correspond to stable equilibrium positions. *Fig. 36 (c)*, on the other hand, represents the solution of state space. It is possible to observe how the trajectories converge around two points on the graph, which, by virtue of this, are defined as equilibrium points.

The results obtained are a sequence of frames that have formed a video. In the following section, only some of them will be shown.

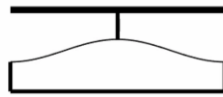
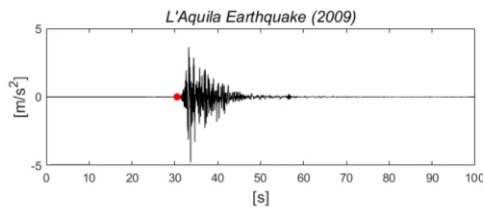


Figure 37: First equilibrium condition

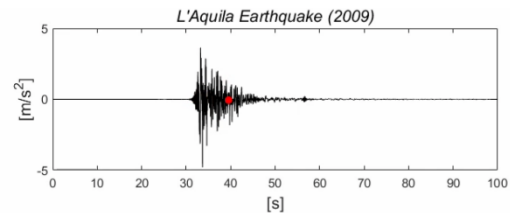


Figure 38: Second equilibrium condition

In *Fig. 37* and *Fig. 38* the two equilibrium configurations of the metapanel during the earthquake application are represented, showing how they change depending on the provided input.

4.0 Benchmark cases

This section of the thesis outlines the structural and geometric characteristics of the buildings considered in the analysis. These structures were designed based on those most commonly found across Italy. A total of eight models were created, varying in geometry and structural composition:

- 4 concrete structures:
 - 2 with square floor plans
 - 2 with rectangular floor plans
- 4 masonry structures:
 - 2 with square floor plans
 - 2 with rectangular floor plans

The individual structures will also be defined by a height that is the same for each pair. The two height configurations modeled are **16 meters** and **10 meters**, considering the ridge point. The aforementioned structures were subjected to both modal and transient analysis, and the results will be presented in the following chapters.

4.1.1 Reinforced concrete structure

The models of structures have different planimetric dimensions, in this case, the square plants have dimensions of 10x10m while the rectangular ones are 8x12m.

In both structures the presence of openings, such as doors and windows, have been provided, the dimensions are reported in detail in the following part.

These structures are made up of structural elements such as:

- Column
- Beams
- Slabs
- Infill walls

The dimensions of the structural elements were defined through pre-dimensioning, in this case it is necessary to define:

The column are 3 meters high for each floor, with dimensions 30x30 cm. The beams develop equal to the length of the perimeter of the structure, with dimensions of 30x30. As regarding slabs were also defined every 3 meters of height, with dimensions coinciding with the area. Furthermore, infill walls are defined by a height of about 3 m and a thickness of 20 cm all around the perimeter for each floor.

For further information on the structural features used, please refer to *4.2.1*

First square plan in reinforced concrete

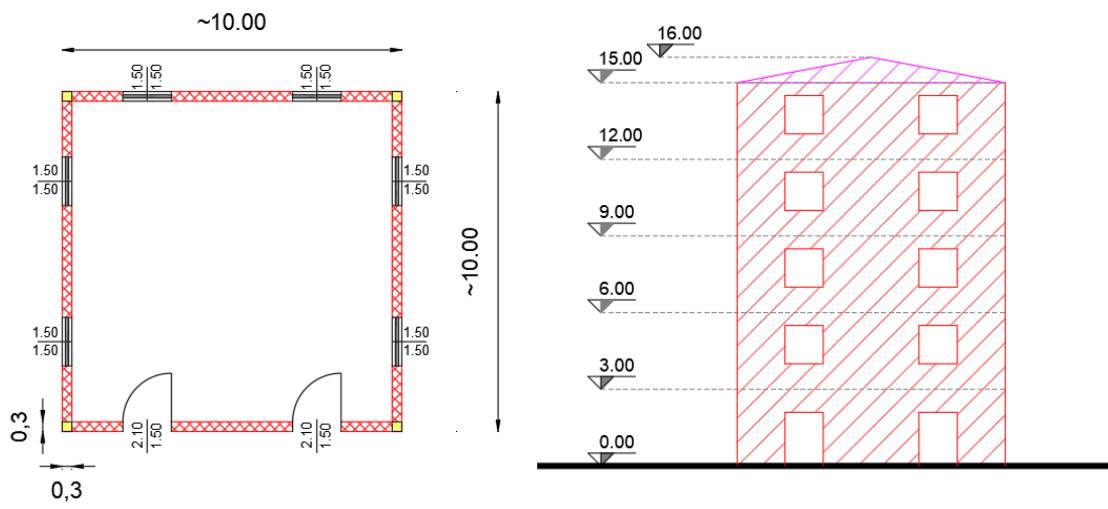
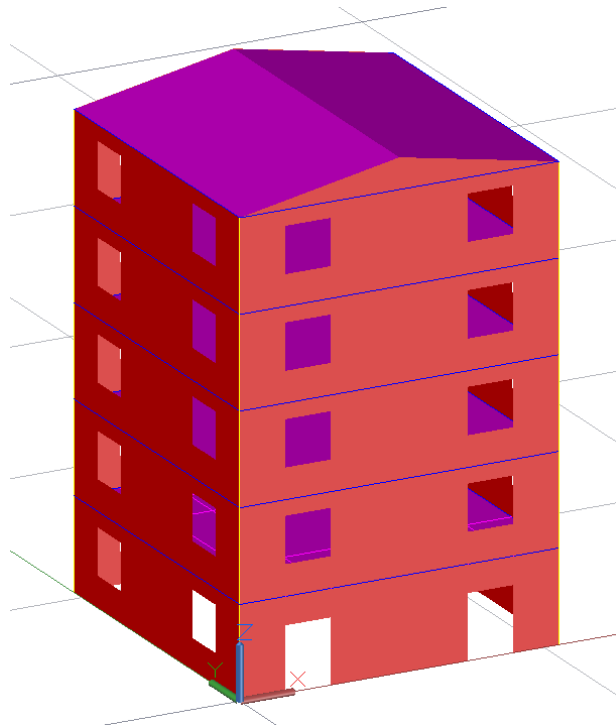


Figure 39: First typology of reinforced concrete building



Second square plan in reinforced concrete

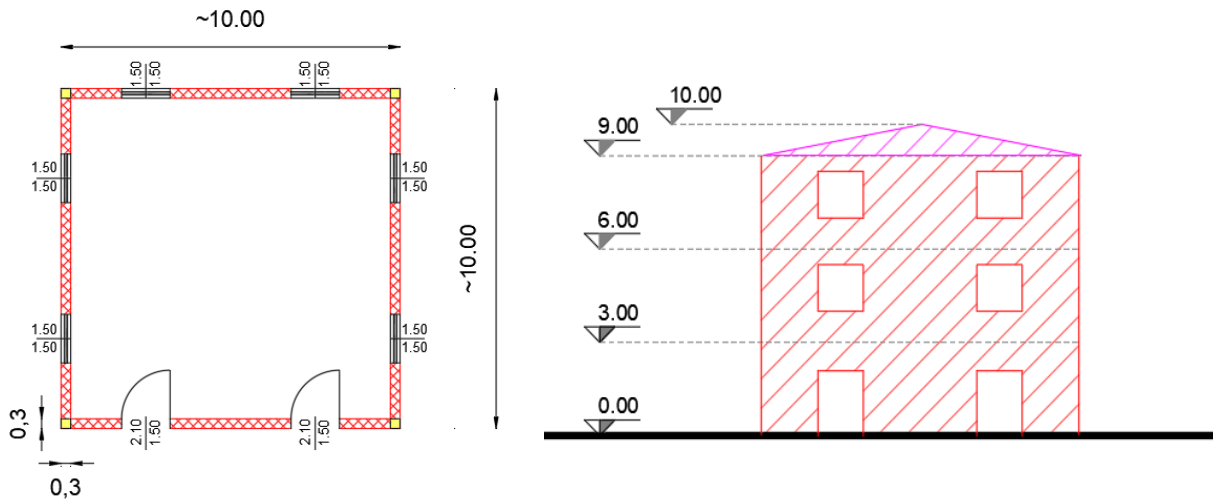
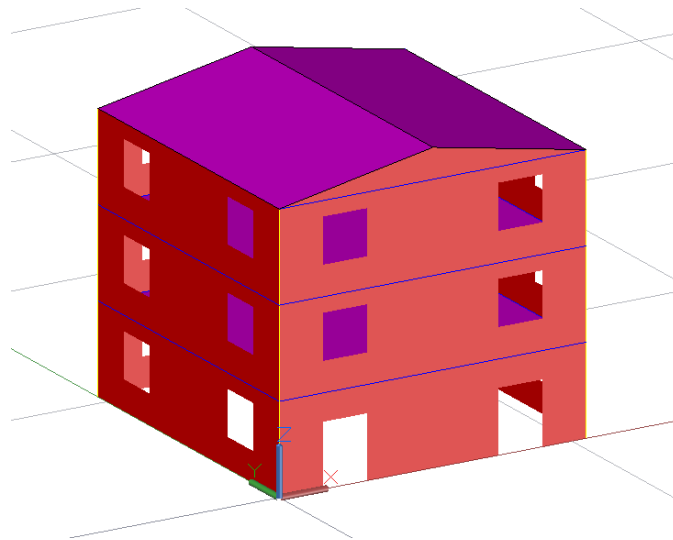


Figure 40: Second typology of reinforced concrete building



Third rectangular plan in reinforced concrete

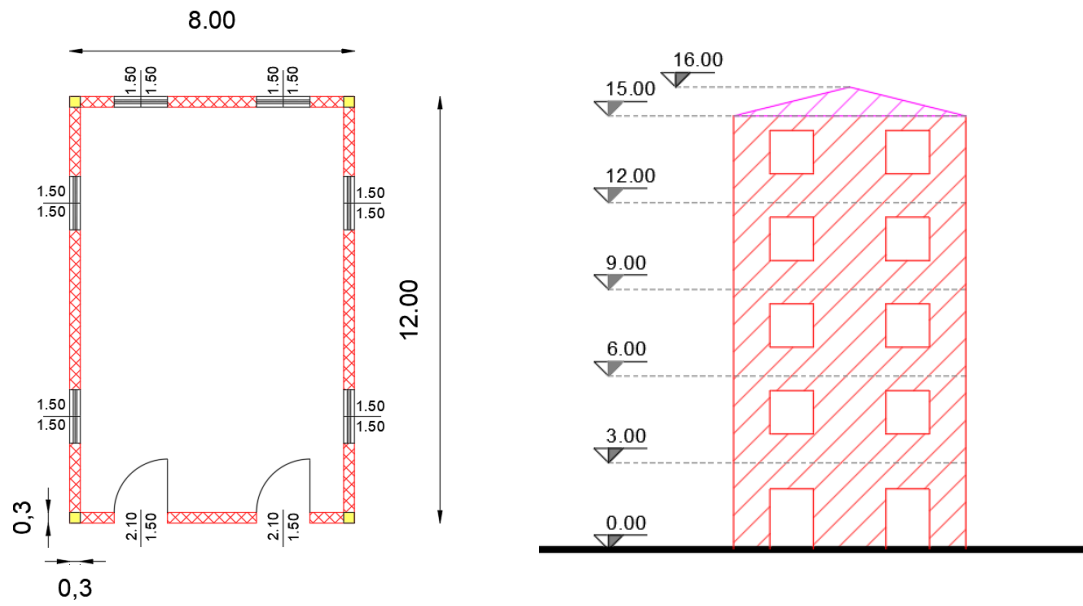
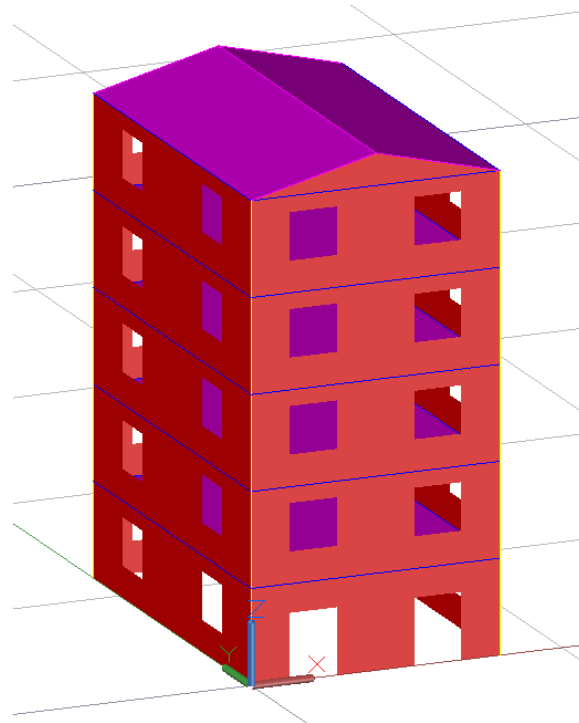


Figure 41: Third typology of reinforced concrete building



Fourth rectangular plan in reinforced concrete

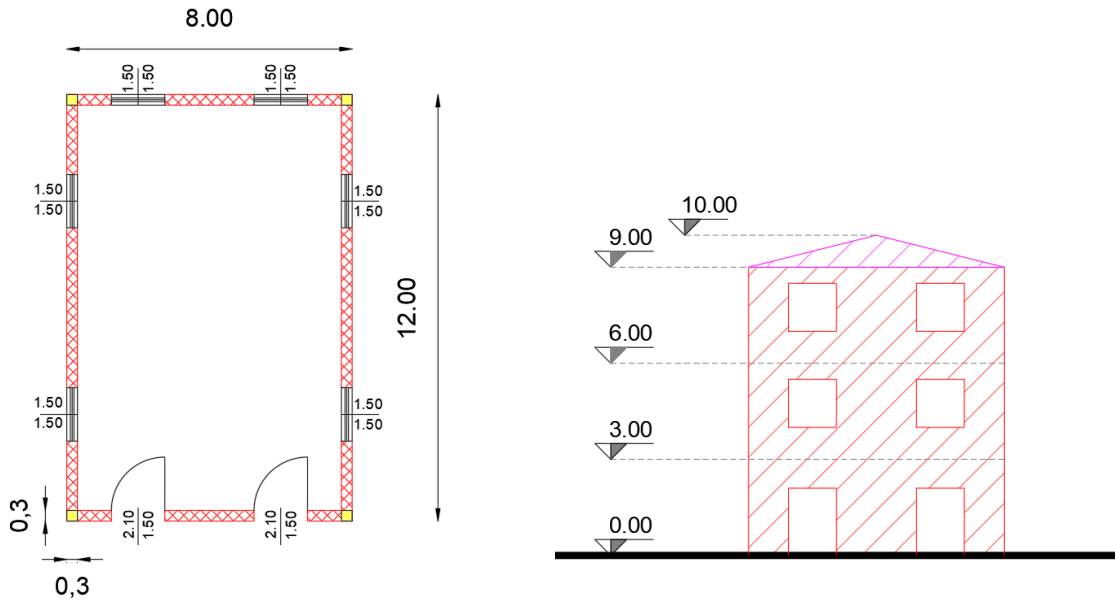
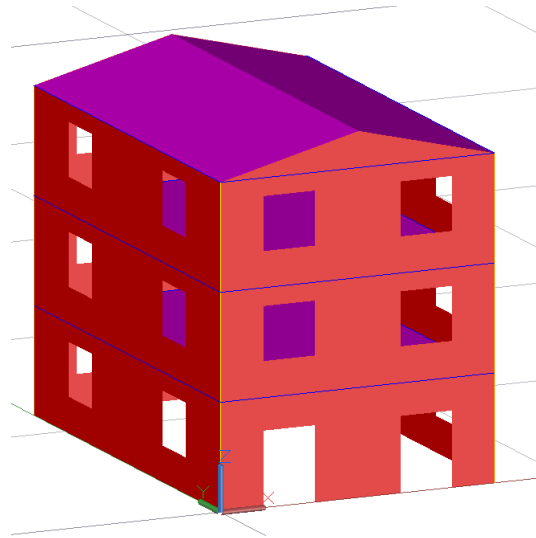


Figure 42: Fourth typology of reinforced concrete building



4.1.2 Masonry structure

These structures are made up of structural elements such as:

- load-bearing walls
- curbs
- slabs

The load-bearing wall was defined by a height of 3 m for each floor and a constant thickness along the entire perimeter equal to 40 cm. As regarding curb, with dimensions of 40x30 cm, placed at the top at a height of 3 meters for each floor, with the aim of ensuring a better distribution of the tensions. Furthermore, slabs were also defined every 3 meters of height, with dimensions coinciding with the area.

For further information on the structural features used, please refer to 4.2.2

First square masonry structure

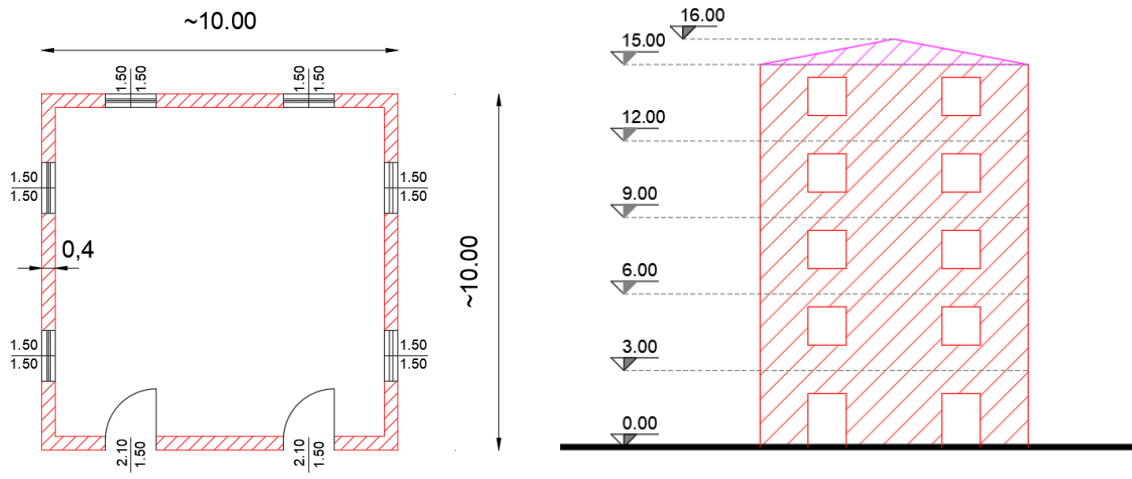
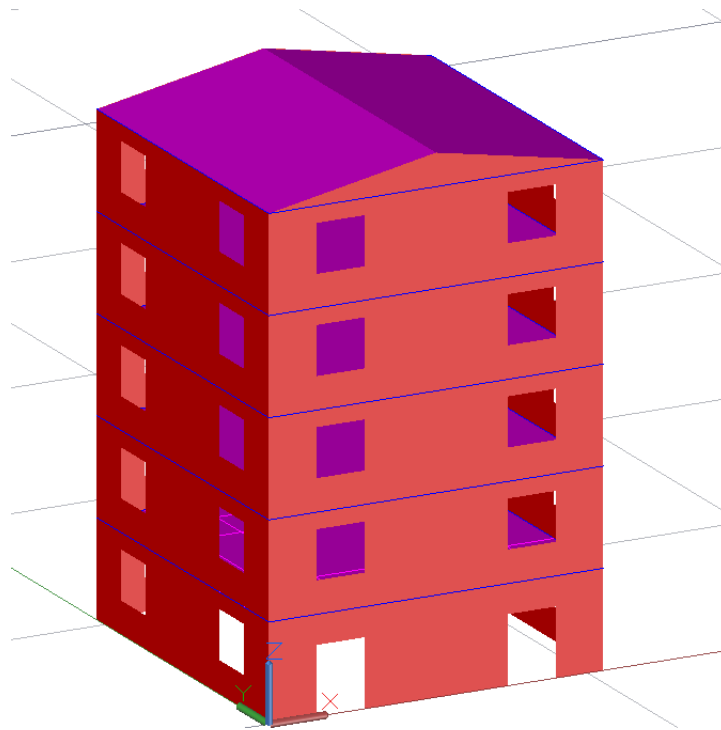


Figure 43: First typology of masonry building



Second square masonry structure

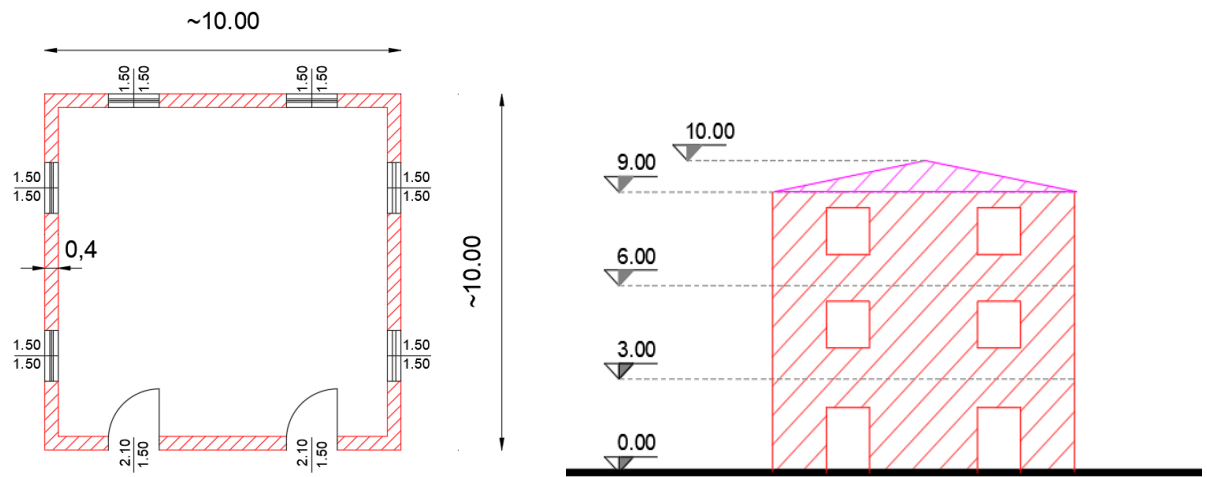
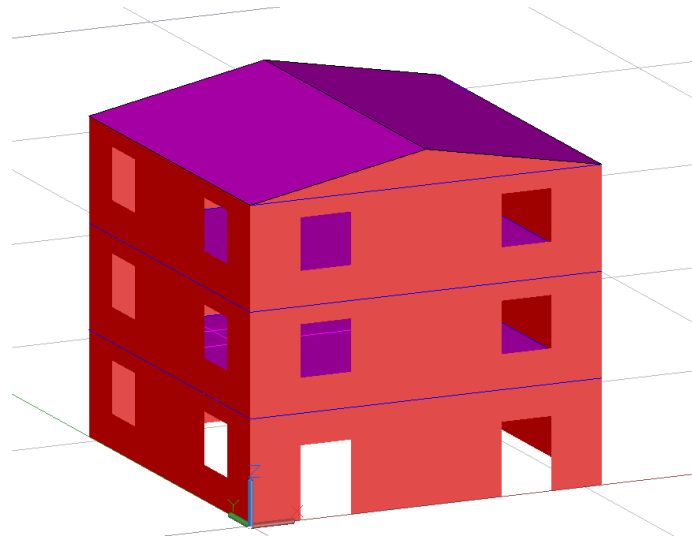


Figure 44: Second typology of masonry building



Third rectangular masonry structure

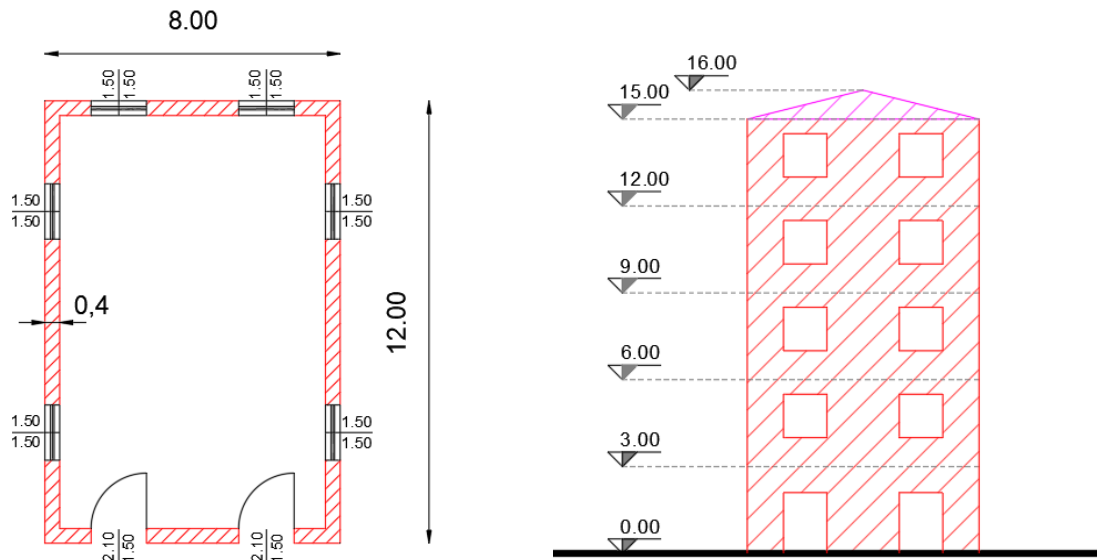
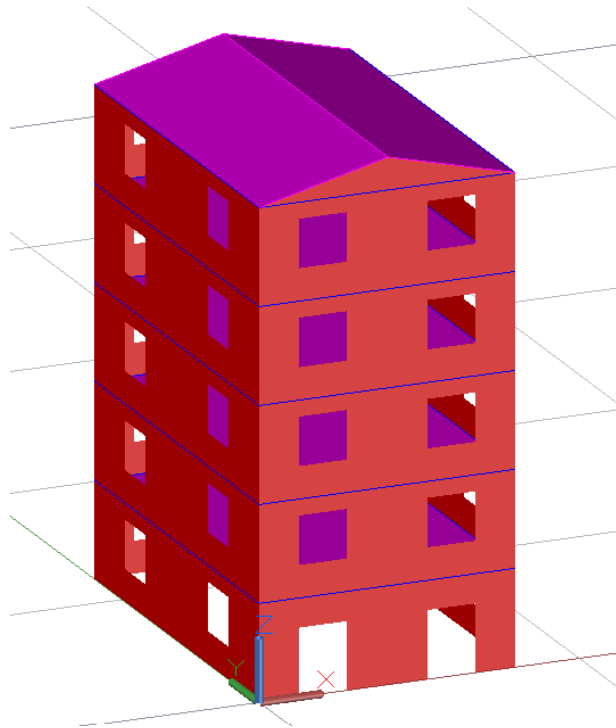


Figure 45: Third typology of masonry building



Fourth rectangular masonry structure

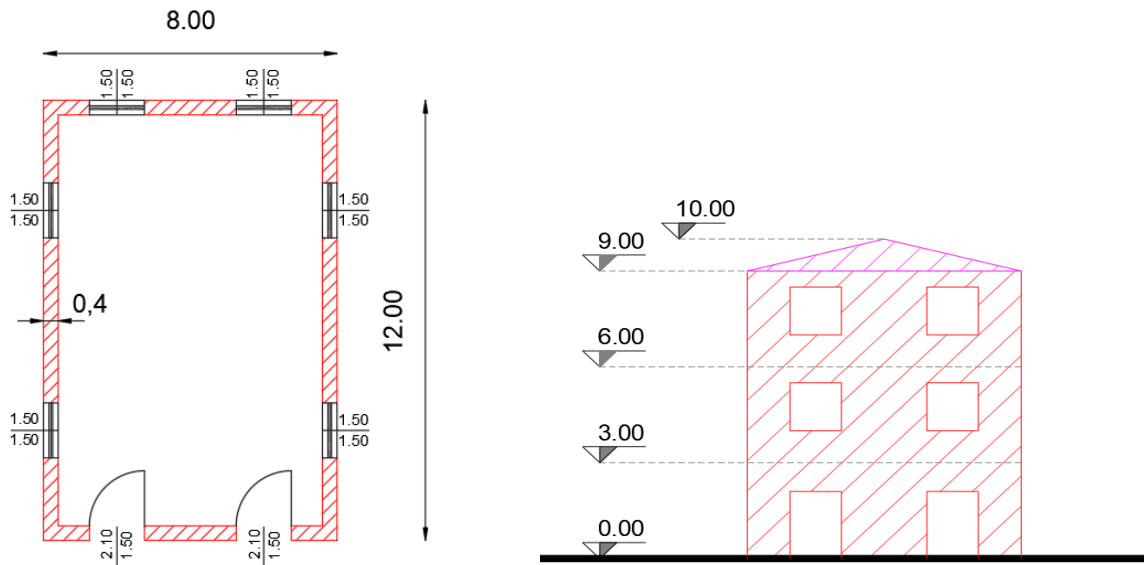
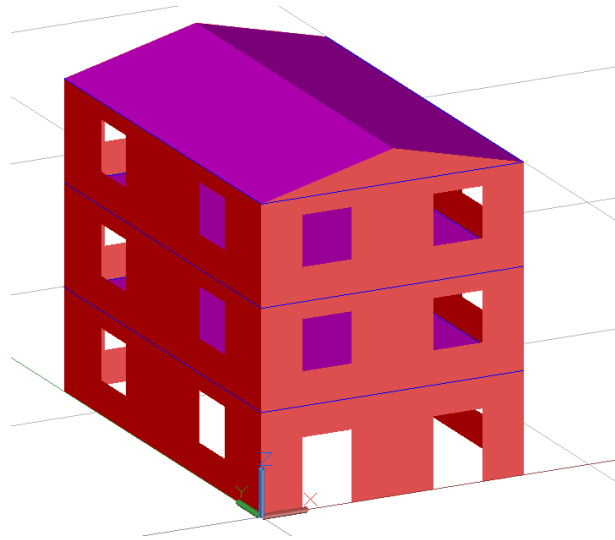


Figure 46: Fourth typology of masonry building



4.2 Finite Element Modelling

For this modeling, it was essential to divide the previous structural elements in AutoCAD and create the IGES file. An IGES file (Initial Graphics Exchange Specification) is a standard file format used to exchange graphic and geometric data between different Computer-Aided Design (CAD) software and simulation software. In fact, IGES formats were employed to represent various geometries, including curves, surfaces, and solids.

For each structure defined, it was necessary to create a code in a text file that was used in Ansys. This code contains a description of the characteristics of the structural system, including the use of various materials and types of elements to simulate the physical behaviour of the building.

Once the association between material and section has taken place, it is necessary to define the mesh of the individual elements which will then be assembled to obtain the entire structure.

The "mesh" in a FEM (Finite Element Method) software is a discrete representation of a geometric domain, subdivided into small elements (triangles, quadrilaterals, tetrahedra, etc.) that approximate a structure or material. Each element of the mesh is a small "brick" used to calculate physical properties such as deformations, stresses, and heat flux.

The mesh is crucial because it allows the finite element method to be applied to solve complex problems that cannot easily be analysed using analytical methods. The precision and accuracy of the solution directly depend on the quality and fineness of the mesh. A finer mesh, with many small elements, provides a more accurate solution but requires more computational power.

At this point the structure has been defined and as anticipated it has been subjected to a modal and a transient analysis.

Modal analysis

The modal analysis, , decomposes the dynamic response into the contributions of the individual modes of vibration, by transforming a system with N degrees of freedom into N systems with 1 degree of freedom. The structural response is obtained by superimposing the individual modes of vibration (modal superposition).

The modal analysis seeks the modes of vibration of a structure and, for each mode, calculates its natural vibration period, i.e., the time interval required for the structure to complete one full oscillation according to a deformation configuration similar to one of its modes of vibration. For a vibrating system, a general rule applies: the number of modes of vibration will be equal to the number of degrees of freedom of the system.

To define this problem, we begin with the general equation of motion for systems with N degrees of freedom.

$$[M]\{\ddot{x}\} + [K]\{x\} = 0 \quad (27)$$

Where:

$[M]$ is the mass matrix;

$\{\ddot{x}\}$ is the acceleration vector

$[K]$ is the stiffness matrix

$\{x\}$ is the displacement vector

The solution is determined by a spatial form and a temporal form of the following type:

$$\{x\} = \{\psi\}\varphi(t) \quad (28)$$

$$\{\ddot{x}\} = \{\psi\}\ddot{\varphi}(t) \quad (29)$$

By substituting into the equation of motion, the following is obtained:

$$[K]\{\psi\} - \omega^2[M]\{\psi\} = 0 \quad (30)$$

In this way, the eigenvalue and eigenvector problem is defined. By neglecting the trivial solution ($\{\psi\} = 0$), the following solution is found:

$$\det([K] - \omega^2[M]) = 0 \quad (31)$$

In this way, the modal frequencies ω of the system can be determined.

Thus, the eigenvalue problem is solved.

Time-history dynamic analysis

Transient analysis is a time history dynamic analysis technique used in engineering to study the response of a structure or system to forces that vary over time, such as a rapidly changing load or a dynamic event (like an earthquake or impact).

During a transient analysis, the structural response to a load that is not constant but varies over time is considered. This analysis allows for an understanding of the behaviour of the structure under complex time-varying stresses, such as accelerations or vibrations occurring within a specific time interval.

For this type of analysis, the 2009 L'Aquila earthquake and a wind load were used. As regarding the earthquake, the knowledge of acceleration as a function of time was possible to receive through the National Earthquake Observatory (ONT)[12]. The ONT is an organization that collects, monitors, and analyses seismic data in Italy. The observatory's role is to study and provide precise information on the country's geodynamics, the frequency and intensity of earthquakes, and their effects in various regions.

It is important to highlight that this earthquake was used to create a simulation of Italian buildings, as complete as possible.

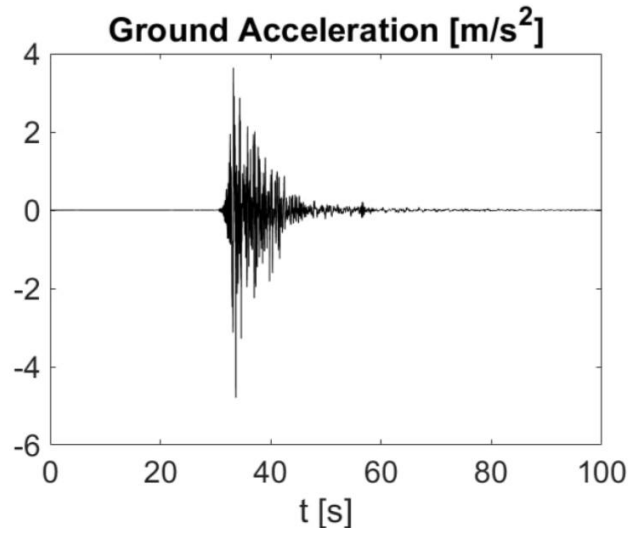


Figure 47: Seismogram of the Aquila earthquake

For this earthquake, a sampling time of 0.005 seconds was applied to the structures, with a duration of 100 seconds, which resulted in the analysis of 20,000 elements. In this case, the small displacement hypothesis was used for this transient analysis.

For additional information about the analytical procedure please refer to 2.2.1.

For the wind load, simulated wind signal was accessed thanks to [11] Fig. 48. Due to the long investigation time, it was necessary to shorten the duration to reduce the computational load. A time frame, only 30 seconds, was selected during which the wind speed reaches its peak for the transient analysis.

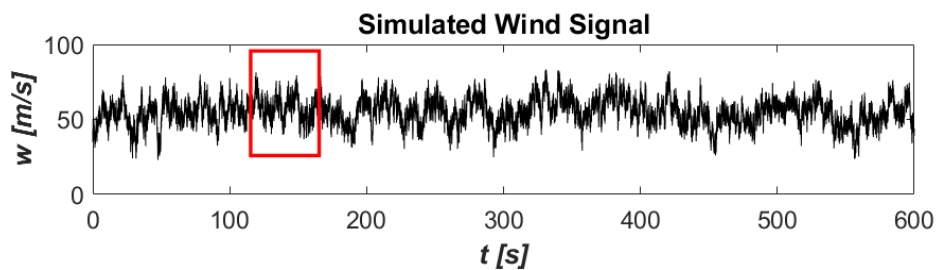


Figure 48: Simulated wind signal

Once the wind speed was determined, the pressure P exerted Fig. 49 by the wind was calculated using Eq. (32)

$$P = \frac{1}{2} \rho v^2 \quad (32)$$

Where:

P is the applied pressure

ρ is the density of air equal to 1.225 kg/m^3

v is the wind velocity

The application of this pressure was assumed, for the purpose of the simulation, to be present on a single facade characterized by $X=0$.

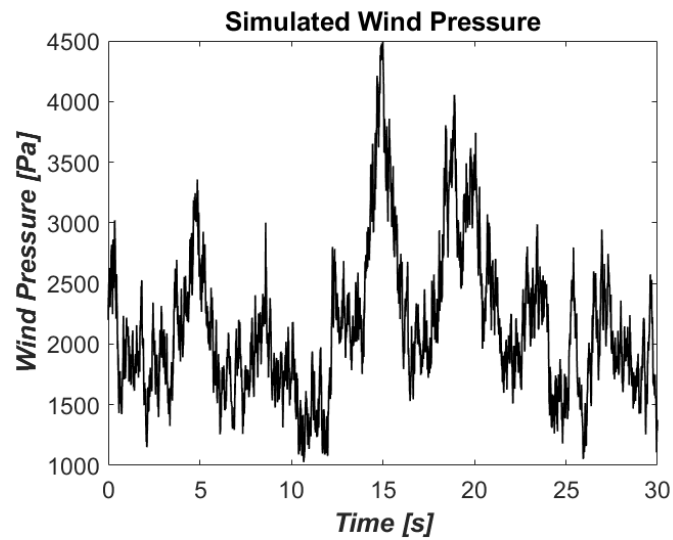


Figure 49: Applied pressure due to wind

4.2.1 Reinforced concrete structure

For these cases, two main types of structural elements are established: one for infill walls and floors (shell elements, which represent flat surfaces such as walls and floors), and the other for columns and beams (beam elements, which represent linear structures such as columns and beams).

These elements are characterized by different materials that have different values. The adopted characteristics are summarized in the tables below.

<i>Infill wall (hollow concrete blocks)</i>		
E	1.2x10 ⁹	N/m ²
v	0.25	
ρ	1200	Kg/m ³

Table 2: Material parameters of infill wall

<i>Reinforced concrete</i>		
E	3x10 ¹⁰	N/m ²
v	0.20	
ρ	2500	Kg/m ³

Table 3: Material parameters of reinforced concrete

Each material is associated with a structural section. The infill walls are treated as shell sections with a thickness of 0.3 meters, while the slabs are defined with a greater thickness of 0.3 meters. The columns and beams are modelled as beam elements, with quadratic section measuring 0.3x0.3 meters.

4.2.2 Masonry structure

Two main types of structural elements are established: one for load bearing walls and slabs (shell elements, which represent flat surfaces), and the other for curb (beam elements, which represent linear structures).

For each type of material, specific physical parameters are defined.

<i>Load bearing walls (solid bricks and mortar)</i>		
E	1.8x10 ⁹	N/m ²
v	0.25	
ρ	1300	Kg/m ³

Table 4: Material parameters of load bearing walls

<i>Reinforced concrete</i>		
E	3x10 ¹⁰	N/m ²
v	0.20	
ρ	2500	Kg/m ³

Table 5: Material parameters of reinforced concrete

Each material is associated with a structural section. The load bearing walls are treated as shell sections with a thickness of 0.4 meters, while the slabs are defined with a greater thickness of 0.3 meters. Curb elements are modelled as beam elements, with rectangular section measuring 0.4x0.3 meters.

4.2.3 Result of Reinforced concrete structures

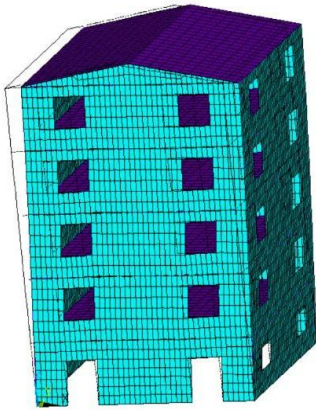
Modal analysis

Subsequently, the three modal deformations of the reinforced concrete structures corresponding to translation along the x-axis, along the y-axis, and rotation about the z-axis will be presented.

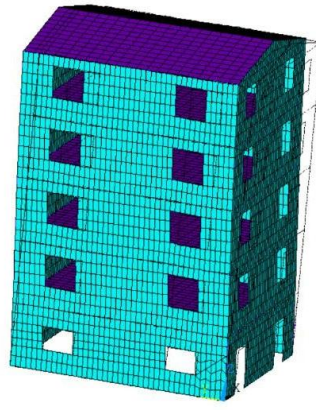
It is reminded that, in order to better visualize the deformations, the assumption of not real scale was used

First square plan – Reinforced concrete

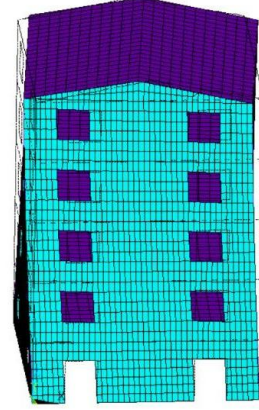
$$f_1 = 2.19 \text{ Hz}$$



$$f_2 = 2.21 \text{ Hz}$$

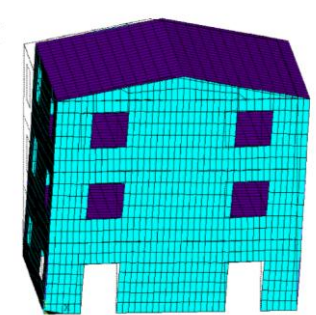


$$f_3 = 3.65 \text{ Hz}$$

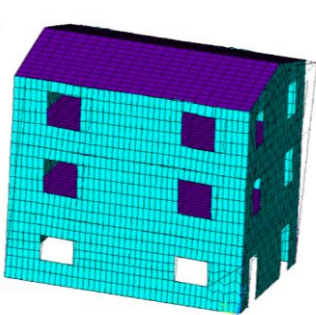


Second square plan – Reinforced concrete

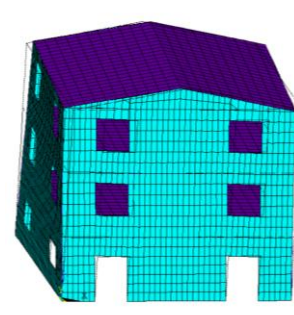
$$f_1 = 3.42 \text{ Hz}$$



$$f_2 = 3.44 \text{ Hz}$$

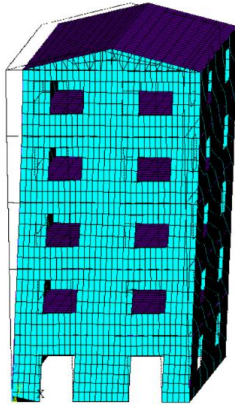


$$f_3 = 5.68 \text{ Hz}$$

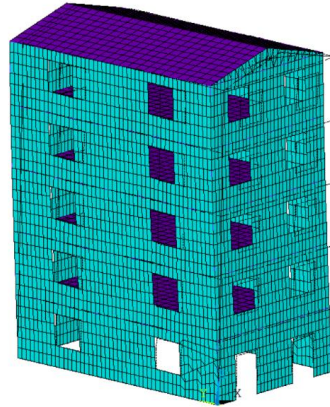


Third rectangular plan – Reinforced concrete

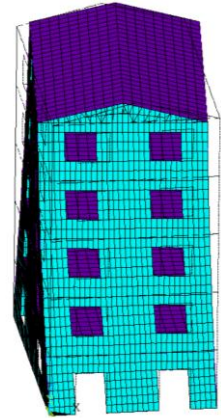
$f_1 = 1.85 \text{ Hz}$



$f_2 = 2.55 \text{ Hz}$

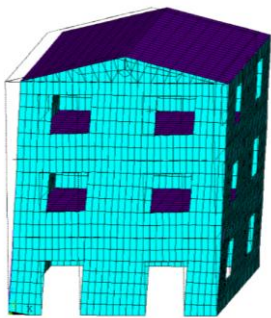


$f_3 = 3.44 \text{ Hz}$

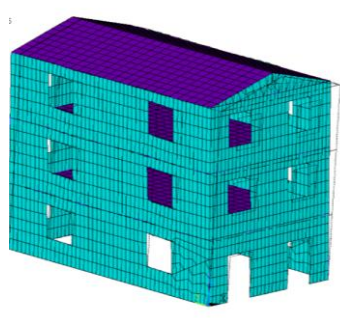


Fourth rectangular plan – Reinforced concrete

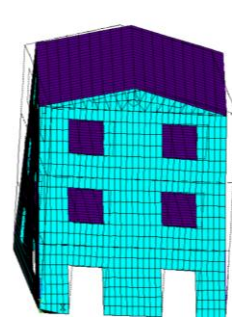
$f_1 = 2.89 \text{ Hz}$



$f_2 = 3.98 \text{ Hz}$



$f_3 = 5.35 \text{ Hz}$

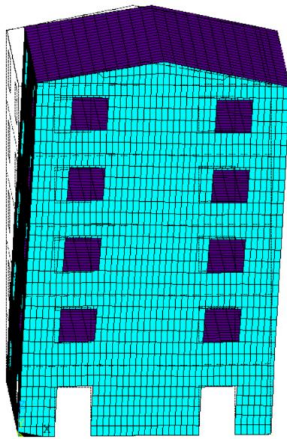


4.2.4 Result of Masonry structures

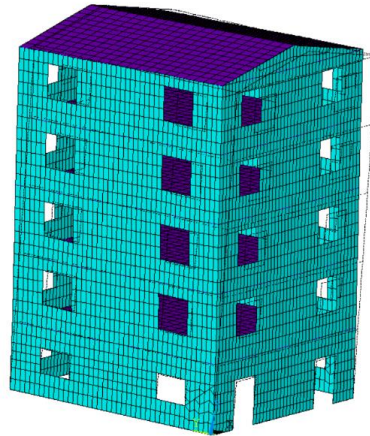
Modal analysis

First square plan – Masonry

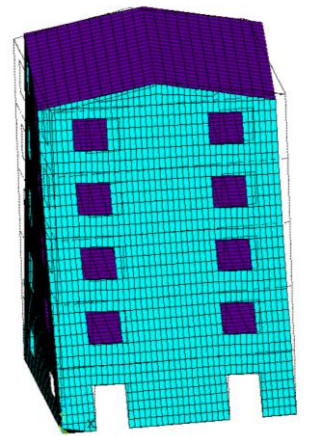
$$f_1 = 2.88 \text{ Hz}$$



$$f_2 = 2.90 \text{ Hz}$$

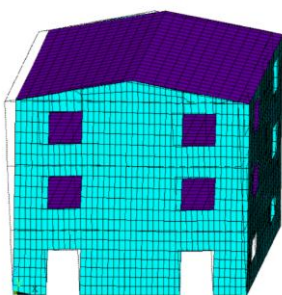


$$f_3 = 5.42 \text{ Hz}$$

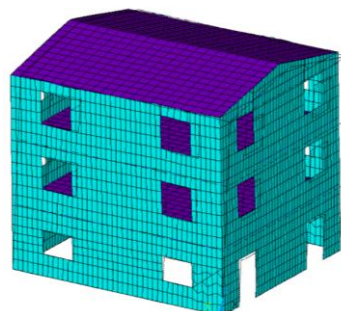


Second square plan – Masonry

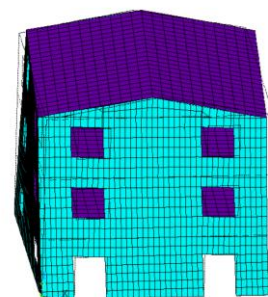
$$f_1 = 4.90 \text{ Hz}$$



$$f_2 = 4.93 \text{ Hz}$$

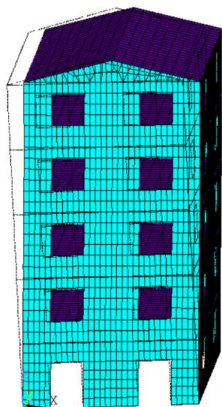


$$f_3 = 8.53 \text{ Hz}$$

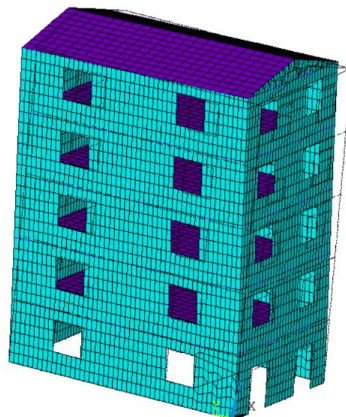


Third rectangular plan – Masonry

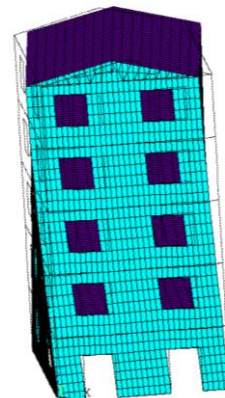
$f_1 = 2.39 \text{ Hz}$



$f_2 = 3.25 \text{ Hz}$

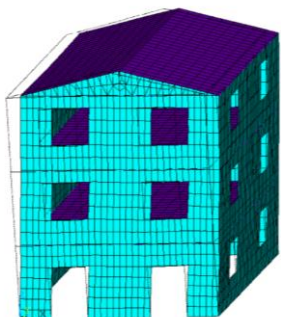


$f_3 = 5.05 \text{ Hz}$

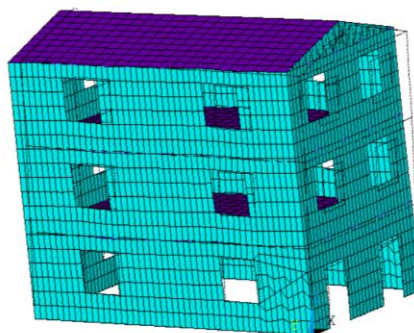


Fourth rectangular plan – Masonry

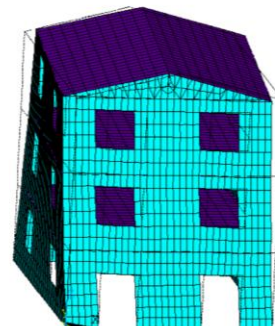
$f_1 = 4.04 \text{ Hz}$



$f_2 = 5.57 \text{ Hz}$



$f_3 = 7.88 \text{ Hz}$



5.0 Application of coupled system

In this chapter of the thesis, the elements studied so far the metapanel and the buildings will be analysed together. Two solutions will be presented:

1. The meta-panels will be applied only to the top floor of each building.
2. The meta-panels will be applied to both the top and penultimate floors of each building.

The structure will be analysed through both a modal analysis and a transient analysis, as previously described. The transient analysis will involve the application of two types of loads: the Aquila earthquake *Fig 47* and the wind load *Fig. 49*.

The displacement results obtained for reinforced concrete buildings section 4.2.3 and masonry buildings section 4.2.4 through transient analysis will be directly compared to the first and second solution previously introduced.

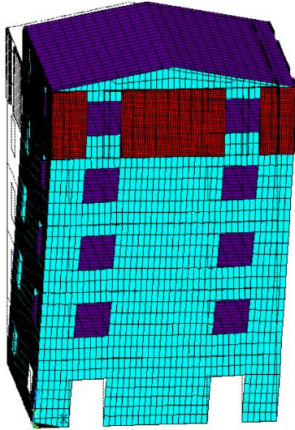
5.1 Reinforced concrete structures

5.1.1 First proposed solution

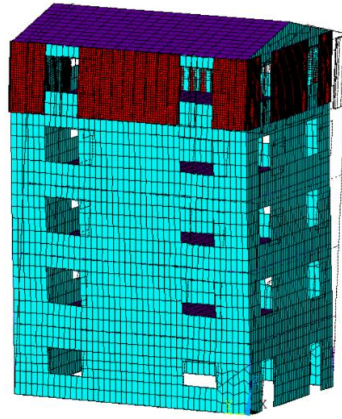
Modal analysis

First square plan – Reinforced concrete

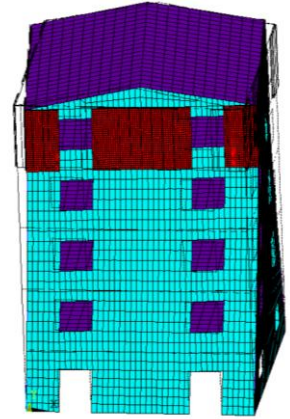
$$f_1 = 2.20 \text{ Hz}$$



$$f_2 = 2.22 \text{ Hz}$$

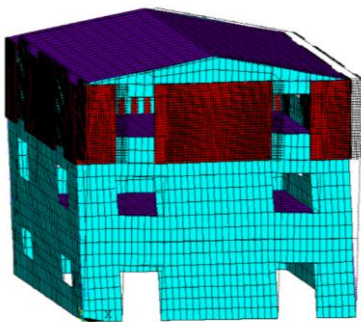


$$f_3 = 3.62 \text{ Hz}$$

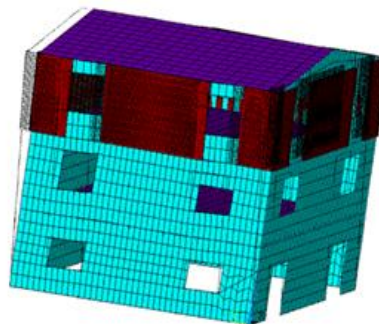


Second square plan – Reinforced concrete

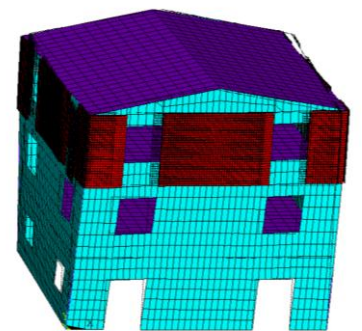
$$f_1 = 3.57 \text{ Hz}$$



$$f_2 = 3.65 \text{ Hz}$$

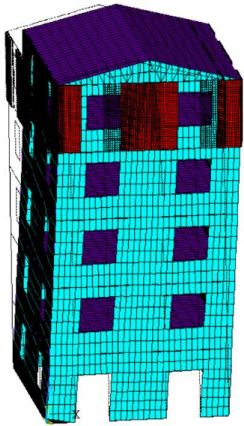


$$f_3 = 5.84 \text{ Hz}$$

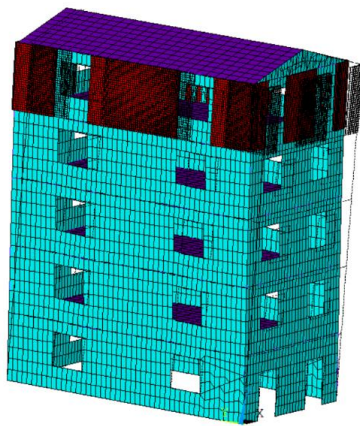


Third rectangular plan – Reinforced concrete

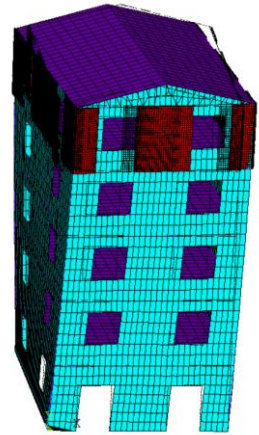
$f_1 = 1.85 \text{ Hz}$



$f_2 = 2.56 \text{ Hz}$

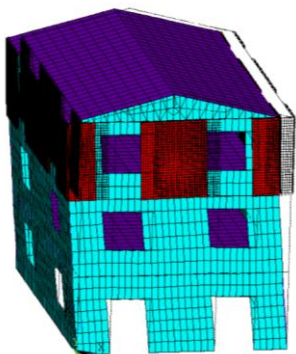


$f_3 = 3.44 \text{ Hz}$

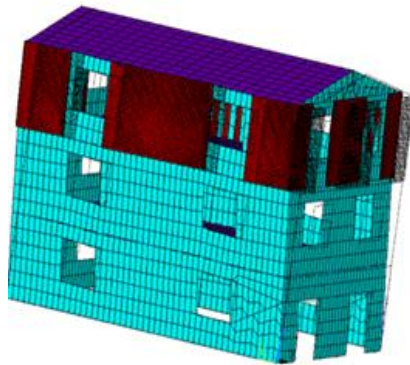


Fourth rectangular plan – Reinforced concrete

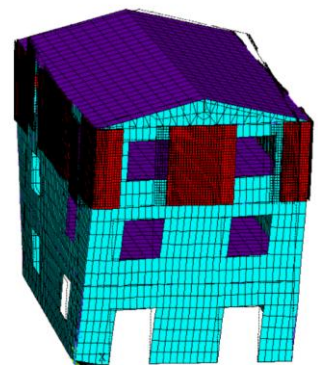
$f_1 = 2.98 \text{ Hz}$



$f_2 = 4.15 \text{ Hz}$



$f_3 = 5.47 \text{ Hz}$



Time-history dynamic analysis under seismic excitation

This section will present the displacement solutions for reinforced concrete buildings, with metapanel applied to the façade of only on the top floor as illustrated in section 5.1.1.

For each analysed reinforced structure, two types of input will be applied: the L'Aquila earthquake *Fig. 47* and the wind load *Fig. 49* as illustrated in 4.2.

Seismic Input Application

According to EC8 (Eurocode 8), seismic forces must be applied in two orthogonal directions. In general, 100% of the earthquake intensity is applied along the primary structural direction (typically aligned with the X or Y axis), while 30% of the intensity is applied along the orthogonal direction.

This distribution accounts for potential seismic components acting perpendicularly to the main structural response. Therefore, in this study, the earthquake load is applied as follows:

- **100% along the primary direction (X)**
- **30% along the orthogonal direction (Y)**

Wind Load Application

For the wind load, the force is applied entirely (100%) along the X direction. However, this applies only to buildings with a greater height (16 meters), as they experience more significant displacements over their service life.

Results Analysis

The extracted results focus on the centroidal point located at the topmost walkable floor, at a height of:

- **Z = 15 m** for taller structures
- **Z = 9 m** for shorter structures

These results will be presented in the section 5.1.1 and 5.1.2

As we can observe in the figures below, *Fig. 50,51,52* and *53*, two types of functions have been plotted, corresponding to the displacement at the centroid of the topmost accessible floor of the considered structure. The red curve represents the deformation response in the "controlled" case, where metapanel are present only on the top floor, as shown in section *5.1.1*, while the black curve represents the deformation response in the "uncontrolled" case. For each case, we compared and estimated the peak displacement reduction, also creating an auxiliary image to ensure better visualization. Furthermore, the displacement recorded along the X direction is larger than the displacement in the Y direction, this is due to the assumptions made according to EC8.

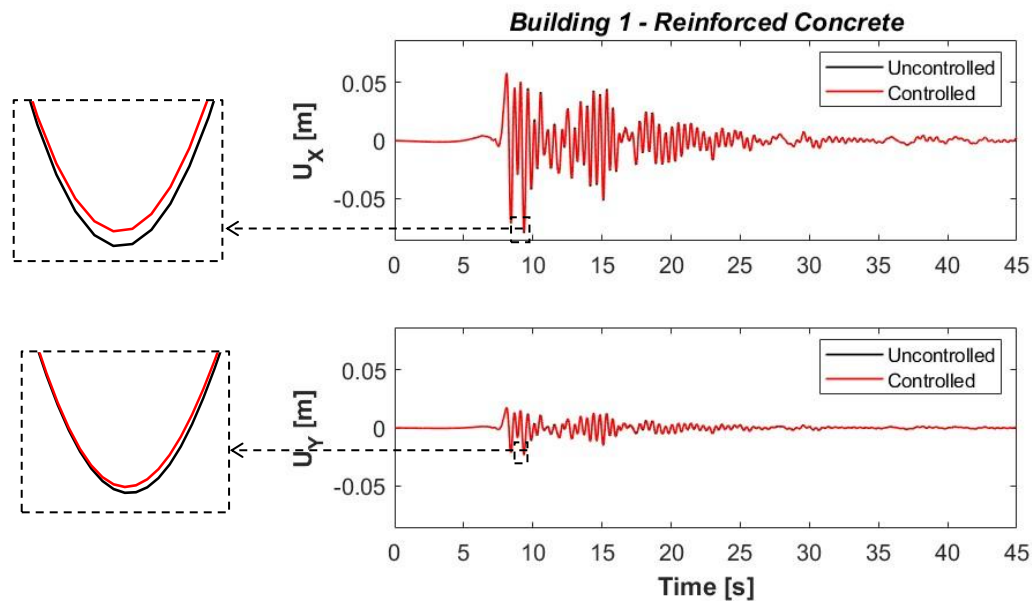


Figure 50: Earthquake displacement with one layer of metapanel (1RC)

In the case of *Fig. 50*, which refers to the reinforced concrete structure with a square floor plan and a node height of $Z = 15$ m, a zoom-in was made at the peak point that occurred at the peak displacement.

The seismic improvement and the relative reduction in the peak corresponding to the displacement along X is **1.43 %** and along Y corresponds to **2.73 %**, these values will be appropriately collected in Table 6.

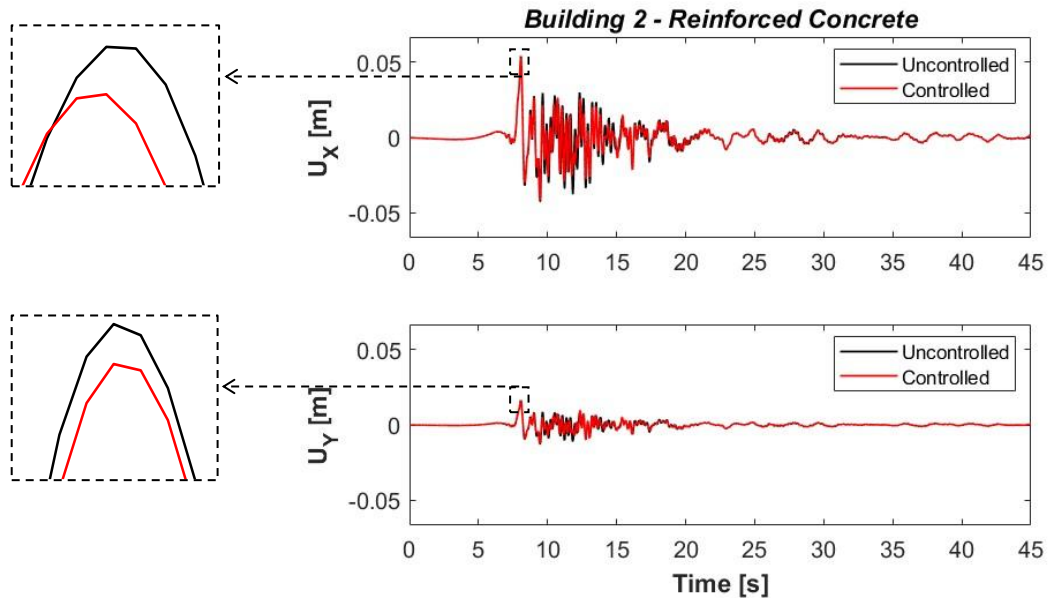


Figure 51: Earthquake displacement with one layer of metapanel (2RC)

In the case of *Fig. 51*, which refers to the reinforced concrete structure with a square floor plan and a node height of $Z = 9$ m, a zoom-in was made at the peak point that occurred at the peak displacement.

The seismic improvement and the relative reduction in the peak corresponding to the displacement along X is **1.51 %** and along Y corresponds to **2.63 %**, these values will be appropriately collected in Table 6.

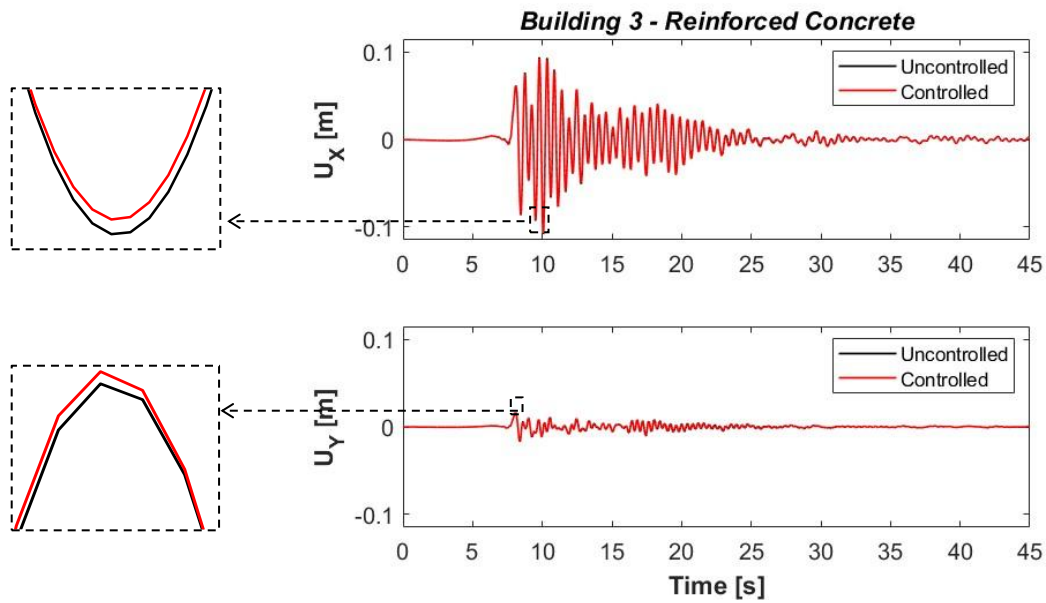


Figure 52: Earthquake displacement with one layer of metapanel (3RC)

In the case of Fig. 52, which refers to the reinforced concrete structure with a rectangular floor plan and a node height of $Z = 15$ m, a zoom-in was made at the peak point that occurred at the peak displacement.

The seismic improvement and the relative reduction in the peak corresponding to the displacement along X is **1.37 %** and along Y corresponds to **1.62 %**, these values will be appropriately collected in Table 6.

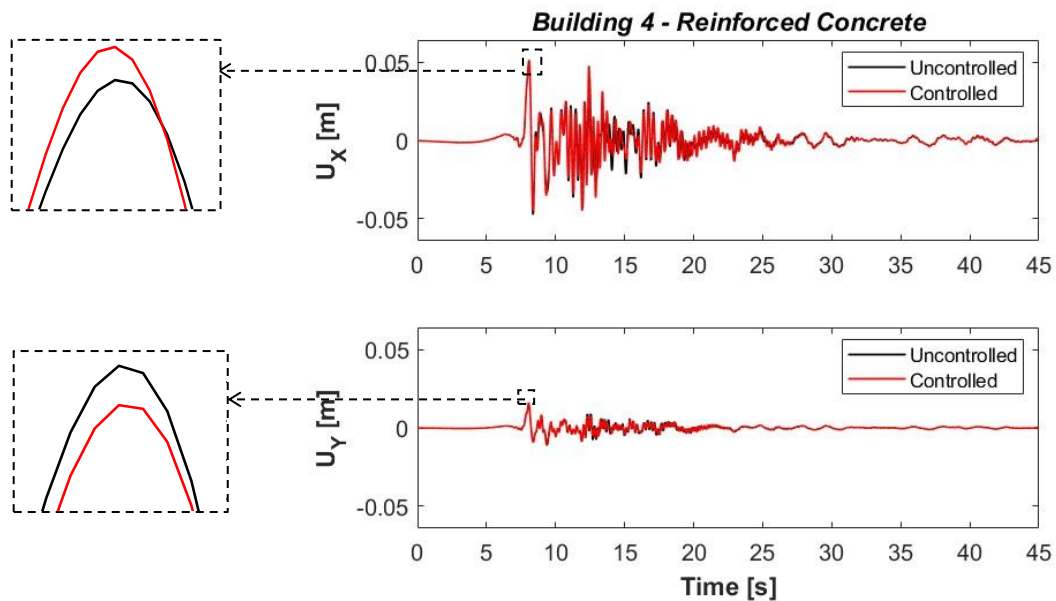


Figure 53: Earthquake displacement with one layer of metapanel (4RC)

In the case of *Fig. 53*, which refers to the reinforced concrete structure with a rectangular floor plan and a node height of $Z = 9$ m, a zoom-in was made at the peak point that occurred at the peak displacement.

The seismic improvement and the relative reduction in the peak corresponding only to the displacement along X is **0.99 %**. In this case, for the displacements referred to the Y direction, no seismic improvement was found, corresponding to **-1.83 %**, these values will be appropriately collected in Table 6.

One Layer of metapanel				
	<i>PLANE</i>	<i>FLOORS</i>	Δu_x [%]	Δu_y [%]
Reinforced Concrete	<i>square</i>	3	1.51	2.63
		5	1.43	2.73
	<i>rectangular</i>	3	0.99	-1.83
		5	1.37	1.62

Table 6: Collection of seismic improvement for an earthquake with a single layer of metapanel for reinforced concrete structure.

These results were achievable due to the presence of the metapanel, which acted as a passive control system through the mass applied above them. The earthquake input generated deformation in the panel, and through the oscillation of the mass and the bistable behavior, it was possible to achieve seismic improvement for almost all of the buildings.

Time-history dynamic analysis under wind excitation

This section presents *Fig. 54,55* that illustrate how the simulated application of wind acts on the reinforced concrete structure in the absence of metapanel compared to their presence. This is done to understand the impact of metapanel on the building response in case of operating conditions. The figures show two types of functions: one in red, referring to the "controlled" case, which consists of the structure system with metapanel applied only on the top floor. The black function refers to the "uncontrolled" case, consisting of the structure system alone. Both functions describe the displacement of the same centroid point located on the topmost floor slab. As previously stated, this simulation was carried out considering that the wind was applied to the entire surface corresponding to the X direction.

The purpose of this analysis was to evaluate whether the presence of metapanel applied to buildings with five above-ground floors could ensure, in addition to seismic improvement, an enhancement of comfort throughout the building's service life. The values will be reported in Table 7.

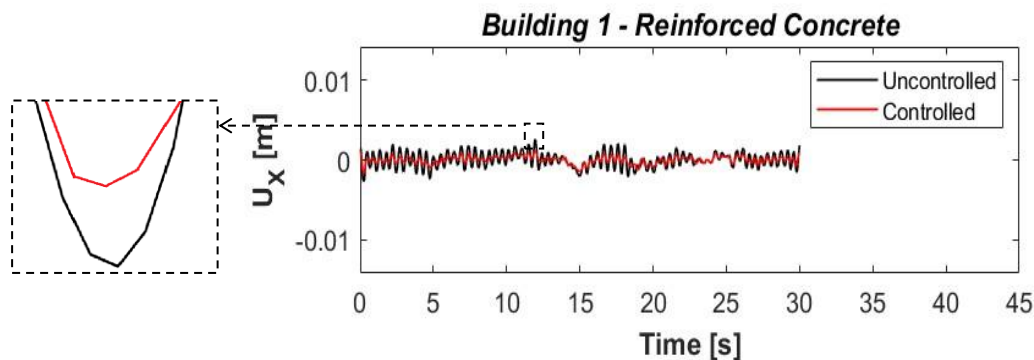


Figure 54: Wind displacement with one layer of metapanel (IRC)

In the case of *Fig 54.* , which refers to the reinforced concrete structure with a square floor plan and a node height of $Z = 15$ m, a zoom-in was made at the peak point that occurred at the peak displacement.

The dissipative capacity and the relative reduction in the peak corresponding to the displacement along X is **38.05 %**. For these simulations, no study was presented

regarding the displacement along the Y direction for the applied load assumptions. The value will be appropriately collected in Table 7.

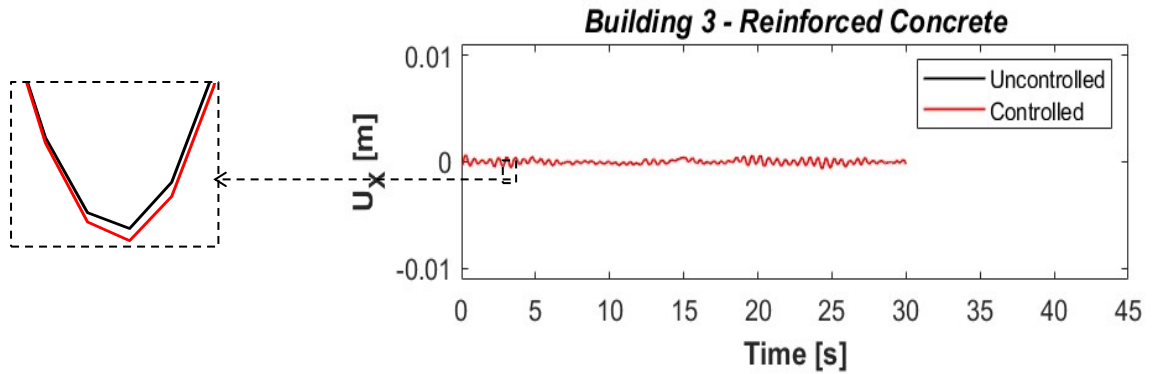


Figure 55: Wind displacement with one layer of metapanel (3RC)

In the case of Fig. 55, which refers to the reinforced concrete structure with a rectangular floor plan and a node height of $Z = 15$ m, a zoom-in was made at the peak point that occurred at the peak displacement.

The dissipative capacity and the relative reduction in the peak corresponding to the displacement along X is **1.26 %**. For these simulations, no study was presented regarding the displacement along the Y direction for the applied load assumptions. The value will be appropriately collected in Table 7.

One Layer of metapanel				
	<i>PLANE</i>	<i>FLOORS</i>	Δu_x [%]	Δu_y [%]
Reinforced Concrete	<i>square</i>	-	-	-
		5	38.05	-
	<i>rectangular</i>	-	-	-
		5	1.26	-

Table 7: Collection of wind-induced dissipative capacity for a single layer of metapanel for reinforced concrete structure.

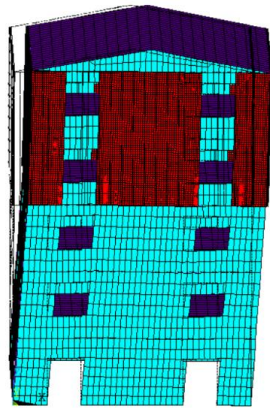
The results presented in Table 19 show that the application of simulated wind to reinforced concrete structures taller than 15 meters has led to an improvement in comfort. This effect is particularly notable in the square-plan building, which achieves a dissipation of **38.05%**.

5.1.2 Second proposed solution

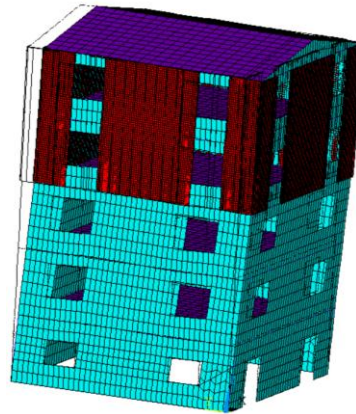
Modal analysis

First square plan – Reinforced concrete

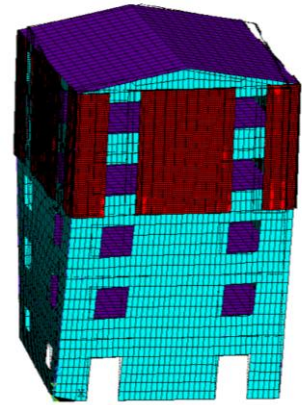
$$f_1 = 2.27 \text{ Hz}$$



$$f_2 = 2.29 \text{ Hz}$$

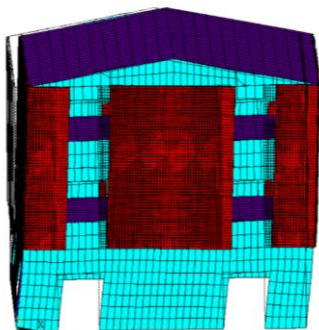


$$f_3 = 3.74 \text{ Hz}$$

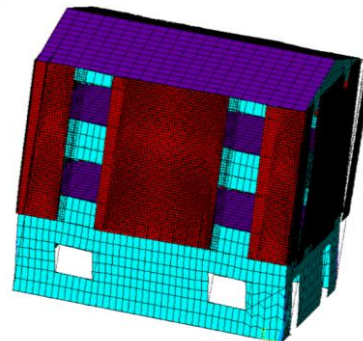


Second square plan – Reinforced concrete

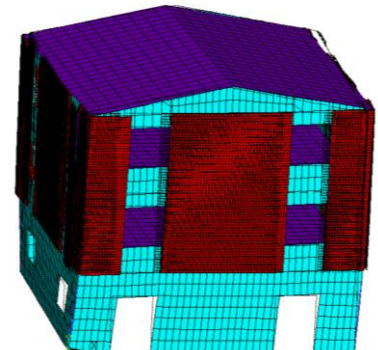
$$f_1 = 3.96 \text{ Hz}$$



$$f_2 = 4.06 \text{ Hz}$$

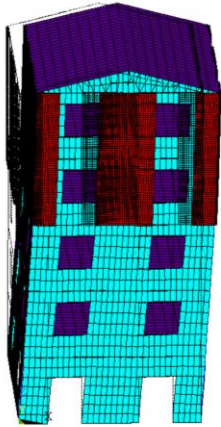


$$f_3 = 6.51 \text{ Hz}$$

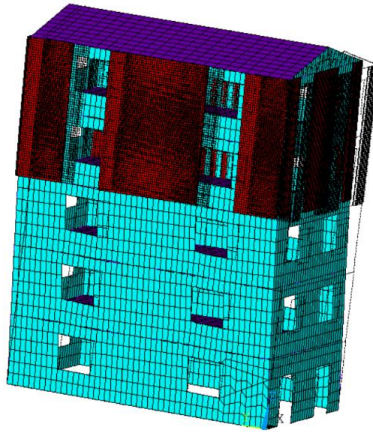


Third rectangular plan – Reinforced concrete

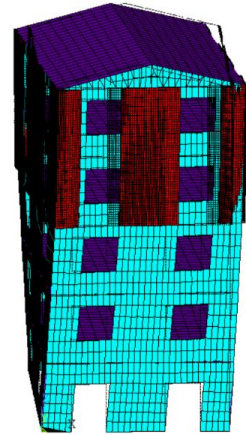
$f_1 = 1.89 \text{ Hz}$



$f_2 = 2.63 \text{ Hz}$

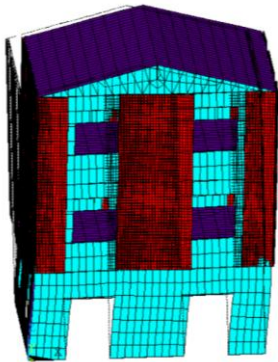


$f_3 = 3.51 \text{ Hz}$

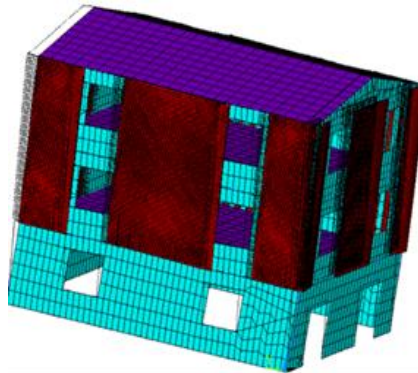


Fourth rectangular plan – Reinforced concrete

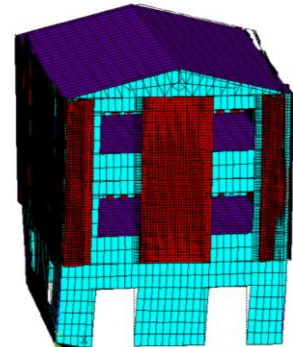
$f_1 = 3.21 \text{ Hz}$



$f_2 = 4.57 \text{ Hz}$



$f_3 = 5.96 \text{ Hz}$



Time-history dynamic analysis under seismic excitation

This section will present the displacement solutions for reinforced concrete buildings, this time with metapanel applied to the façade of both the top and second-to-last floors as illustrated in section 5.1.2.

As can be observed in *Fig. 56,57,58* and *59*, two types of functions have been plotted, corresponding to the displacement at the centroid of the topmost accessible floor of the considered structure. The red curve represents the deformation response in the "controlled" case, while the black curve represents the deformation response in the "uncontrolled" case. For each case, we compared and estimated the peak displacement reduction, also creating an auxiliary image to ensure better visualization. Furthermore, the displacement recorded along the X direction is larger than the displacement in the Y direction, this is due to the assumptions made according to EC8.

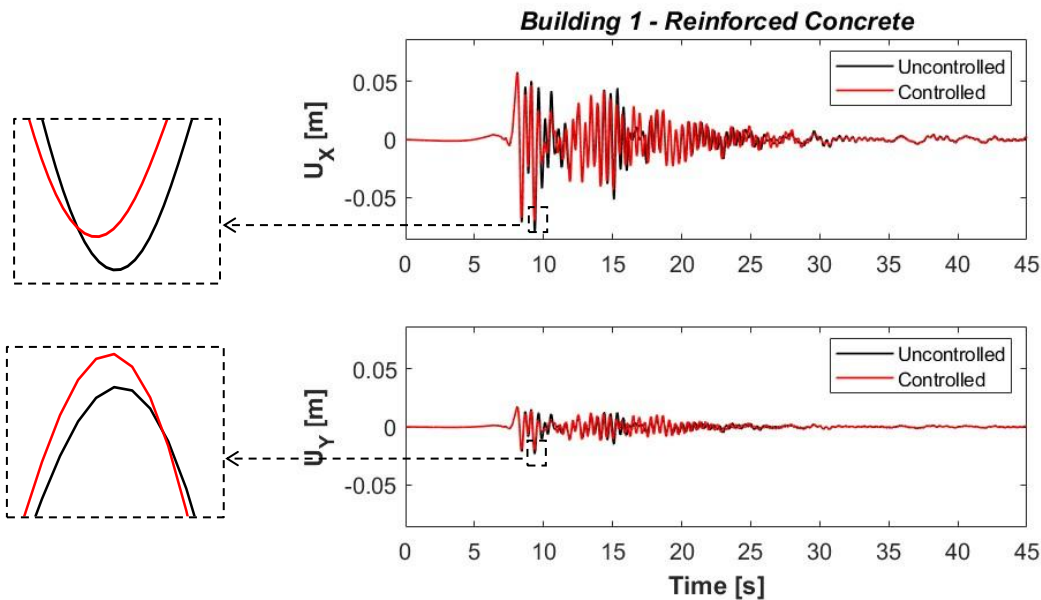


Figure 56: Earthquake displacement with two layers of metapanel (1RC)

The presence of a double row of metapanel installed on the building has led to significant increases in seismic dissipation. As can be observed, in *Fig. 56*, which refers to the reinforced concrete structure with a square floor plan and a node height of $Z=15$ m, a zoom-in was made at the peak point that occurred at the peak displacement.

The seismic improvement and the relative reduction in the peak corresponding to the displacement along X is **12.10%** and along Y corresponds to **14.28 %**, these values will be appropriately collected in Table 8.

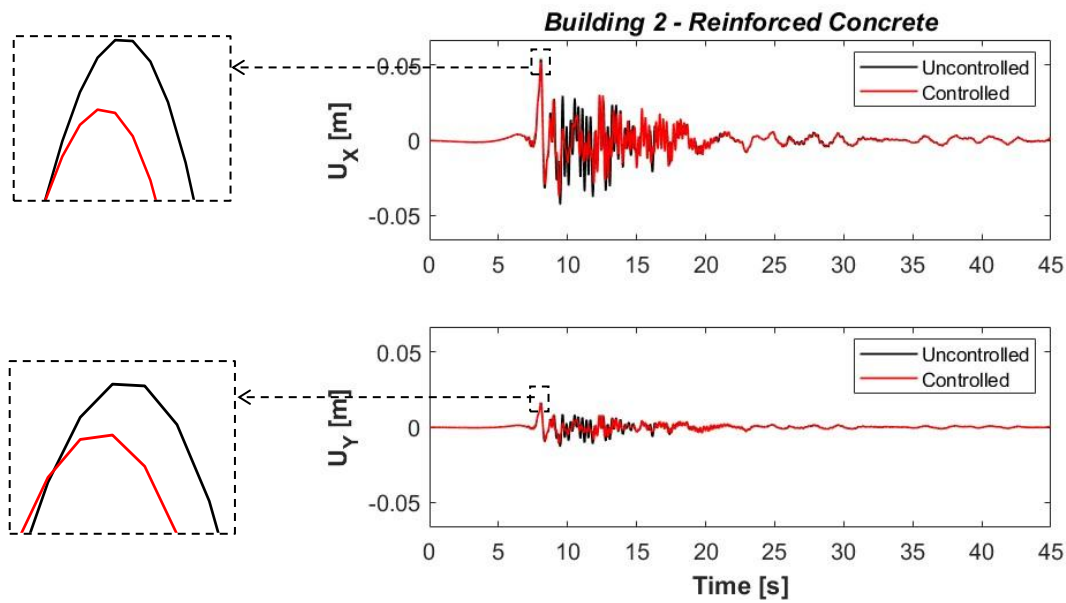


Figure 57: Earthquake displacement with two layers of metapanel (2RC)

In the case of *Fig. 57*, which refers to the reinforced concrete structure with a square floor plan and a node height of $Z = 9$ m, a zoom-in was made at the peak point that occurred at the peak displacement.

The seismic improvement and the relative reduction in the peak corresponding only to the displacement along X is **3.88 %**. In this case, for the displacements referred to the Y direction, no seismic improvement was found, corresponding to **2.67 %**, these values will be appropriately collected in Table 8.

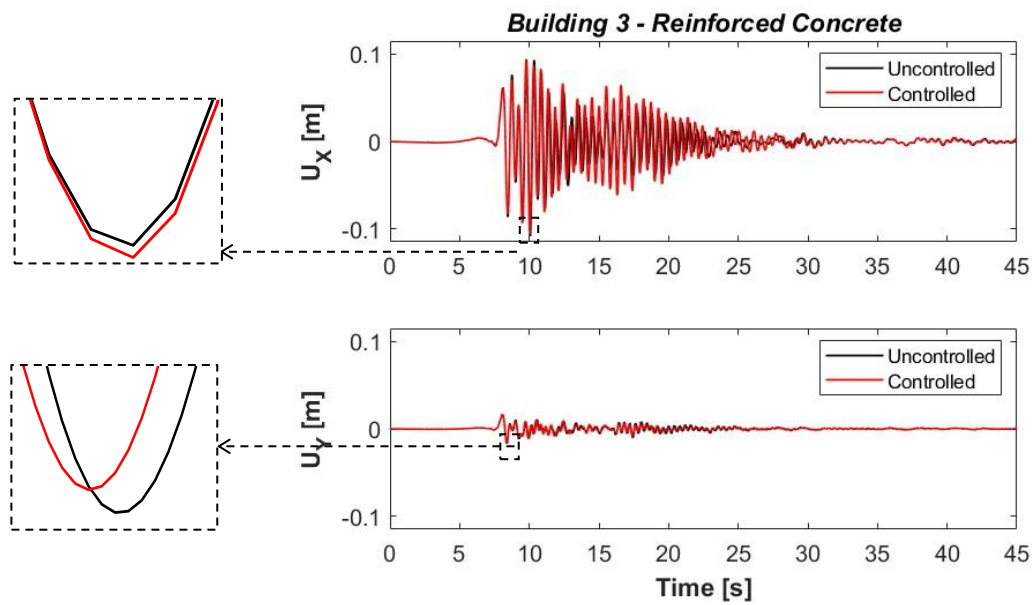


Figure 58: Earthquake displacement with two layers of metapanel (3RC)

In the case of *Fig. 58*, which refers to the reinforced concrete structure with a rectangular floor plan and a node height of $Z = 15$ m, a zoom-in was made at the peak point that occurred at the peak displacement.

The seismic improvement and the relative reduction in the peak corresponding only to the displacement along X is **2.80 %**. In this case, for the displacements referred to the Y direction, no seismic improvement was found, corresponding to **4.84%**, these values will be appropriately collected in Table 8.

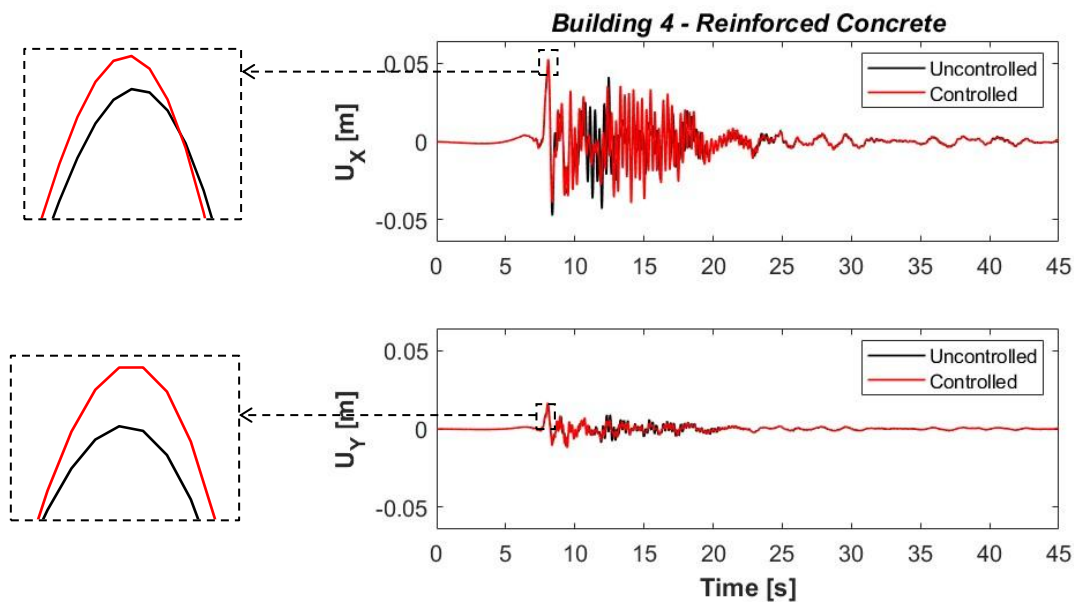


Figure 59: Earthquake displacement with two layers of metapanel (4RC)

In the case of *Fig. 59*, which refers to the reinforced concrete structure with a rectangular floor plan and a node height of $Z = 9$ m, a zoom-in was made at the peak point that occurred at the peak displacement.

For this type of structure, the application of metapanel did not result in any seismic improvement. The corresponding value along X is **-2.34 %**. In this case, for the displacements referred to the Y direction, also no seismic improvement was found, corresponding to **-5.40%**, these values will be appropriately collected in Table 8.

Two Layer of metapanel					
		<i>PLANE</i>	<i>FLOORS</i>	ΔU_x [%]	ΔU_y [%]
Reinforced Concrete	<i>square</i>		3	3.88	2.67
			5	12.10	14.28
	<i>rectangular</i>		3	-2.34	-5.40
			5	2.80	4.84

Table 8 Collection of seismic improvement for an earthquake with a double layer of metapanel for reinforced concrete structure

The results shown in Table 8 demonstrate how the use of a greater mass applied to the surface of reinforced concrete structure, significantly contributes to seismic improvement. The increase in mass generated a rise in damping, amplifying the passive absorption of the metapanel. Through its bistable properties, the increase in absorbed energy was enhanced, leading to much higher values in most cases, even exceeding **12%**.

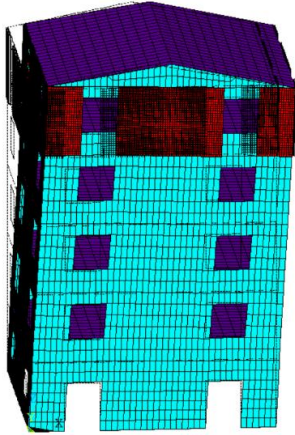
5.2 Masonry structures

5.2.1 First proposed solution

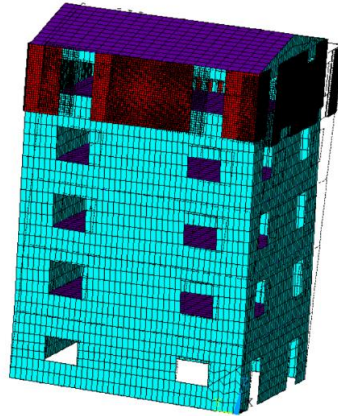
Modal analysis

First square plan – Masonry

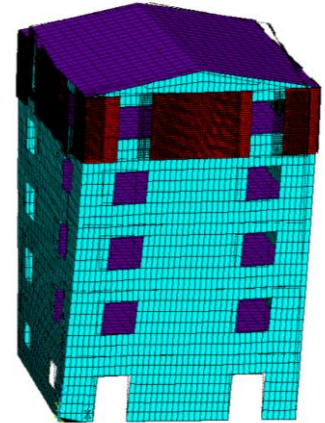
$$f_1 = 2.88 \text{ Hz}$$



$$f_2 = 2.90 \text{ Hz}$$

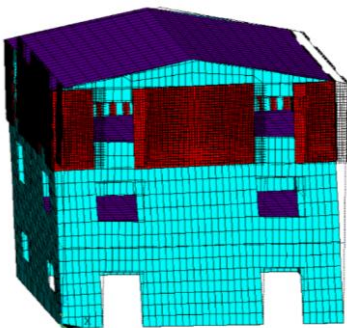


$$f_3 = 5.40 \text{ Hz}$$

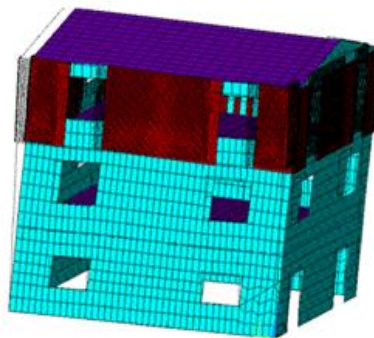


Second square plan – Masonry

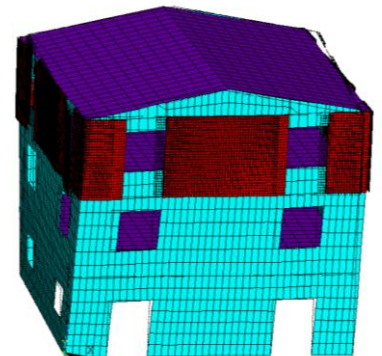
$$f_1 = 4.96 \text{ Hz}$$



$$f_2 = 5.02 \text{ Hz}$$

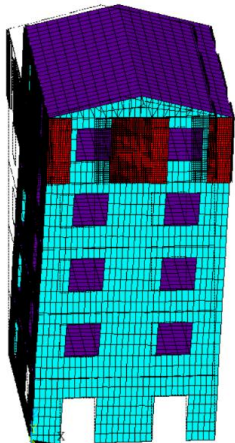


$$f_3 = 8.61 \text{ Hz}$$

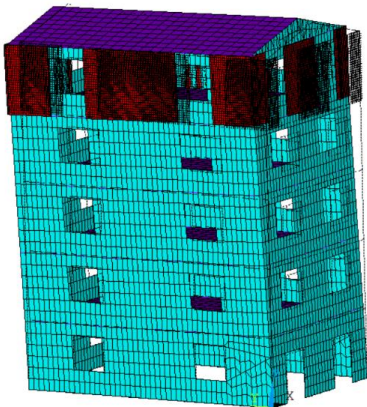


Third rectangular plan – Masonry

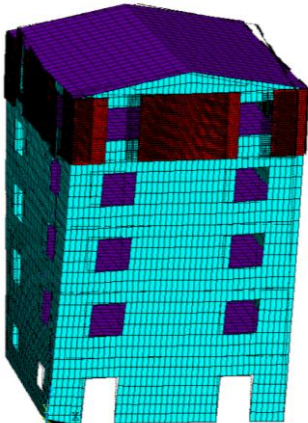
$f_1 = 2.39 \text{ Hz}$



$f_2 = 3.25 \text{ Hz}$

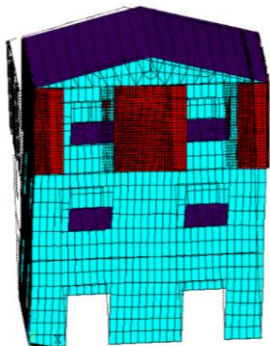


$f_3 = 5.03 \text{ Hz}$

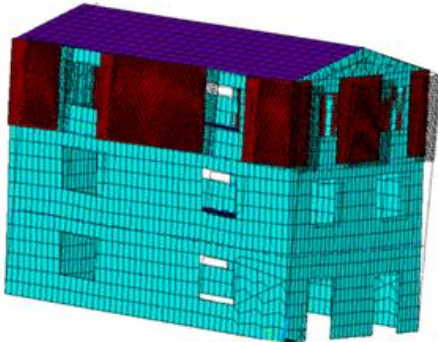


Fourth rectangular plan – Masonry

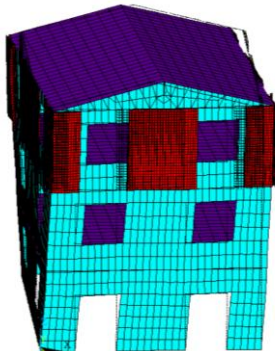
$f_1 = 4.07 \text{ Hz}$



$f_2 = 5.63 \text{ Hz}$



$f_3 = 7.91 \text{ Hz}$



Time-history dynamic analysis under seismic excitation

In this section, as previously described for the reinforced concrete structures, the structural responses of masonry buildings will be analyzed. In *Fig. 60,61,62* and *63*, two types of functions have been plotted, corresponding to the displacement at the centroid of the topmost accessible floor of the considered structure. The red curve represents the deformation response in the "controlled" case, where metapanel are present only on the top floor, as shown in section 5.2.1, while the black curve represents the deformation response in the "uncontrolled" case. For each case, we compared and estimated the peak displacement reduction, also creating an auxiliary image to ensure better visualization. Furthermore, the displacement recorded along the X direction is larger than the displacement in the Y direction, this is due to the assumptions made according to EC8

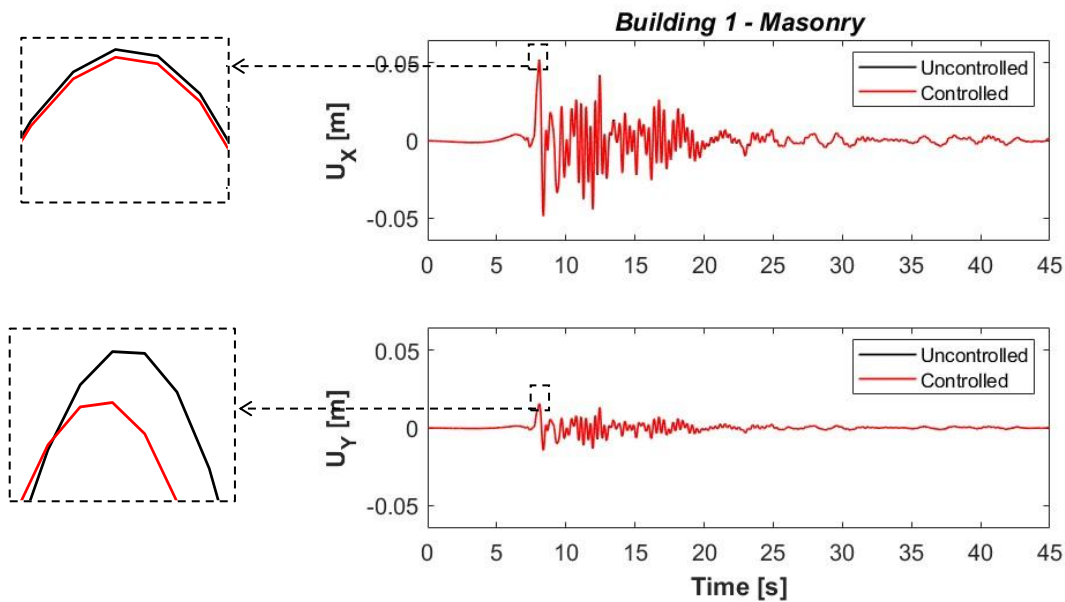


Figure 60: Earthquake displacement with one layer of metapanel (1M)

In the case of *Fig. 60*, which refers to the masonry structure with a square floor plan and a node height of $Z = 15$ m, a zoom-in was made at the peak point that occurred at the peak displacement.

The seismic improvement and the relative reduction in the peak corresponding to the displacement along X is **0.76 %** and along Y corresponds to **1.29 %**, these values will be appropriately collected in Table 9.

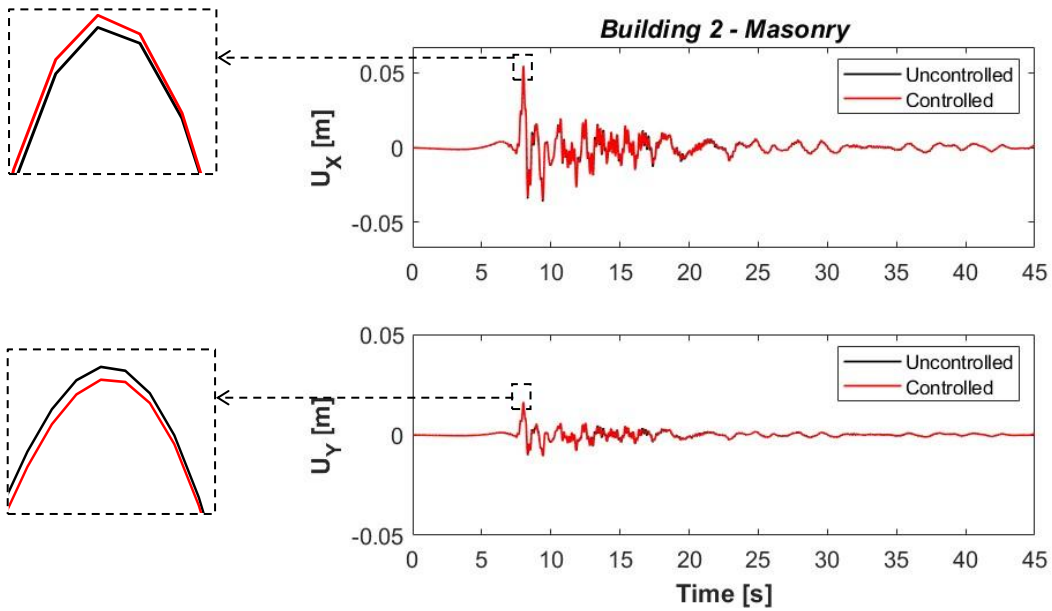


Figure 61: Earthquake displacement with one layer of metapanel (2M)

In the case of Fig. 61, which refers to the masonry structure with a square floor plan and a node height of $Z = 9$ m, a zoom-in was made at the peak point that occurred at the peak displacement.

The seismic improvement and the relative reduction in the peak corresponding to the displacement along X is **-0.18 %** and along Y corresponds to **0.23 %**, these values will be appropriately collected in Table 9.

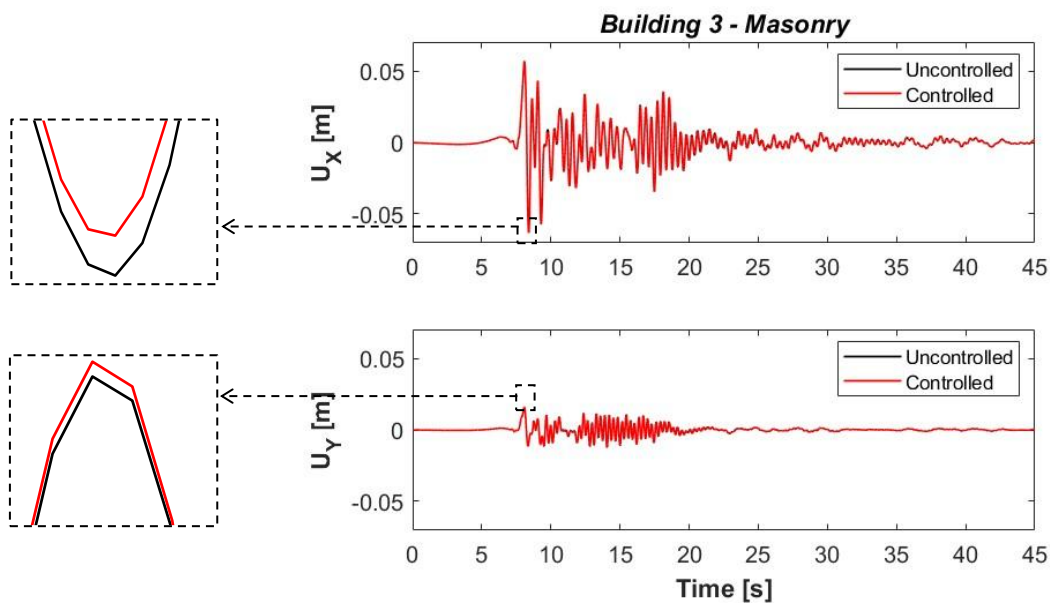


Figure 62: Earthquake displacement with one layer of metapanel (3M)

In the case of *Fig. 62*, which refers to the masonry structure with a rectangular floor plan and a node height of $Z = 15$ m, a zoom-in was made at the peak point that occurred at the peak displacement.

The seismic improvement and the relative reduction in the peak corresponding only to the displacement along Y is **0.37 %**. In this case, for the displacements referred to the X direction, no seismic improvement was found, corresponding to **-0.24 %**, these values will be appropriately collected in Table 9.

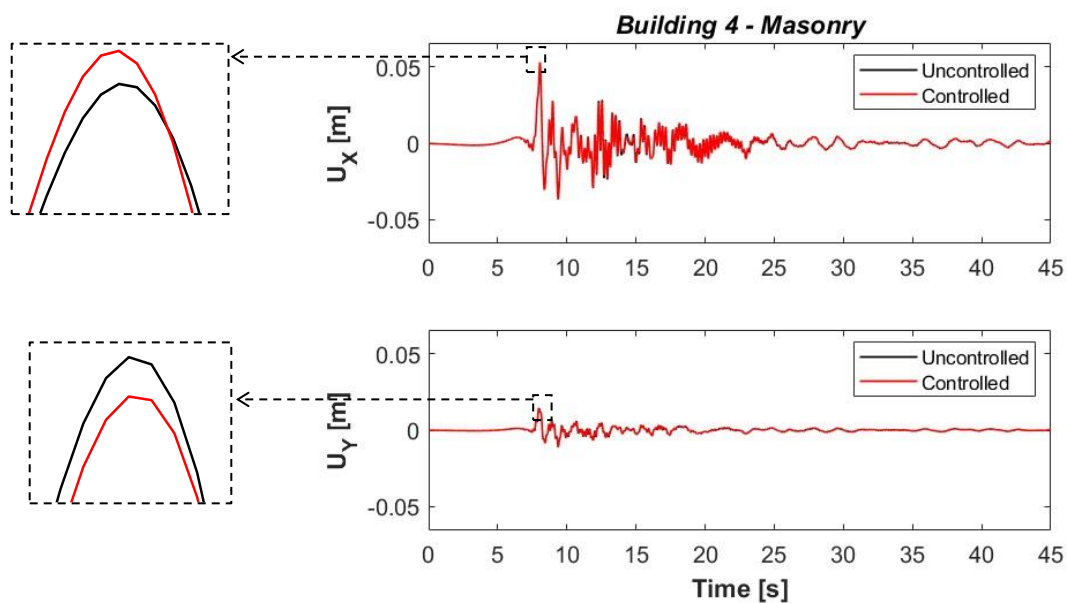


Figure 63: Earthquake displacement with one layer of metapanel (4M)

In the case of *Fig. 63*, which refers to the masonry structure with a rectangular floor plan and a node height of $Z = 9$ m, a zoom-in was made at the peak point that occurred at the peak displacement.

The seismic improvement and the relative reduction in the peak corresponding only to the displacement along Y is **1.85 %**. In this case, for the displacements referred to the X direction, no seismic improvement was found, corresponding to **-0.18 %**, these values will be appropriately collected in Table 9.

One Layer of metapanel				
	<i>PLANE</i>	<i>FLOORS</i>	ΔU_x [%]	ΔU_y [%]
Masonry	<i>square</i>	3	0.76	1.29
		5	0.18	0.23
	<i>rectangular</i>	3	-0.18	1.85
		5	-0.24	0.37

Table 9: Collection of seismic improvement for an earthquake with a single layer of metapanel for masonry structure.

These results were achievable due to the presence of the metapanel, which acted as a passive control system through the mass applied above them. The earthquake input generated deformation in the panel, and through the oscillation of the mass and the bistable behavior, it was possible to achieve seismic improvement for almost all of the buildings.

Time-history dynamic analysis under wind excitation

This section presents *Fig.64,65* that illustrate how the simulated application of wind acts on the masonry structure in the absence of metapanel compared to their presence. The figures show two types of functions: one in red, referring to the "controlled" case, which consists of the structure system with metapanel applied only on the top floor. The black function refers to the "uncontrolled" case, consisting of the structure system alone. Both functions describe the displacement of the same centroid point located on the topmost floor slab. As previously stated, this simulation was carried out considering that the wind was applied to the entire surface corresponding to the X direction.

The purpose of this analysis was to evaluate whether the presence of metapanel applied to buildings with five above-ground floors could ensure, in addition to seismic improvement, an enhancement of comfort throughout the building's service life. The values will be reported in Table 10.

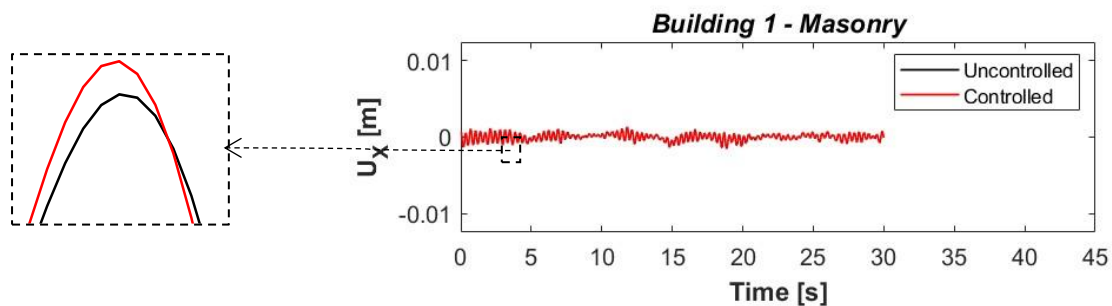


Figure 64: Wind displacement with one layer of metapanel (1M)

In the case of *Fig. 64*, which refers to the masonry structure with a square floor plan and a node height of $Z = 15$ m, a zoom-in was made at the peak point that occurred at the peak displacement

The dissipative capacity and the relative reduction in the peak corresponding to the displacement along X is **2.73 %**. For these simulations, no study was presented regarding the displacement along the Y direction for the applied load assumptions. The value will be appropriately collected in Table 10.

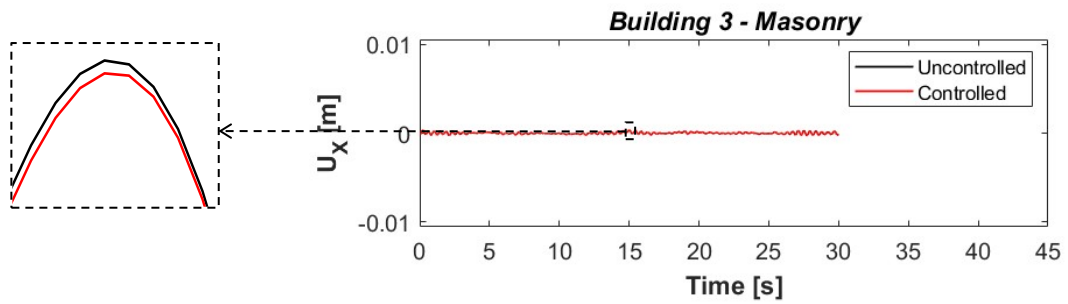


Figure 65: Wind displacement with one layer of metapanel (3M)

In the case of Fig. 65, which refers to the masonry structure with a rectangular floor plan and a node height of $Z = 15$ m, a zoom-in was made at the peak point that occurred at the peak displacement

The dissipative capacity and the relative reduction in the peak corresponding to the displacement along X is **1.59 %**. For these simulations, no study was presented regarding the displacement along the Y direction for the applied load assumptions. The value will be appropriately collected in Table 10.

One Layer of metapanel				
	<i>PLANE</i>	<i>FLOORS</i>	ΔU_x [%]	ΔU_y [%]
Masonry	<i>square</i>	-	-	-
		5	2.73	-
	<i>rectangular</i>	-	-	-
		5	1.59	-

Table 10: Collection of wind-induced dissipative capacity for a single layer of metapanel for masonry structure

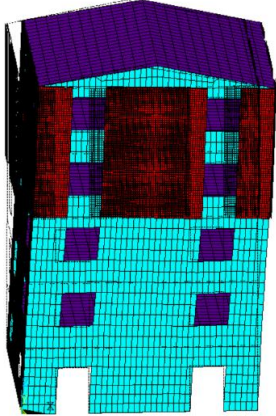
The results presented in Table 10 show that the application of simulated wind to masonry structures taller than 15 meters has led to an improvement in comfort.

5.2.2 Second proposed solution

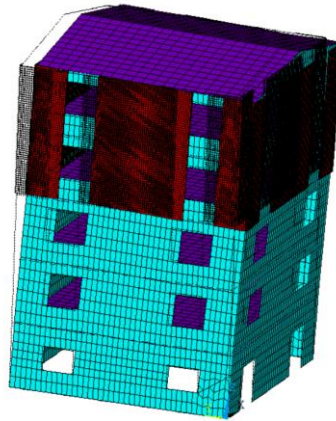
Modal analysis

First square plan – Masonry

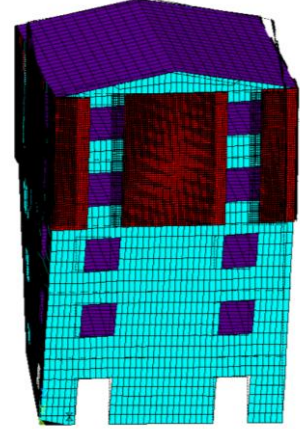
$$f_1 = 2.91 \text{ Hz}$$



$$f_2 = 2.93 \text{ Hz}$$

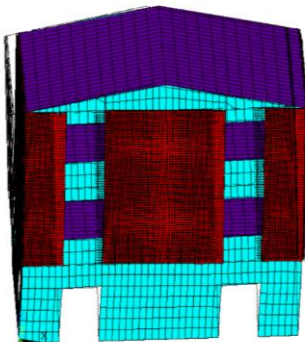


$$f_3 = 5.46 \text{ Hz}$$

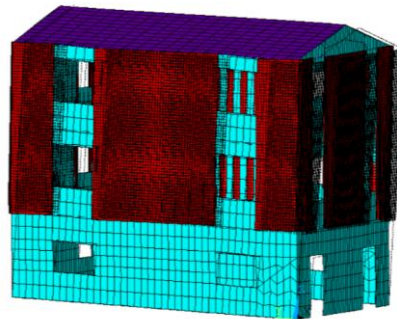


Second square plan – Masonry

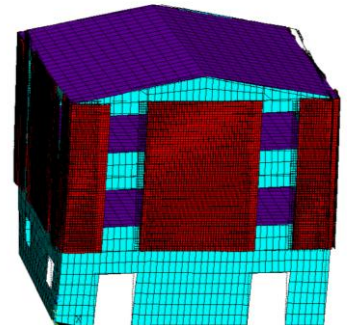
$$f_1 = 5.22 \text{ Hz}$$



$$f_2 = 5.31 \text{ Hz}$$

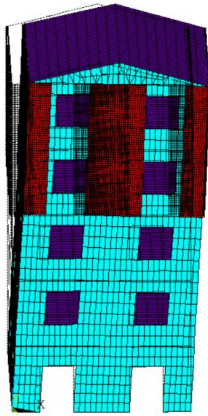


$$f_3 = 9.06 \text{ Hz}$$

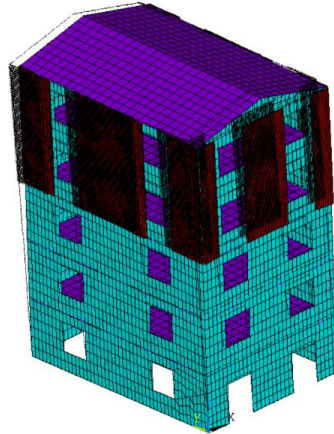


Third rectangular plan – Masonry

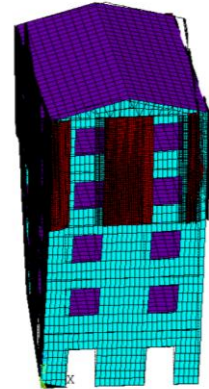
$f_1 = 2.41 \text{ Hz}$



$f_2 = 3.28 \text{ Hz}$

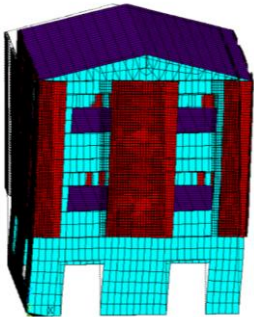


$f_3 = 5.06 \text{ Hz}$

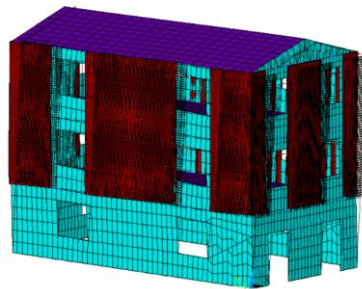


Fourth rectangular plan – Masonry

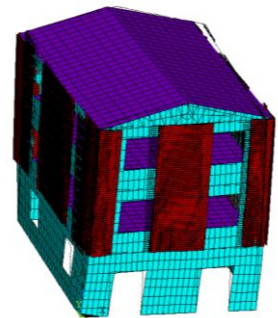
$f_1 = 4.23 \text{ Hz}$



$f_2 = 5.91 \text{ Hz}$



$f_3 = 8.24 \text{ Hz}$



Time-history dynamic analysis under earthquake excitation

This section will present the displacement solutions for masonry buildings, this time with metapanel applied to the façade of both the top and second-to-last floors as illustrated in section 5.1.2.

As can be observed in *Fig. 66,67,68* and *69*, two types of functions have been plotted, corresponding to the displacement at the centroid of the topmost accessible floor of the considered structure. The red curve represents the deformation response in the "controlled" case, while the black curve represents the deformation response in the "uncontrolled" case. For each case, we compared and estimated the peak displacement reduction, also creating an auxiliary image to ensure better visualization. Furthermore, the displacement recorded along the X direction is larger than the displacement in the Y direction, this is due to the assumptions made according to EC8.

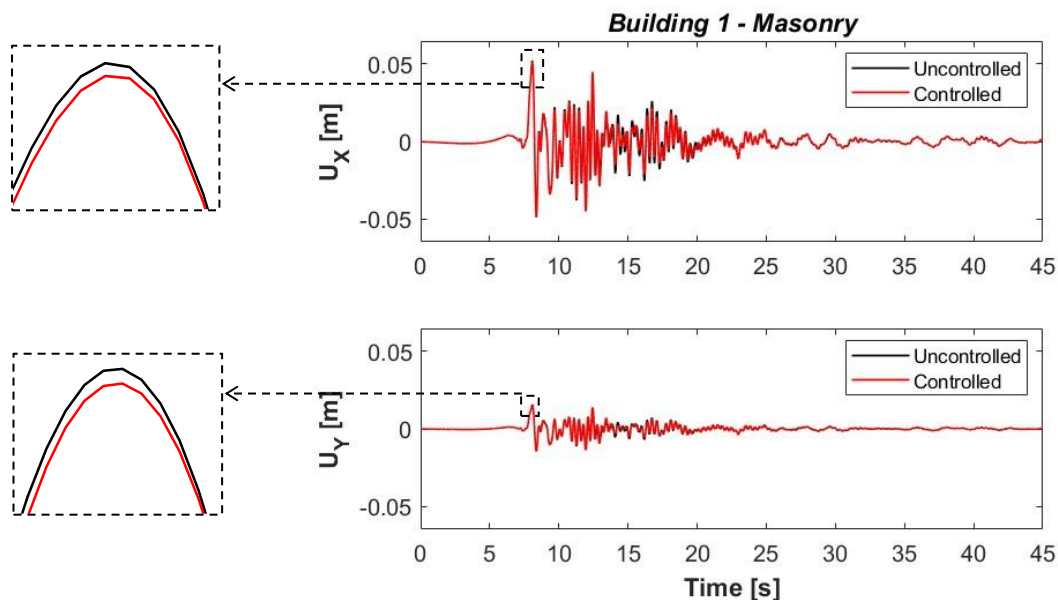


Figure 66: Earthquake displacement with two layers of metapanel (1M)

In *Fig. 66*, which refers to the masonry structure with a square floor plan and a node height of $Z=15$ m, a zoom-in was made at the peak point that occurred at the peak displacement.

The relative seismic improvement and the reduction in the peak corresponding only to the displacement along X is **0.51 %**. In this case, for the displacements referred to the Y direction, no seismic improvement was found, corresponding to **0.48 %**, these values will be appropriately collected in Table 11.

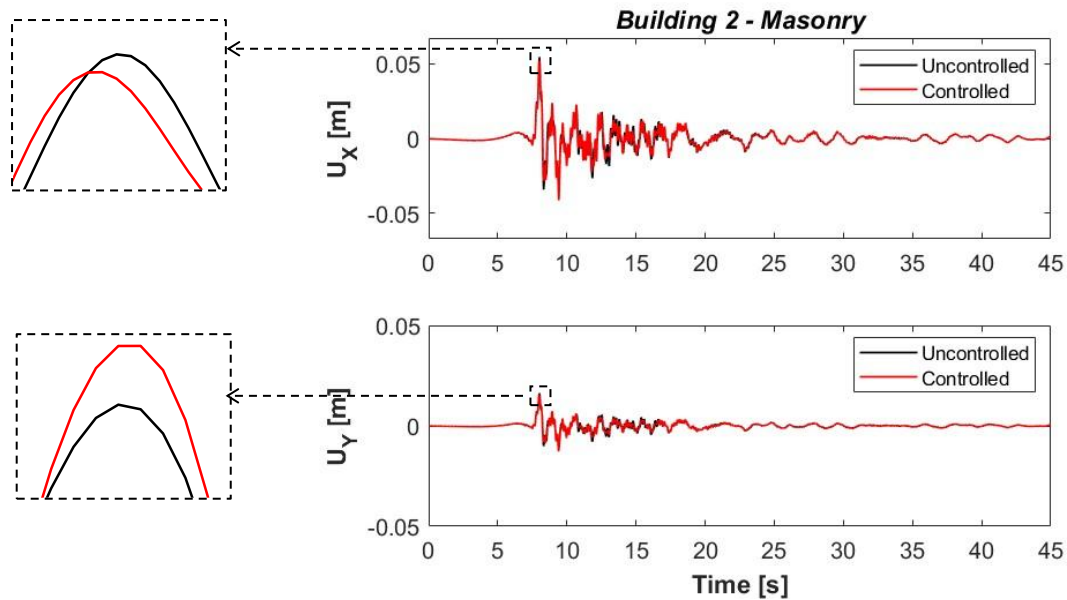


Figure 67: Earthquake displacement with two layers of metapanel (2M)

The presence of a double row of metapanel installed on the building has led to significant increases in seismic dissipation. As can be observed, in Fig. 67, which refers to the masonry structure with a square floor plan and a node height of $Z=9$ m, a zoom-in was made at the peak point that occurred at the peak displacement.

The seismic improvement and the relative reduction in the peak corresponding only to the displacement along X is **4.07 %**. In this case, for the displacements referred to the Y direction, no seismic improvement was found, corresponding to **5.02 %**, these values will be appropriately collected in Table 11.

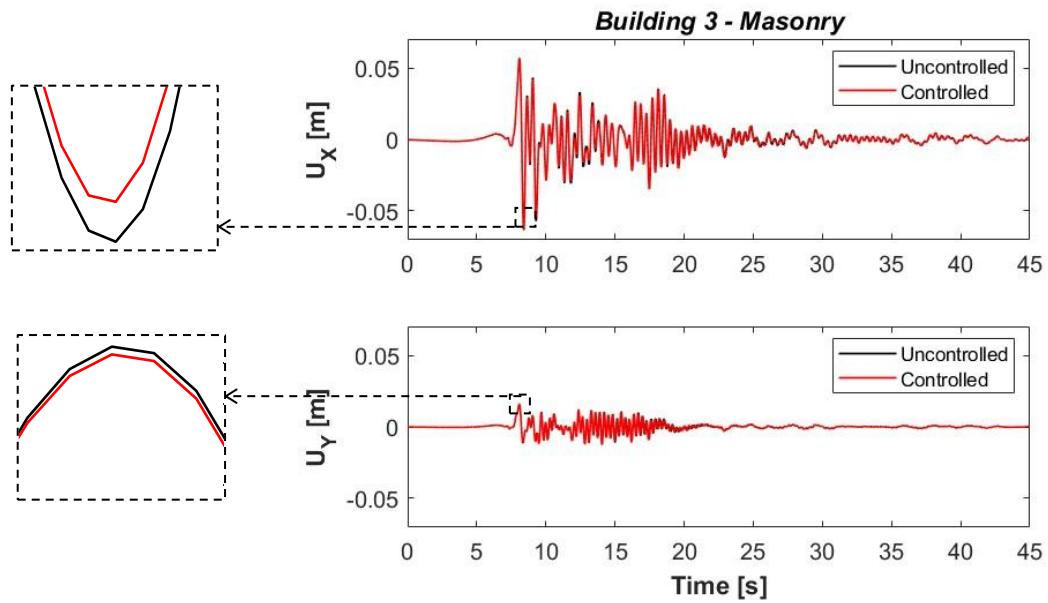


Figure 68: Earthquake displacement with two layers of metapanel (3M)

In the case of *Fig. 68*, which refers to the masonry structure with a rectangular floor plan and a node height of $Z = 15$ m, a zoom-in was made at the peak point that occurred at the peak displacement.

The seismic improvement and the relative reduction in the peak corresponding only to the displacement along X is **1.11 %**. In this case, for the displacements referred to the Y direction, no seismic improvement was found, corresponding to **-0.41 %**, these values will be appropriately collected in Table 11.

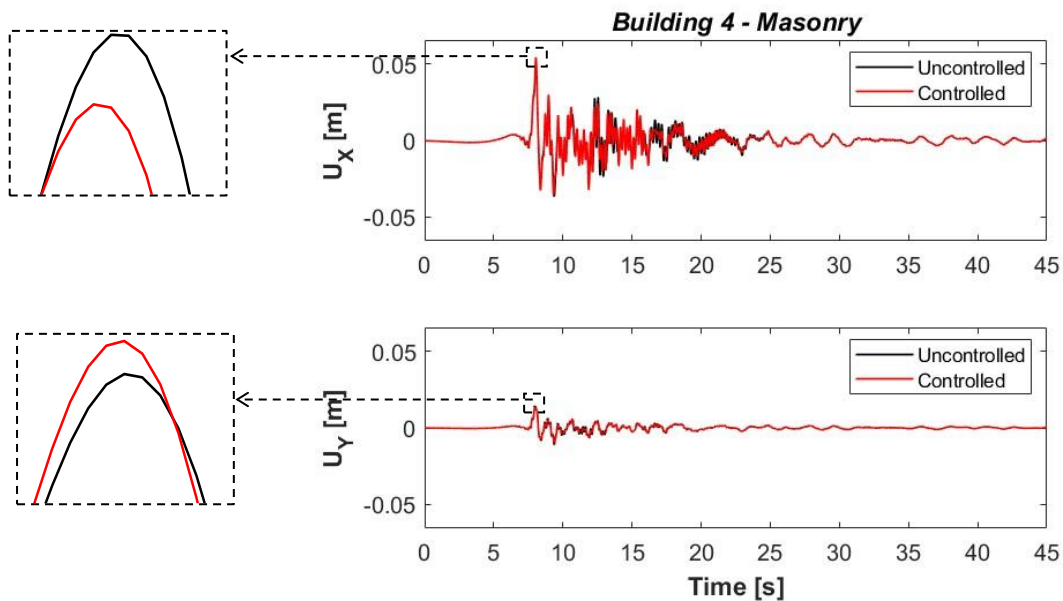


Figure 69: Earthquake displacement with two layers of metapanel (4M)

In the case of *Fig. 69*, which refers to the masonry structure with a rectangular floor plan and a node height of $Z = 9$ m, a zoom-in was made at the peak point that occurred at the peak displacement.

The seismic improvement and the relative reduction in the peak corresponding only to the displacement along Y is **8.24 %**. In this case, for the displacements referred to the Y direction, no seismic improvement was found, corresponding to **-2.85 %**, these values will be appropriately collected in Table 11.

Two Layer of metapanel				
	<i>PLANE</i>	<i>FLOORS</i>	Δu_x [%]	Δu_y [%]
Masonry	<i>square</i>	3	4.07	5.02
		5	0.51	0.48
	<i>rectangular</i>	3	-2.85	8.24
		5	1.11	-0.14

Table 11: Collection of seismic improvement for an earthquake with a double layer of metapanel for masonry structure

The results shown in Table 11 demonstrate how the use of a greater mass applied to the surface of masonry structure, significantly contributes to seismic improvement. The increase in mass generated a rise in damping, amplifying the passive absorption of the metapanel. Through its bistable properties, the increase in absorbed energy was enhanced, leading to much higher values in most cases, even exceeding **8%**.

Summary table of earthquake results

One Layer of metapanel				
	<i>PLANE</i>	<i>FLOORS</i>	Δu_x [%]	Δu_y [%]
Reinforced Concrete	<i>square</i>	3	1.51	2.63
		5	1.43	2.73
	<i>rectangular</i>	3	0.99	-1.83
		5	1.37	1.62
Two Layer of metapanel				
	<i>PLANE</i>	<i>FLOORS</i>	Δu_x [%]	Δu_y [%]
Reinforced Concrete	<i>square</i>	3	3.88	2.67
		5	12.10	14.28
	<i>rectangular</i>	3	-2.34	-5.40
		5	2.80	4.84

Table 12: Summary table for reinforced concrete structures subjected to earthquake

Summary table of earthquake results

One Layer of metapanel				
	<i>PLANE</i>	<i>FLOORS</i>	Δu_x [%]	Δu_y [%]
Masonry	<i>square</i>	-	-	-
		5	2.73	-
	<i>rectangular</i>	-	-	-
		5	1.59	-
Two Layer of metapanel				
	<i>PLANE</i>	<i>FLOORS</i>	Δu_x [%]	Δu_y [%]
Masonry	<i>square</i>	3	4.07	5.02
		5	0.51	0.48
	<i>rectangular</i>	3	-2.85	8.24
		5	1.11	-0.14

Table 13: Summary table for masonry structures subjected to earthquakes

Summary table of wind results

One Layer of metapanel				
	<i>PLANE</i>	<i>FLOORS</i>	Δu_x [%]	Δu_y [%]
Reinforced Concrete	<i>square</i>	-	-	-
		5	38.05	-
	<i>rectangular</i>	-	-	-
		5	1.26	-
One Layer of metapanel				
	<i>PLANE</i>	<i>FLOORS</i>	Δu_x [%]	Δu_y [%]
Masonry	<i>square</i>	-	-	-
		5	2.73	-
	<i>rectangular</i>	-	-	-
		5	1.59	-

Table 14: Summary table for masonry and reinforced structures subjected to wind

As illustrated in the previous chapters, the eight buildings made of masonry and reinforced concrete were analysed through a time history analysis to evaluate the dissipative effect of the metapanel during earthquake application and comfort during wind application. The results summarized in the tables above indicate that, in most cases, the application of metapanel led to seismic improvement and enhanced comfort. The results vary depending on the type of analysis, leading to the conclusion that metapanel achieve good performance when properly optimized.

6.0 Conclusion

This thesis explored an innovative approach for improving the seismic response of buildings, by using the advanced properties of mechanical metamaterials through the use of bistable metapanel. This study, applied to a benchmark of four structures, made of reinforced concrete and masonry, with different heights and plans, provided an in-depth exploration of the impact of metapanel in terms of both reducing seismic forces and improving comfort in the case of wind load application. Starting with an analysis of the current state of the different structures, the integration of metapanel was designed to address specific seismic needs while preserving the aesthetic integrity of the building. The simulation results highlighted how the use of metapanel can lead to a more or less significant reduction in displacements and oscillations during seismic events, thereby tangibly improving the dynamic response of the structure. This behavior is attributed to the bistability of the metapanel and the passive absorption derived from the motion of the mass applied to the surface, which can increase energy dissipation only when the metapanel is optimized, and consequently, leads to a reduction in displacements. A key aspect is the possibility of using metapanel as reversible and non-invasive solutions, particularly suitable for existing buildings. The reversibility of metapanel adds value in contexts where preserving the integrity of the structure is a priority, as they can be removed without leaving permanent traces and potentially allow for the restoration of the building to its original state. This approach also offers a high degree of adaptability, enabling the installation or removal of metapanel depending on risk conditions and seismic regulations, which may change over time. These features make metapanel a flexible and sustainable solution, particularly suitable for the long-term preservation of historic buildings in seismic areas. In conclusion, the adoption of bistable metapanel proves to be a promising and sustainable strategy for seismic protection and wind load management on existing buildings, combining structural effectiveness, respect for architectural integrity, and comfort.

References

- [1] X.-Y. Cao, D. Shen, D.-C. Feng, C.-L. Wang, Z. Qu, and G. Wu, “Seismic retrofitting of existing frame buildings through externally attached sub-structures: State of the art review and future perspectives.”
- [2] S. G. Luca, C. Pastia, I. Toma, and M. Budescu, “Control strategies for seismic energy dissipation,” in *International Multidisciplinary Scientific GeoConference Surveying Geology and Mining Ecology Management, SGEM*, International Multidisciplinary Scientific Geoconference, 2014, pp. 435–442. doi: 10.5593/sgem2014/b11/s5.058.
- [3] A. S. Saeed, R. Abdul Nasar, and M. A. AL-Shudeifat, “A review on nonlinear energy sinks: designs, analysis and applications of impact and rotary types,” Jan. 01, 2023, *Springer Science and Business Media B.V.* doi: 10.1007/s11071-022-08094-y.
- [4] A.F. Vakakis and O.V. Gendelman, “Nonlinear Targeted Energy Transfer in Mechanical and Structural Systems I.” [Online]. Available: www.springer.com/series/6557
- [5] G. Singh and A. Marwaha, “A Review of Metamaterials and its Applications,” *International Journal of Engineering Trends and Technology*, vol. 19, no. 6, 2015, [Online]. Available: <http://www.ijettjournal.org>
- [6] X. Tan *et al.*, “Effect of beam configuration on its multistable and negative stiffness properties,” *Compos Struct*, vol. 286, Apr. 2022, doi: 10.1016/j.compstruct.2022.115308.
- [7] X. Yu, J. Zhou, H. Liang, Z. Jiang, and L. Wu, “Mechanical metamaterials associated with stiffness, rigidity and compressibility: A brief review,” May 01, 2018, *Elsevier Ltd.* doi: 10.1016/j.pmatsci.2017.12.003.
- [8] Ryan L. Harne and K.W.Wang, “Harnessing Bistable Structural Dynamics.”
- [9] G.K. Ananthasuresh, “The Principle of Minimum Potential Energy.”
- [10] S. Chen *et al.*, “A novel gradient negative stiffness honeycomb for recoverable energy absorption,” *Compos B Eng*, vol. 215, Jun. 2021, doi: 10.1016/j.compositesb.2021.108745.
- [11] J. O. Martín del Campo, A. Pozos-Estrada, and O. Pozos-Estrada, “Development of fragility curves of land-based wind turbines with tuned mass dampers under cyclone and seismic loading,” *Wind Energy*, vol. 24, no. 7, pp. 737–753, Jul. 2021, doi: 10.1002/we.2600.
- [12] <https://terremoti.ingv.it/>

RINGRAZIAMENTI

Vorrei dedicare questo spazio e queste parole alle persone che mi hanno accompagnato per questi anni, agli amici e ai colleghi, è stata un'esperienza ricca di emozioni e sacrifici ma accanto a loro è stato più facile e divertente.

Un particolare ringraziamento va alla mia famiglia, il loro contributo e la loro presenza mi ha permesso di raggiungere questo piccolo grande obiettivo, non potrò mai dimenticarlo. E poi, un ringraziamento alla mia dolce metà Giulia, il suo supporto, il suo tifo e le sue parole mi hanno aiutato ad accendere una luce quando tutto sembrava buio.